Unitary Fermi gas in the ϵ expansion

Yusuke Nishida

Department of Physics, University of Tokyo

December 2006

PhD Thesis

Abstract

We construct systematic expansions around four and two spatial dimensions for a Fermi gas near the unitarity limit. Near four spatial dimensions such a Fermi gas can be understood as a weakly-interacting system of fermionic and bosonic degrees of freedom. To the leading and next-to-leading orders in the expansion over $\epsilon = 4 - d$, with d being the dimensionality of space, we calculate the thermodynamic functions and the fermion quasiparticle spectrum as functions of the binding energy of the two-body state. We also show that the unitary Fermi gas near two spatial dimensions reduces to a weakly-interacting Fermi gas and calculate the thermodynamic functions and the fermion quasiparticle spectrum in the expansion over $\bar{\epsilon} = d - 2$.

Then the phase structure of the polarized Fermi gas with equal and unequal masses in the unitary regime is studied using the ϵ expansion. We find that at unitarity in the equal mass limit, there is a first-order phase transition from the unpolarized superfluid state to a fully polarized normal state. On the BEC side of the unitarity point, in a certain range of the two-body binding energy and the mass difference, we find a gapless superfluid phase and a superfluid phase with spatially varying condensate. These phases occupy a region in the phase diagram between the gapped superfluid phase and the polarized normal phase.

Thermodynamics of the unitary Fermi gas at finite temperature is also investigated from the perspective of the expansion over ϵ. We show that the thermodynamics is dominated by bosonic excitations in the low temperature region $T \ll T_c$. Analytic formulas for the thermodynamic functions as functions of the temperature are derived to the lowest order in ϵ in this region. In the high temperature region where $T \sim T_c$, bosonic and fermionic quasiparticles are excited and we determine the critical temperature T_c and the thermodynamic functions around T_c to the leading and next-to-leading orders in ϵ and $\bar{\epsilon}$.

Finally we discuss the matching of the two systematic expansions around four and two spatial dimensions in order to extract physical observables at $d = 3$. We find good agreement of the results with those from recent Monte Carlo simulations.

Table of Contents

Chapter 1

Introduction

BCS-BEC crossover and the unitarity limit

Interacting fermionic systems appear in various subfields of physics. The Bardeen–Cooper–Schrieffer (BCS) mechanism shows that if the interaction is attractive, the Fermi surface is unstable toward the formation of Cooper pairs and the ground state of the system universally exhibits the superfluidity or superconductivity [1, 2]. Such phenomena have been observed in the metallic superconductor [3], the superfluid ^{3}He [4], the high-T_c superconductor [5], and recently, in the ultracold atomic gases such as ^{40}K [6] or ^{6}Li [7] under optical traps. Possibilities of the superfluid nuclear matter [8, 9], the color superconductivity [10, 11], and the neutrino superfluidity [12] are also discussed in literatures, which will be important to astrophysics such as the physics of neutron stars. Among others, experiments on the ultracold atomic gases have the remarkable feature where the strength of attraction between atoms is arbitrarily tunable through the magnetic-field induced Feshbach resonances [13, 14]. Their interaction predominantly arises from binary s-wave collisions whose strength can be characterized by the s-wave scattering length a. Across the Feshbach resonance, a can in principal be tuned to take any value from -0 to $-\infty$ and from $+\infty$ to $+0$ [15, 16]. Therefore, the experiments of the ultracold atomic gases provide an ideal field for studying interacting fermionic systems and testing various many-body techniques developed for related problems.

With the use of the experimental technique of the magnetic-field tunable Feshbach resonance, the longstanding idea of the crossover from the BCS state to the Bose–Einstein condensation (BEC) [17, 18, 19, 20] has been recently realized in laboratories. The schematic phase diagram of the BCS-BEC crossover problem is shown in Fig. 1.1 as a function of the dimensionless variable $1/(ak_F)$ with k_F being the Fermi momentum (horizontal axis). Here the effective range of the interaction r_0 is assumed to be small $r_0 k_F \to 0$. As long as the attractive interaction between fermions is weak (BCS regime where $ak_F < 0$), the system exhibits the BCS ground state characterized by the condensation of the loosely bound Cooper pairs. On the other hand, if the attractive interaction is strong enough (BEC regime where $0 < ak_F$), two fermions form a bound molecule and the ground state of the system is described by the BEC of the tightly bound molecules. These two apparently different situations are considered to be smoothly connected without the phase transition, which means the ground state in

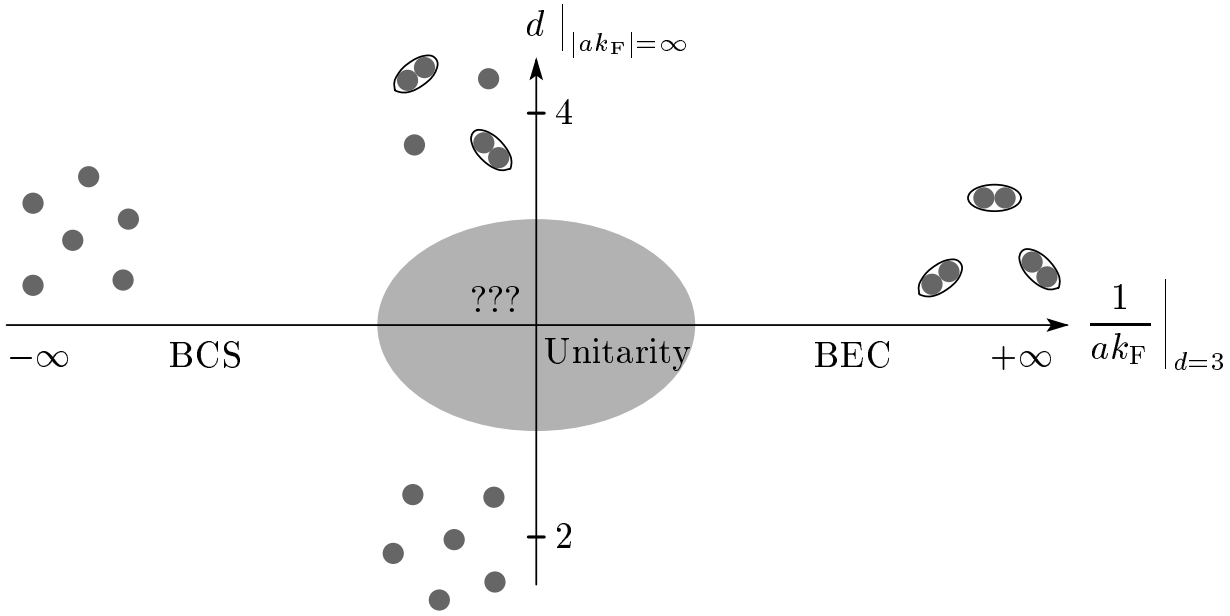

Figure 1.1: The BCS-BEC crossover problem in the plane of the inverse scattering length $1/ak_F$ and the spatial dimension d. There are four limits where the system becomes non-interacting; $ak_F \to \pm 0$, $d \to 4$, and $d \to 2$.

the whole regime of the $1/(ak_F)$ axis is the superfluidity/superconductivity.

The both ends of the phase diagram correspond to weakly-interacting systems; a weakly-interacting Fermi gas in the BCS limit $ak_F \to -0$ and a weakly-interacting Bose gas in the BEC limit $ak_F \to +0$. In these two limits, the usual Green's function techniques for the many-body problem are applicable and we can understand the properties of the system in terms of the perturbative expansion over $|ak_F| \ll 1$ [21]. An exception is the superfluidity in the BCS limit where the paring gap $\Delta \sim e^{\pi/(2ak_F)}$ is a non-perturbative effect and never appears to any finite orders in the perturbative ak_F expansion. On the other hand, there exists a strongly-interacting regime in the middle of the phase diagram where $|ak_F| \gg 1$. The point of the infinite scattering length $|ak_F| \to \infty$ corresponds to the threshold where the zero energy bound molecule is formed and provides the conceptual boundary between the BCS regime and the BEC regime. The perturbative expansion over $|ak_F|$ obviously breaks down in this regime because the expansion parameter is no longer small. Such a regime is frequently referred to as the unitary regime because the infinite scattering length $|ak_F| \to \infty$ is the "unitarity limit" where the s-wave cross section reaches the maximal value allowed by the unitarity constraint of the scattering matrix.

The Fermi gas in the unitarity limit, which we refer to as the unitary Fermi gas, has attracted intense attention across many subfields of physics. As we mentioned, the system can be experimentally realized in atomic traps using the Feshbach resonance and has been extensively studied [22, 23, 24, 25, 26, 27, 28, 29, 30, 31, 6, 32, 33, 7, 34, 35, 36, 37, 38, 39, 40, 41, 42, 43, 44, 45, 46]. Furthermore, since the fermion density is the only dimensionful scale of the unitary Fermi gas, its

properties are expected to be *universal*, i.e., independent of details of the interparticle interaction. The unitary Fermi gas is thus an idealization of dilute nuclear matter [47], where the neutron-neutron s-wave scattering length $a_{nn} \simeq -18.5\,\mathrm{fm}$ is much larger than the effective range $r_0 \simeq 2.7\,\mathrm{fm}$ [48], and may be relevant to the physics of neutron stars. It has been also suggested that its understanding may be important for the high-T_c superconductivity [49]. The Fermi gas in the unitary regime provides a new interesting regime other than the conventional weak-coupling BCS and BEC regimes and is worthwhile to study experimentally and theoretically.

Experimental achievements

Before going to details of the theoretical treatment of this thesis, we briefly summarize related experimental achievements in the trapped fermionic atoms over the past decade. Typically $10^5 \sim 10^6$ atoms are confined in the optical potential and can be cooled down to the temperature $\sim 0.1\,E_\mathrm{F}$ using the laser cooling and evaporative cooling [50], where E_F is the Fermi energy of order micro-Kelvin. The degenerate Fermi gas of atoms was first reported in [51], where the non-classical momentum distribution and total energy of the gas were observed. The magnetic-field induced Feshbach resonance make it possible to realize the degenerate Fermi gas in the strongly-interacting regime where $|a|k_\mathrm{F} \gg 1$. Expansion dynamics of such a strongly-interacting degenerate Fermi gas was studied and an anisotropic expansion was observed when the gas is released from the optical trap [22]. The hydrodynamics of expanding strongly-interacting fermionic systems has also attracted special interest of nuclear physics community in connection with the strongly-interacting matter created in the experiment of Relativistic Heavy Ion Collisions [52, 53, 54, 55, 56, 57].

The next goal after creating the degenerate Fermi gas of atoms in the strongly-interacting regime was to establish the superfluidity. First a long-lived molecular gas was created from the atomic Fermi gas using the Feshbach resonance [25, 26, 27, 28, 32] and the condensation of the weakly bound molecules was observed on the BEC side $ak_\mathrm{F} > 0$ [29, 30, 31, 33, 36, 40]. The BEC of the bound molecules formed by fermionic atoms is in complete analogy with that of bosonic atoms achieved earlier using ^{87}Rb or ^{23}Na [58, 59]. The sudden onset of a peak in the momentum distribution of the molecules was reported indicating the phase transition to the BEC state. Soon after the realization of the molecular condensates on the BEC side, the condensation of fermionic atom pairs was observed on the BCS side $ak_\mathrm{F} < 0$ [6, 7]. Here a pairwise projection of the fermionic atoms onto molecules by a rapid sweep from negative a to positive a was used to measure the momentum distribution of the fermionic atom pairs. As an evidence of the superfluidity, collective excitations of the trapped Fermi gas were studied, where the measured frequencies and damping rates are plausibly explained assuming the superfluidity [34, 35, 38]. Another evidence of the superfluidity was an appearance of the pairing gap measured using the radio frequency spectroscopy [37]. The critical temperature as an onset of the superfluidity was presented from the measurement of the heat capacity [39]. Finally the definitive evidence of the superfluidity was provided by the observation of vortex lattices in a rotating Fermi gas [41].

The striking properties of these trapped atomic systems lay not only on the tunability of the interaction strength between atoms but also on their high designability of various interesting systems. For example, Fermi gases with a population imbalance between the two fermion components (finite polarization) have been already realized and studied [42, 43, 44, 45, 46]. The phase separation in the trapping potential was observed where the superfluid core with equal densities is surrounded by the normal gas with unequal densities. Also the realization of Feshbach resonances is available between two different atomic species [60, 61]. While such Feshbach resonances are currently achieved only between fermionic and bosonic atoms, it may be possible in future to realize the Feshbach resonances between two different species of fermionic atoms. It will bring us a new ground to investigate a Fermi gas with finite mass difference between different fermion species. Such asymmetric systems of fermions with density and mass imbalances will be also interesting as a prototype of high density quark matter in the core of neutron stars, where the density and mass asymmetries exist among different quark flavors [62, 63, 64, 65, 66].

Theoretical treatment and ϵ expansion

The breathtaking experimental progresses with high tunability and designability have stimulated various theoretical studies in the new regime of the unitarity limit. The austere simplicity of the unitary Fermi gas, however, implies great difficulties for theoretical treatment, because there seems to be no parameter for a perturbation theory. The usual Green's function techniques for the many-body problem is completely unreliable here since the expansion parameter ak_{F} becomes infinite in the unitarity limit. Although the mean-field type approximations (with or without fluctuations) are often adopted to give a qualitative picture of the BCS-BEC crossover problem, they are not controlled approximations in the strong-coupling unitary regime [17, 18, 19, 20, 67, 68, 69, 70, 71, 72, 73, 74, 75, 76, 77, 78]. A challenging problem for many-body theorists is to establish a systematic approach to investigate the Fermi gas in the unitary regime.

At very high temperatures, a systematic expansion in terms of the fugacity $z = e^{\mu/T}$ (virial expansion) is applicable where μ denotes the chemical potential and T denotes the temperature [79, 80, 81]. However, the virial expansion is restricted to the normal state and can not describe the phase transition to the superfluid state. Considerable progress on the study of the unitary Fermi gas has been recently made by Monte Carlo simulations both at zero temperature [82, 83, 84, 85, 86, 87] and finite temperature [88, 89, 90, 91, 92], but these simulations also have various limitations. For example, Monte Carlo simulations can not treat systems with a population or mass imbalance between two fermion species due to fermion sign problem. Also they can not answer questions related to dynamics like the dynamical response functions and the kinetic coefficients. Analytic treatments of the problem at any temperature, if exist, will be extremely useful and give insights that are not obvious from numerics.

Recently we have proposed a new analytic approach for the unitary Fermi gas based on the systematic expansion in terms of the dimensionality of space [93, 94, 95], utilizing the specialty of *four* or *two* spatial dimensions in the unitarity limit [96]. In this approach, one would extend the problem

to arbitrary spatial dimensions d with keeping the scattering length to be infinite $|ak_{\mathrm{F}}| \to \infty$ (vertical axis in Fig. 1.1). Then we find two non-interacting limits on the d axis, which are $d = 4$ and $d = 2$. Accordingly, slightly below four or slightly above two spatial dimensions, the unitary Fermi gas becomes weakly-interacting, where a "perturbative expansion" is available. Actually the unitary Fermi gas near four spatial dimensions can be understood as a weakly-interacting system of fermionic and bosonic quasiparticles, while near two spatial dimensions it reduces to a weakly-interacting Fermi gas. A small parameter of the perturbative expansion there is $\epsilon = 4 - d$ near four dimensions or $\bar{\epsilon} = d - 2$ near two dimensions. The weakness of the interaction near four and two spatial dimensions can be also seen from the viewpoint of the renormalization group fixed point; the fixed point describing the unitarity limit approaches to the non-interacting Gaussian fixed point near $d = 4$ and $d = 2$ [97, 98]. After performing all calculations treating ϵ or $\bar{\epsilon}$ as a small expansion parameter, results for the physical case of three spatial dimensions are obtained by extrapolating the series expansions to $\epsilon\,(\bar{\epsilon}) = 1$, or more appropriately, by matching the two series expansions.

The ϵ expansion around four spatial dimensions has been developed to calculate thermodynamic functions and the fermion quasiparticle spectrum at zero temperature near the unitarity limit to the leading and next-to-leading orders in ϵ. The results were found to be quite consistent with those obtained by the Monte Carlo simulations and the experiments [93, 94]. Then the ϵ expansion was extended to investigate the thermodynamics of the unitary Fermi gas at finite temperature T, below and above the critical temperature $T = T_{\mathrm{c}}$ [95]. It should be noted that the critical dimension of a superfluid-normal phase transition is also four, which makes weak-coupling calculations reliable at any temperature for the small ϵ. The ϵ expansion was also successfully applied to study atom-dimer and dimer-dimer scatterings in vacuum and found to give results quite close to non-perturbative numerical solutions at $d = 3$ [99]. Thus there are compelling reasons to hope that the limit $d \to 4$ is not only theoretically interesting but also practically useful, despite the fact that the expansion parameter ϵ is one at $d = 3$. We recall that the ϵ expansion has been extremely fruitful in the theory of the second order phase transition [100]. In addition to the above-mentioned works, the phase structure of the polarized Fermi gas near the unitarity limit has been investigated based on the ϵ expansion [94, 101]. The next-to-next-to-leading order correction to the thermodynamic functions at zero temperature was computed in [102] and the BCS-BEC crossover was studied by the ϵ expansion [103]. Very recently, another systematic approach to the Fermi gas in the unitary regime has been proposed; the two-component Fermi gas is generalized to a $2N$-component Fermi gas with $\mathrm{Sp}(2N)$ invariant interaction. Then the inverse of the component number $1/N$ is used for the small expansion parameter [98, 104].

In this thesis, we give a comprehensive study of the unitary Fermi gas from the perspective of the ϵ expansion. We start with the study of two-body scattering in vacuum in the unitarity limit for arbitrary spatial dimensions $2 < d < 4$, which will clarify why and how systematic expansions around four and two spatial dimensions are possible for the unitary Fermi gas (Chap. 2). In Chap. 3, we give a detailed account of the ϵ expansion for the unitary Fermi gas and show the results on the thermodynamic functions and the fermion quasiparticle spectrum in the unitary regime to the leading and next-to-leading orders in ϵ. Then the ϵ expansion is applied to the unitary Fermi gas with unequal densities

of two components, which we call "polarized" Fermi gas. The phase structure of the polarized Fermi gas as a function of the two-body binding energy is investigated with equal fermion masses in Chap. 4 and with unequal fermion masses in Chap 5. We also show in Chap. 6 that there exists a systematic expansion for the Fermi gas in the unitarity limit around two spatial dimensions. In Chap. 7, we make an exploratory discussion to connect the two systematic expansions around four and two spatial dimensions in order to extract results at $d = 3$. Chaps. 8 and 9 are devoted to the thermodynamics of the unitary Fermi gas at finite temperature. In Chap. 8, analytic formulas for the thermodynamic functions in the low temperature region $T \ll T_c$ are shown as functions of the temperature to the lowest order in ϵ. The behavior of the thermodynamic functions above T_c to the leading and next-to-leading orders in ϵ is discussed in Chap. 9. In particular, we put emphasis on the determination of the critical temperature T_c and the thermodynamic functions at T_c by matching the ϵ expansion with the expansion around two spatial dimensions. All the results thus obtained are compared to those from the recent Monte Carlo simulations. Finally, summary and concluding remarks are given in Chap. 10.

The chapters 2–7 in this thesis are based on the author's works in collaboration with D. T. Son [93, 94, 105], while the chapters 8 and 9 are based on the author's paper [95].

Chapter 2

Two-body scattering in vacuum

The special role of four and two spatial dimensions in the unitarity limit has been recognized by Nussinov and Nussinov [96]. They noticed that at infinite scattering length, the wavefunction of two fermions with opposite spin behaves like $R(r) = 1/r^{d-2}$ at small r, where r is the separation between two fermions. Therefore, the normalization integral of the wavefunction takes the form of

$$\int d\boldsymbol{r} R(r)^2 = \int_{r_0} dr \frac{1}{r^{d-3}}, \tag{2.1}$$

which has a singularity at $r_0 \to 0$ in high dimensions $d \geq 4$. From this observation, it is concluded that the unitary Fermi gas at $d \to 4$ become a non-interacting Bose gas. In particular, at fixed Fermi momentum the energy per particle goes to zero as $d \to 4$ from below. On the other hand, in low dimensions $d \leq 2$, the attractive potential with any strength causes zero energy bound states, and hence, the threshold of the appearance of the first two-body bound state corresponds to the zero coupling. It follows that the Fermi gas in the unitary limit corresponds to a non-interacting Fermi gas at $d \to 2$ and the energy per particle approaches to that of the free Fermi gas in this limit. This singular character of $d = 2$ was also recognized in the earlier work [106].

In this Chapter, we shall give precise meaning for their intuitive arguments at $d = 4$ and 2 from the perspective of diagrammatic approach. These two dimensions will provide foundations to construct systematic expansions for the unitary Fermi gas. Here we concentrate on the two-body problem.

2.1 Near four spatial dimensions

The system under consideration is described by a Lagrangian density with a local four-Fermi interaction (here and below $\hbar = 1$):

$$\mathcal{L} = \sum_{\sigma=\uparrow,\downarrow} \psi_\sigma^\dagger \left(i\partial_t + \frac{\boldsymbol{\nabla}^2}{2m_\sigma} \right) \psi_\sigma + c_0 \, \psi_\uparrow^\dagger \psi_\downarrow^\dagger \psi_\downarrow \psi_\uparrow, \tag{2.2}$$

where m_σ $(= m_\uparrow, m_\downarrow)$ is the fermion mass and c_0 is the bare attractive coupling between two fermions. Here we consider the fermions with equal masses $m_\uparrow = m_\downarrow = m$ and generalize our discussion to the unequal mass case in Chap. 5.

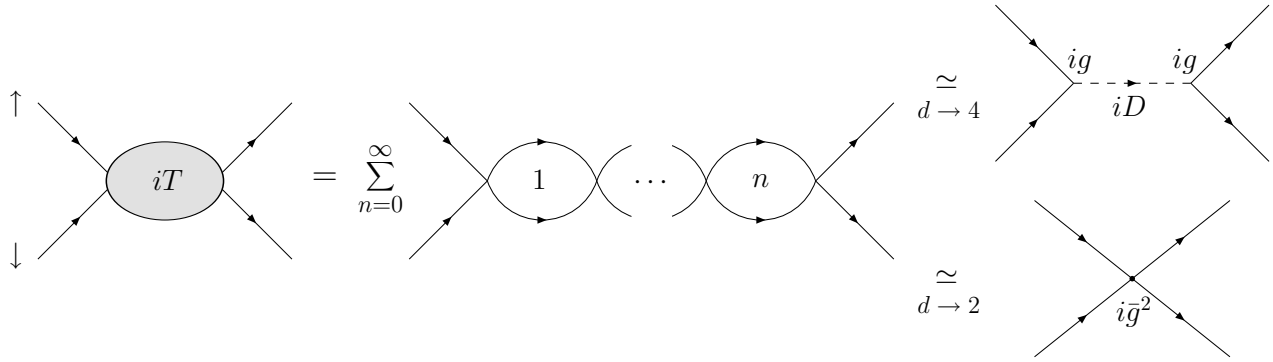

Figure 2.1: Two-fermion scattering in vacuum in the unitarity limit. The T-matrix near four spatial dimensions is expressed by the propagation of boson with the small effective coupling g, while it reduces to a contact interaction with the small effective coupling $\bar{g}^2$ near two spatial dimensions.

The T-matrix of the two-body scattering is given by the geometric series of bubble diagrams depicted in Fig. 2.1. As a result of the summation, its inverse can be written as

$$\begin{aligned} T(p_0,\boldsymbol{p})^{-1} &= \frac{1}{c_0} + i\int \frac{dk_0 d\boldsymbol{k}}{(2\pi)^{d+1}} \frac{1}{\frac{p_0}{2} - k_0 - \varepsilon_{\frac{\boldsymbol{p}}{2}-\boldsymbol{k}} + i\delta} \frac{1}{\frac{p_0}{2} + k_0 - \varepsilon_{\frac{\boldsymbol{p}}{2}+\boldsymbol{k}} + i\delta} \\ &= \frac{1}{c_0} - \int \frac{d\boldsymbol{k}}{(2\pi)^d} \frac{1}{2\varepsilon_{\boldsymbol{k}} - p_0 + \frac{\varepsilon_{\boldsymbol{p}}}{2} - i\delta}, \end{aligned} \tag{2.3}$$

where $\varepsilon_{\boldsymbol{p}} = p^2/2m$ is the kinetic energy of non-relativistic particles. The integral in Eq. (2.3) is divergent and needs to be regularized. In this thesis we shall work in dimensional regularization: integrals are evaluated for those values of d where they converge [for the integral in Eq. (2.3) this corresponds to $d < 2$] and then analytically continued to other values of d. In this regularization scheme, the integral in Eq. (2.3) vanishes for $p_0 = \boldsymbol{p} = 0$ (scatterings at threshold). Therefore the limit of infinite scattering length where $T(0,\boldsymbol{0}) = \infty$ corresponds to $c_0 = \infty$.

The integration over $\boldsymbol{k}$ in Eq. (2.3) can be evaluated explicitly

$$T(p_0,\boldsymbol{p})^{-1} = -\Gamma\left(1-\frac{d}{2}\right)\left(\frac{m}{4\pi}\right)^{\frac{d}{2}}\left(-p_0 + \frac{\varepsilon_{\boldsymbol{p}}}{2} - i\delta\right)^{\frac{d}{2}-1}. \tag{2.4}$$

This expression has a pole at $d = 4$ originating from the ultraviolet divergence of the $\boldsymbol{k}$ integration. Substituting $d = 4-\epsilon$ and expanding in terms of ϵ, the T-matrix near four spatial dimensions becomes

$$iT(p_0,\boldsymbol{p}) = -\frac{8\pi^2\epsilon}{m^2}\frac{i}{p_0 - \frac{\varepsilon_{\boldsymbol{p}}}{2} + i\delta} + O(\epsilon^2). \tag{2.5}$$

If we define

$$g^2 = \frac{8\pi^2\epsilon}{m^2} \tag{2.6}$$

and

$$D(p_0,\boldsymbol{p}) = \left(p_0 - \frac{\varepsilon_{\boldsymbol{p}}}{2} + i\delta\right)^{-1}. \tag{2.7}$$

the T-matrix, to leading order in ϵ, can be written as

$$iT(p_0, \boldsymbol{p}) \simeq (ig)^2 iD(p_0, \boldsymbol{p}). \tag{2.8}$$

The function $D(p_0, \boldsymbol{p})$ is the propagator of a particle with mass $2m$. It is natural to interpret this particle a bound state of two fermions at threshold. We will refer to this particle simply as the *boson*. Eq. (2.8) states that the two-fermion scattering near four spatial dimensions can be thought of as a process that occurs through the propagation of an intermediate boson, as depicted in Fig. 2.1. The effective coupling of two fermions into the boson is given by g. An important point is that the effective coupling $g \sim \epsilon^{1/2}$ is small near four dimensions. This fact indicates the possibility to construct a perturbative expansion for the unitary Fermi gas near four spatial dimensions in terms of the small parameter ϵ.

2.2 Near two spatial dimensions

Similarly, the perturbative expansion around two spatial dimensions is possible. This is because the inverse of T-matrix in Eq. (2.4) has another pole at $d = 2$. Substituting $d = 2 + \bar{\epsilon}$ and expanding in terms of $\bar{\epsilon}$, the T-matrix near two spatial dimensions becomes

$$iT(p_0, \boldsymbol{p}) = i\frac{2\pi}{m}\bar{\epsilon} + O(\bar{\epsilon}^2). \tag{2.9}$$

If we define the effective coupling at $2 + \bar{\epsilon}$ dimensions as

$$\bar{g}^2 = \frac{2\pi}{m}\bar{\epsilon}, \tag{2.10}$$

the T-matrix to the leading order in $\bar{\epsilon}$ can be written as

$$iT(p_0, \boldsymbol{p}) \simeq i\bar{g}^2. \tag{2.11}$$

We see that the T-matrix near two spatial dimensions reduces to that of a contact interaction with the small effective coupling $\bar{g}^2 \sim \bar{\epsilon}$ as depicted in Fig. 2.1. In this case, the boson propagator $D(p)$ in Eq. (2.8) corresponds to just a constant -1. We note that the same effective couplings near four and two spatial dimensions in Eqs. (2.6) and (2.10) can be obtained by the fixed point of the renormalization group flow describing the unitarity limit [97, 98]. We defer our discussion of the expansion over $\bar{\epsilon} = d - 2$ to Chap. 6 and concentrate on the expansion over $\epsilon = 4 - d$.

2.3 Binding energy of two-body state

We shall be interested not only in the physics right at the unitarity point, but also in the vicinity of it. In other words, we shall assume that $1/c_0$ can be nonzero in dimensional regularization. The case of $c_0 < 0$ corresponds to the BEC side of the unitarity point, and $c_0 > 0$ corresponds to the BCS side.

To facilitate a comparison with the physics in three dimensions, we shall find the relation between the coupling c_0, assuming that we are on the BEC side, $c_0 < 0$, and the binding energy of the two-body state at arbitrary spatial dimensions $2 < d < 4$.

The binding energy ε_b, defined to be positive $\varepsilon_b > 0$, is obtained as the location of the pole of the T-matrix at zero external momentum: $T(-\varepsilon_b, \mathbf{0})^{-1} = 0$. From Eqs. (2.3) and (2.4), we see c_0 is related with ε_b via the following equation

$$\frac{1}{c_0} = \Gamma\left(1 - \frac{d}{2}\right)\left(\frac{m}{4\pi}\right)^{\frac{d}{2}} \varepsilon_b^{\frac{d}{2}-1}. \tag{2.12}$$

Near four spatial dimensions, the relationship between ε_b and c_0 to the next-to-leading order in $\epsilon = 4 - d$ is given by

$$\frac{1}{c_0} \simeq -\frac{\varepsilon_b}{2\epsilon}\left(\frac{m}{2\pi}\right)^2 \left[1 + \frac{\epsilon}{2}(1-\gamma)\right]\left(\frac{m\varepsilon_b}{4\pi}\right)^{-\frac{\epsilon}{2}}. \tag{2.13}$$

In three spatial dimensions, the relationship between ε_b and the scattering length $a = -mc_0/4\pi$ becomes $\varepsilon_b = (ma^2)^{-1}$. If we recall that the Fermi energy is related to k_F through $\varepsilon_F = k_F^2/(2m)$, one finds the following relationship holds at $d = 3$:

$$\frac{\varepsilon_b}{\varepsilon_F} = \frac{2}{(ak_F)^2}. \tag{2.14}$$

We will use these relations to compare results in the expansion over $\epsilon = 4 - d$ with the physics at three spatial dimensions.

Chapter 3

Unitary Fermi gas around four spatial dimensions

3.1 Lagrangian and Feynman rules

Employing the idea of the previous Chapter, we now construct the ϵ expansion for the Fermi gas near the unitarity limit. We start with the Lagrangian density in Eq. (2.2) with chemical potentials $\mu_\uparrow$ and $\mu_\downarrow$ introduced to two different components:

$$\mathcal{L} = \sum_{\sigma=\uparrow,\downarrow} \psi_\sigma^\dagger \left(i\partial_t + \frac{\boldsymbol{\nabla}^2}{2m} + \mu_\sigma \right) \psi_\sigma + c_0\, \psi_\uparrow^\dagger \psi_\downarrow^\dagger \psi_\downarrow \psi_\uparrow . \tag{3.1}$$

After making the Hubbard–Stratonovich transformation [107, 108], the Lagrangian density in the Nambu–Gor'kov formalism can be written as

$$\mathcal{L} = \Psi^\dagger \left(i\partial_t + \frac{\sigma_3 \boldsymbol{\nabla}^2}{2m} + \mu\sigma_3 + H \right) \Psi - \frac{1}{c_0}\phi^*\phi + \Psi^\dagger \sigma_+ \Psi \phi + \Psi^\dagger \sigma_- \Psi \phi^*, \tag{3.2}$$

where $\Psi = (\psi_\uparrow, \psi_\downarrow^\dagger)^T$ is a two-component Nambu–Gor'kov field, and $\sigma_{1,2,3}$ and $\sigma_\pm = \frac{1}{2}(\sigma_1 \pm i\sigma_2)$ are the Pauli matrices [110, 109]. We define the average chemical potential as $\mu = (\mu_\uparrow + \mu_\downarrow)/2$ and the chemical potential difference as $H = (\mu_\uparrow - \mu_\downarrow)/2$.

The ground state at finite density system (at least when $H = 0$) is a superfluid state where ϕ condenses: $\langle\phi\rangle = \phi_0$ with ϕ_0 being chosen to be real. With that in mind we expand ϕ around its vacuum expectation value ϕ_0 as

$$\phi = \phi_0 + g\varphi, \qquad g = \frac{(8\pi^2\epsilon)^{1/2}}{m} \left(\frac{m\phi_0}{2\pi} \right)^{\epsilon/4} . \tag{3.3}$$

Here we introduced the effective coupling $g \sim \epsilon^{1/2}$ in Eq. (2.6). The extra factor $(m\phi_0/2\pi)^{\epsilon/4}$ was chosen so that φ has the same dimension as a non-relativistic field [1]. Since the Lagrangian density in

[1] The choice of the extra factor is arbitrary, if it has the correct dimension, and does not affect the final results because the difference can be absorbed into the redefinition of the fluctuation field φ. The particular choice of g in Eq. (3.3) will simplify the form of loop integrals in the intermediate steps.

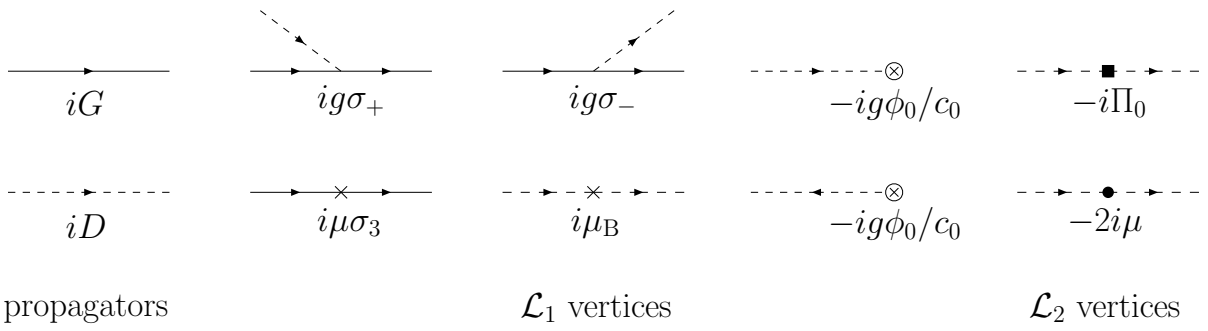

Figure 3.1: Feynman rules from the Lagrangian density in Eq. (3.4). The two vertices on the last column come from $\mathcal{L}_2$, while the rest from $\mathcal{L}_1$. Solid (dotted) lines represent the fermion (boson) propagator iG (iD).

Eq. (3.2) does not have the kinetic term for the boson field φ, we add and subtract its kinetic part by hand. In other words, we rewrite the Lagrangian density as a sum of three parts, $\mathcal{L} = \mathcal{L}_0 + \mathcal{L}_1 + \mathcal{L}_2$, where

$$\mathcal{L}_0 = \Psi^\dagger \left(i\partial_t + H + \frac{\sigma_3 \boldsymbol{\nabla}^2}{2m} + \sigma_+ \phi_0 + \sigma_- \phi_0 \right) \Psi + \varphi^* \left(i\partial_t + \frac{\boldsymbol{\nabla}^2}{4m} \right) \varphi - \frac{\phi_0^2}{c_0}\,, \tag{3.4}$$

$$\mathcal{L}_1 = g\Psi^\dagger \sigma_+ \Psi \varphi + g\Psi^\dagger \sigma_- \Psi \varphi^* + \mu \Psi^\dagger \sigma_3 \Psi + \left(2\mu - \frac{g^2}{c_0} \right) \varphi^* \varphi - \frac{g\phi_0}{c_0} \varphi - \frac{g\phi_0}{c_0} \varphi^*\,, \tag{3.5}$$

$$\mathcal{L}_2 = -\varphi^* \left(i\partial_t + \frac{\boldsymbol{\nabla}^2}{4m} \right) \varphi - 2\mu \varphi^* \varphi\,. \tag{3.6}$$

As we shall soon see, ϕ_0 coincides, to leading order in ϵ, to the energy gap in the fermion spectrum. In the unitarity limit, we have $g^2/c_0 = 0$. When c_0 is finite and negative, $-g^2/c_0 \simeq \varepsilon_{\rm b}$ gives the binding energy of boson to the leading order in ϵ from Eq. (2.13). Throughout this thesis, we consider the vicinity of the unitarity point where g^2/c_0 can be treated as a small quantity [2].

The part $\mathcal{L}_0$ represents the Lagrangian density of non-interacting fermion quasiparticles and bosons with the mass $2m$, whose kinetic terms are introduced by hand in $\mathcal{L}_0$ and taken out in $\mathcal{L}_2$. The propagators of fermion and boson are generated by $\mathcal{L}_0$. The fermion propagator G is a 2×2 matrix,

$$G(p_0, \boldsymbol{p}) = \frac{1}{(p_0 + H)^2 - E_{\boldsymbol{p}}^2 + i\delta} \begin{pmatrix} p_0 + H + \varepsilon_{\boldsymbol{p}} & -\phi_0 \\ -\phi_0 & p_0 + H - \varepsilon_{\boldsymbol{p}} \end{pmatrix}, \tag{3.7}$$

where $E_{\boldsymbol{p}} = \sqrt{\varepsilon_{\boldsymbol{p}}^2 + \phi_0^2}$ is the excitation energy of the fermion quasiparticle. We use the $i\delta$ prescription where $\delta = 0^+$ for positive p_0 while $\delta = 0^-$ for negative p_0. The boson propagator D is given by the same form as in Eq. (2.7),

$$D(p_0, \boldsymbol{p}) = \left(p_0 - \frac{\varepsilon_{\boldsymbol{p}}}{2} + i\delta \right)^{-1}. \tag{3.8}$$

[2] The precise meaning of the "small quantity" here is that g^2/c_0 compared to ϕ_0 is of the order ϵ, $g^2/c_0 \sim \epsilon\phi_0$.

$O(\epsilon^{-1})$	N (fermion density)
$O(\epsilon^{-1/2})$	$\varepsilon_{\rm F}$ (Fermi energy)
$O(1)$	ϕ_0 (condensate), Δ (energy gap)
	P (pressure), E (energy density)
$O(\epsilon)$	μ, $\mu_{\rm B}$ (chemical potentials)

Table 3.1: Summary of powers of ϵ in various quantities at zero temperature when the condensate ϕ_0 is regarded as $O(1)$.

The parts $\mathcal{L}_1$ and $\mathcal{L}_2$ generate the vertices which are depicted in Fig. 3.1. The first two terms in $\mathcal{L}_1$ represent the fermion-boson interactions, whose coupling is proportional to g and small in the limit $\epsilon \to 0$. This coupling originates from the two-body scattering in vacuum in the unitarity limit which was studied in the previous Chapter (see Fig. 2.1). The third and fourth terms are insertions of chemical potentials, μ and the boson chemical potential

$$\mu_{\rm B} \equiv 2\mu - \frac{g^2}{c_0}, \tag{3.9}$$

to the fermion and boson propagators, respectively. We treat these two terms as perturbations because μ will turn out to be small, $\mu/\phi_0 \sim \epsilon$, and we limit ourselves to the vicinity of the unitarity point where we can regard g^2/c_0 to be so small that $\mu_{\rm B}/\phi_0 \sim \epsilon$. The last two terms in $\mathcal{L}_1$ give tadpoles to the φ and φ^* fields, which are proportional to $-ig\phi_0/c_0$. The condition of cancellation of tadpole diagrams will determine the value of the condensate ϕ_0.

Finally, we treat the two terms in $\mathcal{L}_2$ as additional vertices for the boson propagator as depicted in the last column of Fig. 3.1, which are proportional to $-i\Pi_0$ and $-2i\mu$ where

$$\Pi_0(p_0, \boldsymbol{p}) = p_0 - \frac{\varepsilon_{\boldsymbol{p}}}{2}. \tag{3.10}$$

These two vertices play roles of counter terms so as to avoid double counting of certain types of diagrams which are already taken into $\mathcal{L}_0$ and $\mathcal{L}_1$. In the latter part of this Chapter, we will consider the unpolarized case with $H = 0$ at zero temperature.

3.2 Power counting rule of ϵ

Near unitarity, we can use the same power counting rule of ϵ developed in the unitarity limit [93]. Let us first consider Feynman diagrams constructed only from $\mathcal{L}_0$ and $\mathcal{L}_1$, without the vertices from $\mathcal{L}_2$. We make a prior assumption $\mu/\phi_0 \sim \epsilon$, which will be checked later, and consider ϕ_0 to be $O(1)$. Each pair of boson-fermion vertices is proportional to $g^2 \sim \epsilon$ and hence brings a factor of ϵ. Also, each insertion of $\mu \sim \epsilon$ or $\mu_{\rm B} = 2\mu - g^2/c_0 \sim \epsilon$ brings another factor of ϵ. Therefore the naive power of ϵ for a given diagram is $N_g/2 + N_\mu$, where N_g is the number of couplings g from $\mathcal{L}_1$. $N_\mu = N_{\mu_{\rm F}} + N_{\mu_{\rm B}}$ is the sum of the number of μ insertions to the fermion line and $\mu_{\rm B}$ insertions to the boson line.

However, this naive counting does not take into account the fact that there might be inverse powers of ϵ coming from integrals which have ultraviolet divergences at $d = 4$. Each loop integral in the ultraviolet region behaves as

$$\int dp_0 d\boldsymbol{p} \sim \int d\boldsymbol{p}\, \varepsilon_{\boldsymbol{p}} \sim p^6, \tag{3.11}$$

while each fermion or boson propagator behaves, at worst, as $G(p) \sim p^{-2}$ or $D(p) \sim p^{-2}$. Therefore, a given diagram may diverges as $\sim p^{\mathcal{D}}$ with $\mathcal{D}$ being the superficial degree of divergence given by

$$\mathcal{D} = 6L - 2P_{\mathrm{F}} - 2P_{\mathrm{B}}. \tag{3.12}$$

Here L is the number of loop integrals and $P_{\mathrm{F(B)}}$ is the number of fermion (boson) propagators. From the similar argument to the relativistic field theories [111], one can derive the following relations including the number of external fermion (boson) lines $E_{\mathrm{F(B)}}$:

$$\begin{aligned} L &= (P_{\mathrm{F}} - N_{\mu_{\mathrm{F}}}) + (P_{\mathrm{B}} - N_{\mu_{\mathrm{B}}}) - N_g + 1, \\ N_g &= (P_{\mathrm{F}} - N_{\mu_{\mathrm{F}}}) + \frac{E_{\mathrm{F}}}{2} = 2(P_{\mathrm{B}} - N_{\mu_{\mathrm{B}}}) + E_{\mathrm{B}}. \end{aligned} \tag{3.13}$$

With the use of these relations, the superficial degree of divergence $\mathcal{D}$ is written as

$$\mathcal{D} = 6 - 2(E_{\mathrm{F}} + E_{\mathrm{B}} + N_\mu), \tag{3.14}$$

which shows that the inverse powers of ϵ appear only in diagrams with no more than three external lines and chemical potential insertions. This is similar to the situation in quantum electrodynamics where infinities occur only in electron and photon self-energies and the electron-photon triple vertex.

However, this estimation of $\mathcal{D}$ is actually an over-estimate: for many diagrams the real degree of divergence is smaller than given in Eq. (3.14). To see that we split $G(p)$ into the retarded and advanced parts, $G(p) = G^{\mathrm{R}}(p) + G^{\mathrm{A}}(p)$, where G^{R} (G^{A}) has poles only in the lower (upper) half of the complex p_0 plane:

$$\begin{aligned} G_{11}(p) &= \frac{p_0 + \varepsilon_{\boldsymbol{p}}}{p_0^2 - E_{\boldsymbol{p}}^2 + i\delta} = \frac{E_{\boldsymbol{p}} + \varepsilon_{\boldsymbol{p}}}{2E_{\boldsymbol{p}}(p_0 - E_{\boldsymbol{p}} + i\delta)} + \frac{E_{\boldsymbol{p}} - \varepsilon_{\boldsymbol{p}}}{2E_{\boldsymbol{p}}(p_0 + E_{\boldsymbol{p}} - i\delta)}, \\ G_{22}(p) &= \frac{p_0 - \varepsilon_{\boldsymbol{p}}}{p_0^2 - E_{\boldsymbol{p}}^2 + i\delta} = \frac{E_{\boldsymbol{p}} - \varepsilon_{\boldsymbol{p}}}{2E_{\boldsymbol{p}}(p_0 - E_{\boldsymbol{p}} + i\delta)} + \frac{E_{\boldsymbol{p}} + \varepsilon_{\boldsymbol{p}}}{2E_{\boldsymbol{p}}(p_0 + E_{\boldsymbol{p}} - i\delta)}, \\ G_{12}(p) = G_{21}(p) &= \frac{-\phi_0}{p_0^2 - E_{\boldsymbol{p}}^2 + i\delta} = \frac{-\phi_0}{2E_{\boldsymbol{p}}(p_0 - E_{\boldsymbol{p}} + i\delta)} + \frac{-\phi_0}{2E_{\boldsymbol{p}}(p_0 + E_{\boldsymbol{p}} - i\delta)}. \end{aligned} \tag{3.15}$$

From these expressions, it is easy to see that the ultraviolet behaviors of different components of the propagators are different:

$$\begin{aligned} &G_{11}^{\mathrm{R}}(p) \sim G_{22}^{\mathrm{A}}(p) \sim D^{\mathrm{R}}(p) \sim p^{-2}, \\ &G_{12}^{\mathrm{R,A}}(p) \sim G_{21}^{\mathrm{R,A}}(p) \sim p^{-4}, \qquad G_{11}^{\mathrm{A}}(p) \sim G_{22}^{\mathrm{R}}(p) \sim p^{-6}. \end{aligned} \tag{3.16}$$

Note that the boson propagator $D(p)$ has a pole on the lower half plane of p_0, we have only the retarded Green's function for boson, $D^{\mathrm{A}}(p) = 0$.

From these analytic properties of the propagators in the ultraviolet region and the vertex structures in $\mathcal{L}_1$ as well as the relation of Eq. (3.14), one can show that there are only four skeleton diagrams which have the $1/\epsilon$ singularity near four dimensions. They are one-loop diagrams of the boson self-energy [Figs. 3.2(a) and 3.2(c)], the φ tadpole [Fig. 3.2(e)], and the vacuum diagram [Fig. 3.2(g)]. We shall examine these apparent four exceptions of naive power counting rule of ϵ one by one.

The first diagram, Fig. 3.2(a), is the one-loop diagram of the boson self-energy. The frequency integral can be done explicitly, yielding

$$\begin{aligned} -i\Pi_{\mathrm{a}}(p) &= -g^2 \int \frac{dk}{(2\pi)^{d+1}} G_{11}\Big(k+\frac{p}{2}\Big) G_{22}\Big(k-\frac{p}{2}\Big) \\ &= ig^2 \int \frac{d\boldsymbol{k}}{(2\pi)^d} \frac{1}{4E_{\boldsymbol{k}-\frac{\boldsymbol{p}}{2}} E_{\boldsymbol{k}+\frac{\boldsymbol{p}}{2}}} \\ &\quad \times \left[\frac{(E_{\boldsymbol{k}-\frac{\boldsymbol{p}}{2}} + \varepsilon_{\boldsymbol{k}-\frac{\boldsymbol{p}}{2}})(E_{\boldsymbol{k}+\frac{\boldsymbol{p}}{2}} + \varepsilon_{\boldsymbol{k}+\frac{\boldsymbol{p}}{2}})}{E_{\boldsymbol{k}-\frac{\boldsymbol{p}}{2}} + E_{\boldsymbol{k}+\frac{\boldsymbol{p}}{2}} - p_0 - i\delta} + \frac{(E_{\boldsymbol{k}-\frac{\boldsymbol{p}}{2}} - \varepsilon_{\boldsymbol{k}-\frac{\boldsymbol{p}}{2}})(E_{\boldsymbol{k}+\frac{\boldsymbol{p}}{2}} - \varepsilon_{\boldsymbol{k}+\frac{\boldsymbol{p}}{2}})}{E_{\boldsymbol{k}-\frac{\boldsymbol{p}}{2}} + E_{\boldsymbol{k}+\frac{\boldsymbol{p}}{2}} + p_0 - i\delta} \right]. \end{aligned} \tag{3.17}$$

The integral over $\boldsymbol{k}$ is ultraviolet divergent at $d = 4$ and has a pole at $\epsilon = 0$. Thus it is $O(1)$ by itself instead of $O(\epsilon)$ according to the naive counting. The residue at the pole is

$$\begin{aligned} \Pi_{\mathrm{a}}(p) &= -g^2 \int \frac{d\boldsymbol{k}}{(2\pi)^d} \left(2\varepsilon_{\boldsymbol{k}} - p_0 + \frac{\varepsilon_{\boldsymbol{p}}}{2}\right)^{-1} + \cdots \\ &= -\left(p_0 - \frac{\varepsilon_{\boldsymbol{p}}}{2}\right) + O(\epsilon), \end{aligned} \tag{3.18}$$

which is cancelled out exactly by adding the vertex Π_0 in $\mathcal{L}_2$. Therefore the diagram of the type in Figs. 3.2(a), when combined with the vertex from $\mathcal{L}_2$ in Fig. 3.2(b), conforms to the naive ϵ power counting, i.e., is $O(\epsilon)$.

Similarly, the diagram in Fig. 3.2(c) representing the boson self-energy with one μ insertion is given by

$$-i\Pi_{\mathrm{c}}(p) = 2\mu\, g^2 \int \frac{dk}{(2\pi)^{d+1}} \left[G_{11}\Big(k+\frac{p}{2}\Big)^2 - G_{12}\Big(k+\frac{p}{2}\Big)^2 \right] G_{22}\Big(k-\frac{p}{2}\Big), \tag{3.19}$$

which also contains a $1/\epsilon$ singularity, and is $O(\epsilon)$ instead of the naive $O(\epsilon^2)$. The leading part of this diagram is

$$\begin{aligned} \Pi_{\mathrm{c}}(p) &= -2\mu\, g^2 \int \frac{d\boldsymbol{k}}{(2\pi)^d} \, (2\varepsilon_{\boldsymbol{k}})^{-2} + \cdots \\ &= -2\mu + O(\epsilon^2), \end{aligned} \tag{3.20}$$

and is cancelled out by the second vertex from $\mathcal{L}_2$. Then the sum of Figs. 3.2(c) and 3.2(d) is again $O(\epsilon^2)$, consistent with the naive power counting.

The φ tadpole diagram with one μ insertion in Fig. 3.2(e) is

$$\begin{aligned} \Xi_{\mathrm{e}} &= -\mu g \int \frac{dk}{(2\pi)^{d+1}} \left[G_{11}(k) - G_{22}(k) \right] G_{21}(k) \\ &= ig\mu\phi_0 \int \frac{d\boldsymbol{k}}{(2\pi)^d} \frac{\varepsilon_{\boldsymbol{k}}}{2E_k^3} = 2i\frac{\mu\phi_0}{g} + O(\epsilon^{3/2}), \end{aligned} \tag{3.21}$$

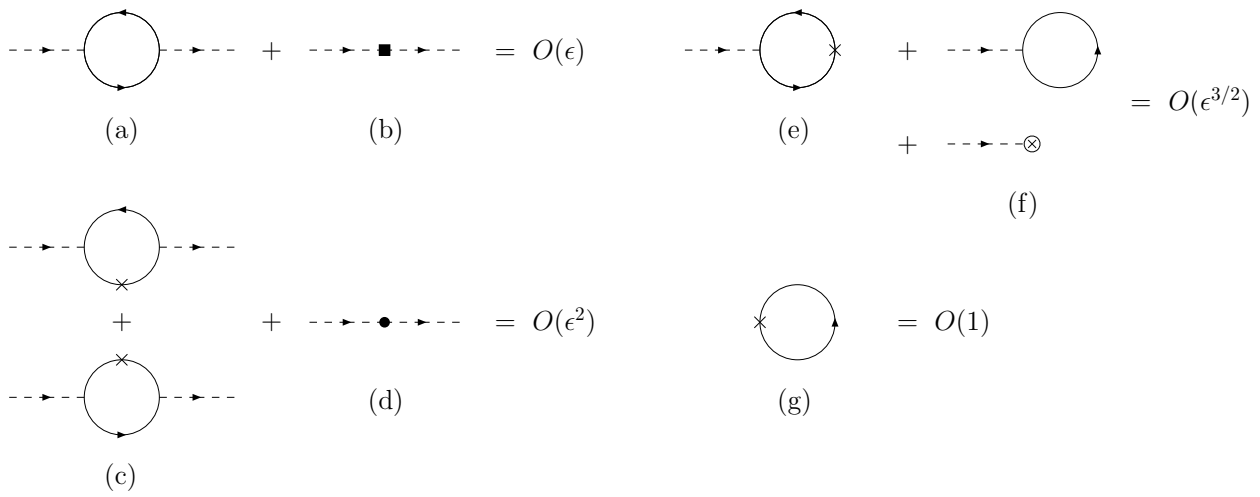

Figure 3.2: Four apparent exceptions of naive power counting rule of ϵ, (a, c, e, g). The boson self-energy diagram, (a) or (c), is combined with the vertex from $\mathcal{L}_2$, (b) or (d), to restore the naive ϵ counting. The tadpole diagram in (e) cancels with other tadpole diagrams at the minimum of the effective potential. The vacuum diagram (g) is the only exception of the naive power counting rule of ϵ, which is $O(1)$ instead of $O(\epsilon)$.

which is $O(\epsilon^{1/2})$ instead of the naive $O(\epsilon^{3/2})$. This tadpole diagram should be cancelled by other tadpole diagrams of order $O(\epsilon^{1/2})$ in Fig. 3.2(f),

$$\begin{aligned}\Xi_{\rm f} &= g\int\frac{dk}{(2\pi)^{d+1}}G_{21}(k) - i\frac{g\phi_0}{c_0}\\ &= -\frac{ig}{2}\left(\frac{m\phi_0}{2\pi}\right)^2 - i\frac{g\phi_0}{c_0} + O(\epsilon^{3/2}).\end{aligned} \tag{3.22}$$

The condition of cancellation, $\Xi_{\rm e} + \Xi_{\rm f} = 0$, gives the gap equation to determine $\phi_0(\mu)$ to the leading order in ϵ. The solution to the gap equation is

$$\phi_0 = \frac{2\mu}{\epsilon} - \frac{2}{c_0}\left(\frac{2\pi}{m}\right)^2 + O(\epsilon). \tag{3.23}$$

When $c_0 < 0$, this solution can be written in terms of the binding energy $\varepsilon_{\rm b}$ as $\phi_0 = (2\mu + \varepsilon_{\rm b})/\epsilon$. Now the previously made assumption $\mu/\phi_0 = O(\epsilon)$ is checked. The condition of cancellation of tadpole diagrams is automatically satisfied by the minimization of the effective potential as we will see later.

Finally, the one-loop vacuum diagram with one μ insertion in Fig. 3.2(g) also contains the $1/\epsilon$ singularity as

$$\begin{aligned}i\mu\int\frac{dk}{(2\pi)^{d+1}}\left[G_{11}(k) - G_{22}(k)\right] &= \mu\int\frac{d\boldsymbol{k}}{(2\pi)^d}\frac{\varepsilon_{\boldsymbol{k}}}{E_{\boldsymbol{k}}}\\ &= -\frac{\mu}{\epsilon}\left(\frac{m\phi_0}{2\pi}\right)^2 + O(\epsilon).\end{aligned} \tag{3.24}$$

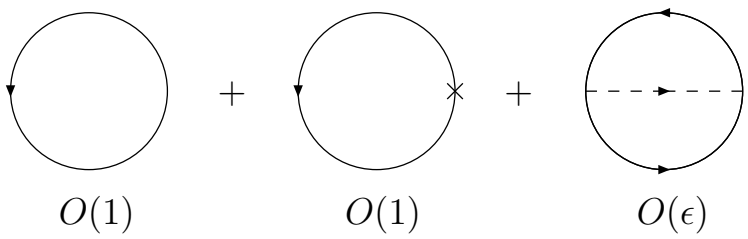

Figure 3.3: Vacuum diagrams contributing to the effective potential up to the next-to-leading order in ϵ. The second diagram is $O(1)$ instead of naive $O(\epsilon)$ because of the $1/\epsilon$ singularity.

The leading part of this diagram is $O(1)$ instead of naive $O(\epsilon)$ and can not be cancelled by any other diagrams. Therefore, Fig. 3.2(g) $\sim O(1)$ is the only exception of our naive power counting rule of ϵ.

Thus, we can now develop a diagrammatic technique for the Fermi gas near the unitarity limit where $g^2/|c_0| \sim \mu$ in terms of the systematic expansion of $\epsilon = 4 - d$. The power counting rule of ϵ is summarized as follow:

1. We consider $\mu/\phi_0 \sim \epsilon$ and regard ϕ_0 as $O(1)$.

2. For any Green's function, we write down all Feynman diagrams according to the Feynman rules in Fig. 3.1 using the propagators from $\mathcal{L}_0$ and the vertices from $\mathcal{L}_1$.

3. If there is any subdiagram of the type in Fig. 3.2(a) or Fig. 3.2(c), we add a diagram where the subdiagram is replaced by a vertex from $\mathcal{L}_2$, Fig. 3.2(b) or Fig. 3.2(d).

4. The power of ϵ for the given Feynman diagram will be $O(\epsilon^{N_g/2+N_\mu})$, where N_g is the number of couplings g and N_μ is the number of chemical potential insertions.

5. The only exception is the one-loop vacuum diagram with one μ insertion in Fig. 3.2(g), which is $O(1)$ instead of the naive $O(\epsilon)$.

We note that the sum of all tadpole diagrams in Figs. 3.2(e) and 3.2(f) vanishes with the solution of the gap equation ϕ_0.

3.3 Effective potential to leading and next-to-leading orders

We now perform calculations to leading and next-to-leading orders in ϵ, employing the Feynman rules and the ϵ power counting that have just been developed. To find the dependence of ϕ_0 on μ, we use the effective potential method [111] in which this dependence follows from the the minimization of the effective potential $V_{\text{eff}}(\phi_0)$. The effective potential at the tree level is given by

$$V_0(\phi_0) = \frac{\phi_0^2}{c_0}. \tag{3.25}$$

Up to the next-to-leading order, the effective potential receives contributions from three vacuum diagrams drawn in Fig. 3.3: fermion loops with and without a μ insertion and a fermion loop with one boson exchange.

The contributions from two one-loop diagrams are $O(1)$ and given by

$$\begin{aligned} V_1(\phi_0) &= i\int \frac{dp}{(2\pi)^{d+1}} \mathrm{Tr}\left[\ln G^{-1}(p) + \mu\sigma_3 G(p)\right] \\ &= -\int \frac{d\boldsymbol{p}}{(2\pi)^d}\left(E_{\boldsymbol{p}} - \mu\frac{\varepsilon_{\boldsymbol{p}}}{E_{\boldsymbol{p}}}\right). \end{aligned} \tag{3.26}$$

By changing the integration variable to $z = (\varepsilon_{\boldsymbol{p}}/\phi_0)^2$ and with the use of the formula

$$\int_0^\infty dz\, \frac{z^{\alpha-1}}{(z+1)^\beta} = \frac{\Gamma(\alpha)\Gamma(\beta-\alpha)}{\Gamma(\beta)}, \tag{3.27}$$

we can perform the integration over $\boldsymbol{p}$ that results in

$$V_1(\phi_0) = -\frac{\left(\frac{m\phi_0}{2\pi}\right)^{\frac{d}{2}}}{2\Gamma(\frac{d}{2})}\left[\frac{\Gamma(\frac{d}{4})\Gamma(-\frac{1}{2}-\frac{d}{4})}{\Gamma(-\frac{1}{2})}\phi_0 - \frac{\Gamma(\frac{d}{4}+\frac{1}{2})\Gamma(-\frac{d}{4})}{\Gamma(\frac{1}{2})}\mu\right]. \tag{3.28}$$

Substituting $d = 4-\epsilon$ and expanding in terms of ϵ up to $O(\epsilon)$, we obtain the effective potential from the one-loop diagrams as

$$V_1(\phi_0) = \frac{\phi_0}{3}\left[1 + \frac{7-3(\gamma+\ln 2)}{6}\epsilon\right]\left(\frac{m\phi_0}{2\pi}\right)^{d/2} - \frac{\mu}{\epsilon}\left[1 + \frac{1-2(\gamma-\ln 2)}{4}\epsilon\right]\left(\frac{m\phi_0}{2\pi}\right)^{d/2} + O(\epsilon^2), \tag{3.29}$$

where $\gamma \approx 0.57722$ is the Euler-Mascheroni constant.

The contribution of the two-loop diagram is $O(\epsilon)$ and given by

$$\begin{aligned} V_2(\phi_0) &= g^2\int \frac{dp\,dq}{(2\pi)^{2d+2}} \mathrm{Tr}\left[G(p)\sigma_+ G(q)\sigma_-\right] D(p-q) \\ &= g^2\int \frac{dp\,dq}{(2\pi)^{2d+2}} G_{11}(p)G_{22}(q)D(p-q). \end{aligned} \tag{3.30}$$

Performing the integrations over p_0 and q_0, we obtain

$$V_2(\phi_0) = -\frac{g^2}{4}\int \frac{d\boldsymbol{p}\,d\boldsymbol{q}}{(2\pi)^{2d}} \frac{(E_{\boldsymbol{p}}-\varepsilon_{\boldsymbol{p}})(E_{\boldsymbol{q}}-\varepsilon_{\boldsymbol{q}})}{E_{\boldsymbol{p}}E_{\boldsymbol{q}}(E_{\boldsymbol{p}}+E_{\boldsymbol{q}}+\varepsilon_{\boldsymbol{p}-\boldsymbol{q}}/2)}. \tag{3.31}$$

Since this is a next-to-leading order diagram and the integral converges at $d = 4$, we can evaluate it at $d = 4$. Changing the integration variables to $x = \varepsilon_{\boldsymbol{p}}/\phi_0$, $y = \varepsilon_{\boldsymbol{q}}/\phi_0$, and $\cos\theta = \hat{\boldsymbol{p}}\cdot\hat{\boldsymbol{q}}$, the integral can be expressed by

$$V_2(\phi_0) = -\epsilon\left(\frac{m\phi_0}{2\pi}\right)^{d/2}\frac{\phi_0}{\pi}\int_0^\infty dx\int_0^\infty dy\int_0^\pi d\theta\, xy\sin^2\theta\, \frac{[f(x)-x][f(y)-y]}{f(x)f(y)\left[g(x,y)-\sqrt{xy}\cos\theta\right]} \tag{3.32}$$

with $f(x) = \sqrt{x^2+1}$ and $g(x,y) = f(x)+f(y)+\frac{1}{2}(x+y)$. The integration over θ can be performed analytically to lead to

$$V_2(\phi_0) = -C\epsilon\left(\frac{m\phi_0}{2\pi}\right)^{d/2}\phi_0, \tag{3.33}$$

where the constant C is given by a two-dimensional integral

$$C = \int_0^\infty dx \int_0^\infty dy \, \frac{[f(x) - x][f(y) - y]}{f(x)f(y)} \left[g(x,y) - \sqrt{g^2(x,y) - xy} \right]. \tag{3.34}$$

The numerical integrations over x and y result in

$$C \approx 0.14424. \tag{3.35}$$

Now, gathering up Eqs. (3.25), (3.29), and (3.32), we obtain the effective potential up to the next-to-leading order in ϵ,

$$\begin{aligned} V_{\rm eff}(\phi_0) &= V_0(\phi_0) + V_1(\phi_0) + V_2(\phi_0) \\ &= \frac{\phi_0^2}{c_0} + \left[\frac{\phi_0}{3} \left\{ 1 + \frac{7 - 3(\gamma + \ln 2)}{6} \epsilon - 3C\epsilon \right\} - \frac{\mu}{\epsilon} \left\{ 1 + \frac{1 - 2(\gamma - \ln 2)}{4} \epsilon \right\} \right] \left(\frac{m\phi_0}{2\pi} \right)^{d/2} \\ &\quad + O(\epsilon^2). \end{aligned} \tag{3.36}$$

The condition of the minimization of the effective potential in terms of ϕ_0 gives the gap equation; $\partial V_{\rm eff}/\partial \phi_0 = 0$. The solution of the gap equation satisfies

$$\phi_0 = \frac{2\mu}{\epsilon} \left[1 + (3C - 1 + \ln 2)\, \epsilon \right] - \frac{2\phi_0^{\epsilon/2}}{c_0} \left(\frac{2\pi}{m} \right)^{d/2} \left[1 + \left(3C - 1 + \frac{\gamma + \ln 2}{2} \right) \epsilon \right]. \tag{3.37}$$

Using the relation of c_0 with the binding energy of boson $\varepsilon_{\rm b}$ in Eq. (2.12), we can rewrite the solution of the gap equation in terms of $\varepsilon_{\rm b}$ up to the next-to-leading order in ϵ as

$$\phi_0 = \frac{2\mu}{\epsilon} \left[1 + (3C - 1 + \ln 2)\, \epsilon \right] + \frac{\varepsilon_{\rm b}}{\epsilon} \left[1 + \left(3C - \frac{1}{2} + \ln 2 - \frac{1}{2} \ln \frac{\varepsilon_{\rm b}}{\phi_0} \right) \epsilon \right]. \tag{3.38}$$

We note that the leading term in Eq. (3.38) could be reproduced using the mean field approximation, but the $O(\epsilon)$ corrections are not. The $O(\epsilon)$ correction proportional to C is the result of the summation of fluctuations around the classical solution and is beyond the mean field approximation.

3.4 Thermodynamic quantities near unitarity

The value of the effective potential $V_{\rm eff}$ at its minimum determines the pressure $P = -V_{\rm eff}(\phi_0)$ at a given chemical potential μ and a given binding energy of boson $\varepsilon_{\rm b}$. Substituting the dependence of ϕ_0 on μ and $\varepsilon_{\rm b}$ in Eq. (3.38), we obtain the pressure as

$$P = \frac{\phi_0}{6} \left[1 + \left(\frac{17}{12} - 3C - \frac{\gamma + \ln 2}{2} \right) \epsilon - \frac{3\varepsilon_{\rm b}}{4\phi_0} \right] \left(\frac{m\phi_0}{2\pi} \right)^{d/2}. \tag{3.39}$$

The fermion number density N is determined by differentiating the pressure in terms of μ as

$$N = \frac{\partial P}{\partial \mu} = \frac{1}{\epsilon} \left[1 + \frac{1 - 2\gamma + 2\ln 2}{4} \epsilon \right] \left(\frac{m\phi_0}{2\pi} \right)^{d/2}. \tag{3.40}$$

Then the Fermi energy from the thermodynamic of free gas in d spatial dimensions is given by

$$\varepsilon_{\rm F} = \frac{2\pi}{m}\left[\frac{1}{2}\Gamma\left(\frac{d}{2}+1\right)N\right]^{2/d} = \frac{\phi_0}{\epsilon^{2/d}}\left(1-\frac{1-\ln 2}{4}\epsilon\right). \tag{3.41}$$

Note that non-trivial dependences on ϵ like $\sqrt{\epsilon}$ and $\ln\epsilon$ appear by taking $N\sim\epsilon^{-1}$ to the power of $2/d$.

From Eqs. (3.38) and (3.41), we can determine the ratio of the chemical potential and the Fermi energy $\mu/\varepsilon_{\rm F}$ near the unitary limit as

$$\frac{\mu}{\varepsilon_{\rm F}} = \frac{\epsilon^{3/2}}{2}\exp\left(\frac{\epsilon\ln\epsilon}{8-2\epsilon}\right)\left[1-\left(3C-\frac{5}{4}(1-\ln 2)\right)\epsilon\right] - \frac{\varepsilon_{\rm b}}{2\varepsilon_{\rm F}}\left[1+\frac{\epsilon}{2}+\frac{\epsilon\ln\epsilon}{4}-\frac{\epsilon}{2}\ln\frac{\varepsilon_{\rm b}}{\varepsilon_{\rm F}}\right]. \tag{3.42}$$

The logarithmic terms in the second line originates by introducing $\phi_0 = \epsilon^{1/2}\varepsilon_{\rm F}$ to the $\ln\varepsilon_{\rm b}/\phi_0$ term in Eq. (3.38). The first term in Eq. (3.42) gives the universal parameter of the unitary Fermi gas $\xi \equiv \mu/\varepsilon_{\rm F}|_{\varepsilon_{\rm b}=0}$ as

$$\begin{aligned}\xi &= \frac{\epsilon^{3/2}}{2}\left[1+\frac{\epsilon\ln\epsilon}{8}-\left(3C-\frac{5}{4}(1-\ln 2)\right)\epsilon\right] \\ &= \frac{1}{2}\epsilon^{3/2}+\frac{1}{16}\epsilon^{5/2}\ln\epsilon - 0.0246\,\epsilon^{5/2}+\cdots.\end{aligned} \tag{3.43}$$

Here we have substituted the numerical value for $C\approx 0.14424$ in Eq. (3.35). The smallness of the coefficient in front of $\epsilon^{5/2}$ is a result of the cancellation between the two-loop correction and the subleading terms from the expansion of the one-loop diagrams around $d=4$. The $O(\epsilon^{7/2})$ correction to the universal parameter ξ was recently computed to find the large correction $0.480\,\epsilon^{7/2}$ [102]. This may be related with the asymptotic nature of the ϵ expansion and some sort of resummation will be necessary to go beyond the next-to-leading order level.

Using Eqs. (3.39), (3.40), and (3.41), the pressure near the unitarity limit normalized by $\varepsilon_{\rm F}N$ is given by

$$\frac{P}{\varepsilon_{\rm F}N} = \frac{2}{d+2}\xi - \frac{\varepsilon_{\rm b}}{8\varepsilon_{\rm F}}\epsilon. \tag{3.44}$$

Then the energy density $E=\mu N-P$ can be calculated from Eqs. (3.42) and (3.44) as

$$\frac{E}{\varepsilon_{\rm F}N} = \frac{d}{d+2}\xi - \frac{\varepsilon_{\rm b}}{2\varepsilon_{\rm F}}\left[1+\frac{\epsilon}{4}+\frac{\epsilon\ln\epsilon}{4}-\frac{\epsilon}{2}\ln\frac{\varepsilon_{\rm b}}{\varepsilon_{\rm F}}\right]. \tag{3.45}$$

The pressure and energy density in the unitarity limit are obtained from ξ via the universal relations depending only on the dimensionality of space. Partial resummation of logarithmic terms of the binding energy $\ln(\varepsilon_{\rm b}/\varepsilon_{\rm F})$ change the exponent of $\varepsilon_{\rm b}/\varepsilon_{\rm F}$ to $(\varepsilon_{\rm b}/\varepsilon_{\rm F})^{1-\epsilon/2}$ [103].

3.5 Quasiparticle spectrum

The ϵ expansion we have developed is also useful for the calculations of physical observables other than the thermodynamic quantities. Here we shall look at the dispersion relation of fermion quasiparticles. To the leading order in ϵ, the dispersion relation is given by $\omega_{\rm F}(\boldsymbol{p}) = E_{\boldsymbol{p}} = \sqrt{\varepsilon_{\boldsymbol{p}}^2+\phi_0^2}$,

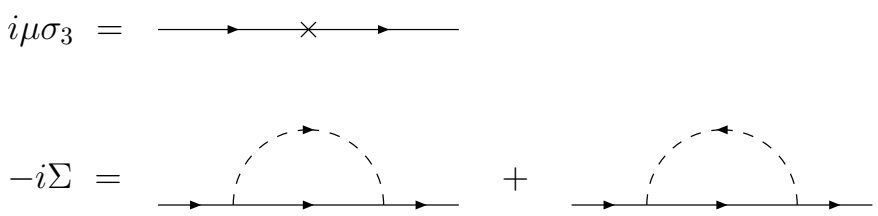

Figure 3.4: Corrections to the fermion self-energy of order $O(\epsilon)$; a μ insertion and one-loop diagrams.

which has a minimum at zero momentum $\boldsymbol{p} = \boldsymbol{0}$ with the energy gap equal to $\Delta = \phi_0 = (2\mu + \varepsilon_{\rm b})/\epsilon$. The next-to-leading order corrections to the dispersion relation come from three sources: from the correction of ϕ_0 in Eq. (3.38), from the μ insertion to the fermion propagator, and from the one-loop self-energy diagrams, $-i\Sigma(p)$, depicted in Fig. 3.4.

Using the Feynman rules, the one-loop diagram of the fermion self-energy in Fig. 3.4 is given by

$$-i\Sigma(p) = g^2 \int \frac{dk}{(2\pi)^{d+1}} \left[\sigma_+ G(k)\sigma_- D(p-k) + \sigma_- G(k)\sigma_+ D(k-p)\right]. \tag{3.46}$$

There are corrections only to the diagonal elements of the self-energy and each element is evaluated as

$$\begin{aligned}\Sigma_{11}(p) &= ig^2 \int \frac{dk}{(2\pi)^{d+1}} G_{22}(k) D(p-k) \\ &= -\frac{g^2}{2} \int \frac{d\boldsymbol{k}}{(2\pi)^d} \frac{E_{\boldsymbol{k}} - \varepsilon_{\boldsymbol{k}}}{E_{\boldsymbol{k}}(E_{\boldsymbol{k}} + \varepsilon_{\boldsymbol{k}-\boldsymbol{p}}/2 - p_0 - i\delta)},\end{aligned} \tag{3.47}$$

and

$$\begin{aligned}\Sigma_{22}(p) &= ig^2 \int \frac{dk}{(2\pi)^{d+1}} G_{11}(k) D(k-p) \\ &= \frac{g^2}{2} \int \frac{d\boldsymbol{k}}{(2\pi)^d} \frac{E_{\boldsymbol{k}} - \varepsilon_{\boldsymbol{k}}}{E_{\boldsymbol{k}}(E_{\boldsymbol{k}} + \varepsilon_{\boldsymbol{k}-\boldsymbol{p}}/2 + p_0 - i\delta)}.\end{aligned} \tag{3.48}$$

The dispersion relation of the fermion quasiparticle $\omega_{\rm F}(\boldsymbol{p})$ is obtained as a pole of the fermion propagator $\det[G^{-1}(\omega, \boldsymbol{p}) + \mu\sigma_3 - \Sigma(\omega, \boldsymbol{p})] = 0$, which reduces to the following equation:

$$\begin{vmatrix} \omega - \varepsilon_{\boldsymbol{p}} + \mu - \Sigma_{11}(\omega, \boldsymbol{p}) & \phi_0 \\ \phi_0 & \omega + \varepsilon_{\boldsymbol{p}} - \mu - \Sigma_{22}(\omega, \boldsymbol{p}) \end{vmatrix} = 0. \tag{3.49}$$

To find the $O(\epsilon)$ correction to the dispersion relation, we only have to evaluate the self-energy $\Sigma(\omega, \boldsymbol{p})$ with ω given by the leading order solution $\omega = E_{\boldsymbol{p}}$. Denoting $\Sigma_{11}(E_{\boldsymbol{p}}, \boldsymbol{p})$ and $\Sigma_{22}(E_{\boldsymbol{p}}, \boldsymbol{p})$ simply by Σ_{11} and Σ_{22} and solving Eq. (3.49) in terms of ω, we obtain the dispersion relation of the fermion quasiparticle as

$$\omega_{\rm F}(\boldsymbol{p}) = E_{\boldsymbol{p}} + \frac{\Sigma_{11} + \Sigma_{22}}{2} + \frac{\Sigma_{11} - \Sigma_{22} - 2\mu}{2E_{\boldsymbol{p}}} \varepsilon_{\boldsymbol{p}} + O(\epsilon^2). \tag{3.50}$$

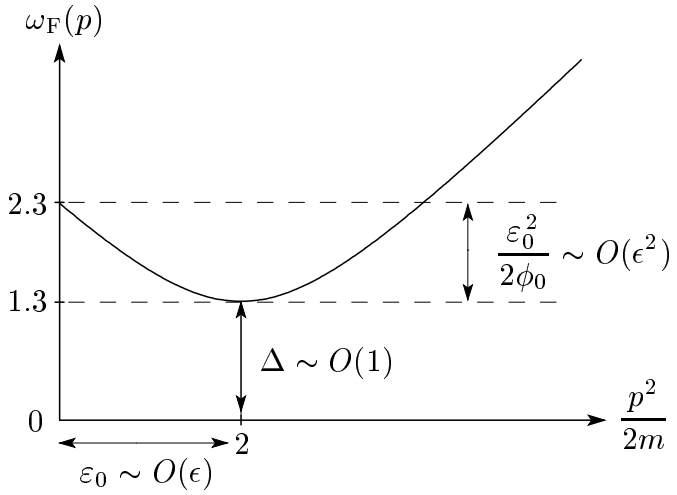

Figure 3.5: Illustration of the dispersion relation of the fermion quasiparticle in the unitarity limit from the ϵ expansion. $\omega_{\rm F}(\boldsymbol{p}) = \sqrt{(\varepsilon_{\boldsymbol{p}} - \varepsilon_0)^2 + \Delta^2}$ in Eq. (3.53) is plotted as a function of $\varepsilon_{\boldsymbol{p}} = p^2/2m$. Values on both axes are extrapolated results to $\epsilon = 1$ in units of the chemical potential μ.

Since the minimum of the dispersion relation will appear at small momentum $\varepsilon_{\boldsymbol{p}} \sim \mu$, we can expand $\Sigma(E_{\boldsymbol{p}}, \boldsymbol{p})$ around zero momentum $\boldsymbol{p} = 0$ as $\Sigma(E_{\boldsymbol{p}}, \boldsymbol{p}) = \Sigma^0(\phi_0, \boldsymbol{0}) + \Sigma'(\phi_0, \boldsymbol{0})\,\varepsilon_{\boldsymbol{p}}/\phi_0$ to find the energy gap of the fermion quasiparticles. Performing the integration over $\boldsymbol{k}$ in Σ analytically, we have

$$\Sigma_{11}(E_{\boldsymbol{p}}, \boldsymbol{p}) = \epsilon\,(2 - 8\ln 3 + 8\ln 2)\,\phi_0 + \epsilon\left(-\frac{8}{3} + 8\ln 3 - 8\ln 2\right)\varepsilon_{\boldsymbol{p}}, \tag{3.51}$$

and

$$\Sigma_{22}(E_{\boldsymbol{p}}, \boldsymbol{p}) = \epsilon\,(-2 - 8\ln 3 + 16\ln 2)\,\phi_0 + \epsilon\left(-\frac{7}{3} - 8\ln 3 + 16\ln 2\right)\varepsilon_{\boldsymbol{p}}. \tag{3.52}$$

Introducing these expressions into Eq. (3.50), we find the fermion dispersion relation around its minimum has the following form

$$\omega_{\rm F}(\boldsymbol{p}) \simeq \Delta + \frac{(\varepsilon_{\boldsymbol{p}} - \varepsilon_0)^2}{2\phi_0} \simeq \sqrt{(\varepsilon_{\boldsymbol{p}} - \varepsilon_0)^2 + \Delta^2}. \tag{3.53}$$

Here Δ is the energy gap of the fermion quasiparticle, which is given by

$$\begin{aligned} \Delta &= \phi_0 + \frac{\Sigma_{11}^0 + \Sigma_{22}^0}{2} \\ &= \left[1 - (8\ln 3 - 12\ln 2)\,\epsilon + O(\epsilon^2)\right]\phi_0. \end{aligned} \tag{3.54}$$

The minimum of the dispersion curve is located at a nonzero value of momentum, $|\boldsymbol{p}| = (2m\varepsilon_0)^{1/2}$, where

$$\begin{aligned} \varepsilon_0 &= \mu + \frac{\Sigma_{22}^0 - \Sigma_{11}^0}{2} - \frac{\Sigma_{11}' + \Sigma_{22}'}{2} \\ &= \mu + \frac{\epsilon\phi_0}{2} + O(\epsilon^2). \end{aligned} \tag{3.55}$$

Then, introducing the solution of the gap equation (3.38), the energy gap Δ as a function of the chemical potential and the binding energy is given by

$$\begin{aligned}\Delta &= \frac{2\mu}{\epsilon}\left[1+(3C-1-8\ln 3+13\ln 2)\epsilon\right]+\frac{\varepsilon_{\rm b}}{\epsilon}\left[1+\left(3C-\frac{1}{2}-8\ln 3+13\ln 2-\frac{1}{2}\ln\frac{\varepsilon_{\rm b}}{\Delta}\right)\epsilon\right]\\ &= \frac{2\mu}{\epsilon}\left(1-0.345\,\epsilon\right)+\frac{\varepsilon_{\rm b}}{\epsilon}\left(1+0.155\,\epsilon-\frac{\epsilon\ln\epsilon}{2}\right)+\frac{\varepsilon_{\rm b}}{2}\ln\left(1+\frac{2\mu}{\varepsilon_{\rm b}}\right),\end{aligned} \tag{3.56}$$

while ε_0 is given by

$$\varepsilon_0 = 2\mu+\frac{\varepsilon_{\rm b}}{2}. \tag{3.57}$$

Note the difference with the mean field approximation, in which $\varepsilon_0 = \mu$. When ε_0 is positive, the fermion dispersion curve has its minimum at nonzero value of momentum as in the BCS limit, while the minimum is located at zero momentum when ε_0 is negative as in the BEC limit. We find the former ($\varepsilon_0 = 2\mu > 0$) is the case in the unitarity limit. The dispersion curve of the fermion quasiparticle $\omega_{\rm F}(\boldsymbol{p})$ in the unitarity limit $\varepsilon_{\rm b} = 0$ is illustrated Fig 3.5. In particular, the difference between the fermion quasiparticle energy at zero momentum and at its minimum is given by $\varepsilon_0^2/2\phi_0 = \epsilon\mu \sim O(\epsilon^2)$.

3.6 Location of the splitting point

Let us consider the situation where the binding energy $\varepsilon_{\rm b}$ is increasing from zero while the number density N is kept fixed. Then $\Delta > 0$ is held fixed but μ is changing. Since to the leading order in ϵ, the chemical potential as a function of the energy gap is given by $2\mu = \epsilon\Delta - \varepsilon_{\rm b}$, the location of the minimum of the dispersion curve can be written as

$$\varepsilon_0 = \epsilon\Delta-\frac{\varepsilon_{\rm b}}{2}. \tag{3.58}$$

Therefore, ε_0 decreases as $\varepsilon_{\rm b}$ increases. When the binding energy reaches $\varepsilon_{\rm b} = 2\epsilon\Delta$, the minimum of the dispersion curve sits exactly at zero momentum $\boldsymbol{p} = \boldsymbol{0}$. This point is referred to as a *splitting point* [112]. We find the splitting point is located at the BEC side of the unitarity limit where the binding energy is positive $\varepsilon_{\rm b} = 2\epsilon\Delta > 0$ and the chemical potential is negative $2\mu = -\epsilon\Delta$. This splitting point will play an important role to determine the phase structure of the polarized Fermi gas in the unitary regime as we will study in Chap. 4.

3.7 Momentum distribution function

Other interesting observables which can be measured in experiments are a momentum distribution function of fermion quasiparticles [113, 114, 115, 116] and a condensate fraction in the fermion density [6, 7, 116, 117, 118]. The momentum distribution functions, $n_{\boldsymbol{p}\uparrow}$ and $n_{\boldsymbol{p}\downarrow}$, can be computed from the fermion propagator $\mathcal{G}(p)$ through

$$n_{\boldsymbol{p}\uparrow} = \int\frac{dp_0}{2\pi i}\,e^{ip_00^+}\mathcal{G}_{11}(p_0,\boldsymbol{p}) \qquad \text{and} \qquad n_{\boldsymbol{p}\downarrow} = -\int\frac{dp_0}{2\pi i}\,e^{-ip_00^+}\mathcal{G}_{22}(p_0,\boldsymbol{p}), \tag{3.59}$$

where the fermion propagator up to the order ϵ is given by

$$\mathcal{G}(p) = G(p) + G(p)\left[\Sigma(p) - \mu\sigma_3\right] G(p) + O(\epsilon^2). \tag{3.60}$$

With the use of the definition of the bare fermion propagator $G(p)$ in Eq. (3.7) and the one-loop fermion self-energy $\Sigma(p)$ in Eq. (3.46), the diagonal elements of the fermion propagator becomes

$$\begin{aligned}\mathcal{G}_{11}(p) &= G_{11}(p) + G_{11}(p)\left[\Sigma_{11}(p) - \mu\right] G_{11}(p) + G_{12}(p)\left[\Sigma_{22}(p) + \mu\right] G_{21}(p) \\ &= \frac{p_0 + \varepsilon_{\boldsymbol{p}}}{p_0^2 - E_{\boldsymbol{p}}^2 + i\delta} + \left(\frac{p_0 + \varepsilon_{\boldsymbol{p}}}{p_0^2 - E_{\boldsymbol{p}}^2 + i\delta}\right)^2 \left[\Sigma_{11}(p) - \mu\right] + \left(\frac{\phi_0}{p_0^2 - E_{\boldsymbol{p}}^2 + i\delta}\right)^2 \left[\Sigma_{22}(p) + \mu\right]\end{aligned} \tag{3.61}$$

and $\mathcal{G}_{22}(p_0, \boldsymbol{p}) = -\mathcal{G}_{11}(-p_0, \boldsymbol{p})$. Since we are considering a symmetric case with $\mu_\uparrow = \mu_\downarrow$ and $m_\uparrow = m_\downarrow$, we can confirm the relationship $n_{\boldsymbol{p}} = n_{\boldsymbol{p}\uparrow} = n_{\boldsymbol{p}\downarrow}$.

From the first term in Eq. (3.61), the $O(1)$ part of the momentum distribution function $n_{\boldsymbol{p}}^{(0)}$ is easily obtained as

$$n_{\boldsymbol{p}}^{(0)} = \int \frac{dp_0}{2\pi i}\, e^{ip_0 0^+} \frac{p_0 + \varepsilon_{\boldsymbol{p}}}{p_0^2 - E_{\boldsymbol{p}}^2 + i\delta} = \frac{E_{\boldsymbol{p}} - \varepsilon_{\boldsymbol{p}}}{2E_{\boldsymbol{p}}}. \tag{3.62}$$

The last two terms in Eq. (3.61) contribute to the momentum distribution function to the order of ϵ. Since $\Sigma_{11}(p_0, \boldsymbol{p})$ in Eq. (3.47) is analytic at $\mathrm{Im}[p_0] > 0$, the p_0 integral of the second term can be evaluated as

$$\begin{aligned}\int \frac{dp_0}{2\pi i} \left(\frac{p_0 + \varepsilon_{\boldsymbol{p}}}{p_0^2 - E_{\boldsymbol{p}}^2 + i\delta}\right)^2 \left[\Sigma_{11}(p) - \mu\right] &= \frac{\partial}{\partial p_0}\left[\left(\frac{p_0 + \varepsilon_{\boldsymbol{p}}}{p_0 - E_{\boldsymbol{p}}}\right)^2 \left[\Sigma_{11}(p) - \mu\right]\right]\Bigg|_{p_0 = -E_{\boldsymbol{p}}} \\ &= -\frac{\phi_0^2}{4E_{\boldsymbol{p}}^3}\left[\Sigma_{11}(-E_{\boldsymbol{p}}, \boldsymbol{p}) - \mu\right] + \frac{(E_p - \varepsilon_{\boldsymbol{p}})^2}{4E_{\boldsymbol{p}}^2}\Sigma_{11}'(-E_{\boldsymbol{p}}, \boldsymbol{p}).\end{aligned} \tag{3.63}$$

The prime in $\Sigma_{11}'(p_0, \boldsymbol{p})$ represents the derivative with respect to p_0. Similarly, using the relationship $\Sigma_{22}(p_0, \boldsymbol{p}) = -\Sigma_{11}(-p_0, \boldsymbol{p})$, the p_0 integral of the third term in Eq. (3.61) can be evaluated as

$$\begin{aligned}\int \frac{dp_0}{2\pi i} \left(\frac{\phi_0}{p_0^2 - E_{\boldsymbol{p}}^2 + i\delta}\right)^2 \left[\Sigma_{22}(p) + \mu\right] &= -\int \frac{dp_0}{2\pi i} \left(\frac{\phi_0}{p_0^2 - E_{\boldsymbol{p}}^2 + i\delta}\right)^2 \left[\Sigma_{11}(p) - \mu\right] \\ &= -\frac{\partial}{\partial p_0}\left[\left(\frac{\phi_0}{p_0 - E_{\boldsymbol{p}}}\right)^2 \left[\Sigma_{11}(p) - \mu\right]\right]\Bigg|_{p_0 = -E_{\boldsymbol{p}}} \\ &= -\frac{\phi_0^2}{4E_{\boldsymbol{p}}^3}\left[\Sigma_{11}(-E_{\boldsymbol{p}}, \boldsymbol{p}) - \mu\right] - \frac{\phi_0^2}{4E_{\boldsymbol{p}}^2}\Sigma_{11}'(-E_{\boldsymbol{p}}, \boldsymbol{p}).\end{aligned} \tag{3.64}$$

From these two contributions, we obtain the next-to-leading order correction to the momentum distribution function as

$$n_{\boldsymbol{p}}^{(1)} = \frac{\phi_0^2}{2E_{\boldsymbol{p}}^3}\mu - \frac{\phi_0^2}{2E_{\boldsymbol{p}}^3}\Sigma_{11}(-E_{\boldsymbol{p}}, \boldsymbol{p}) - \frac{\varepsilon_{\boldsymbol{p}}(E_{\boldsymbol{p}} - \varepsilon_{\boldsymbol{p}})}{2E_{\boldsymbol{p}}^2}\Sigma_{11}'(-E_{\boldsymbol{p}}, \boldsymbol{p}). \tag{3.65}$$

Substituting the solution of the gap equation in the unitarity limit $\mu = \epsilon\phi_0/2 + O(\epsilon^2)$ and the expression for $\Sigma_{11}(p)$ in Eq. (3.47), the $O(\epsilon)$ part of the momentum distribution function $n_{\boldsymbol{p}}^{(1)}$ is given by

$$n_{\boldsymbol{p}}^{(1)} = \epsilon\frac{\phi_0^3}{4E_{\boldsymbol{p}}^3} + \frac{g^2}{4}\int \frac{d\boldsymbol{k}}{(2\pi)^4} \frac{(E_{\boldsymbol{k}} - \varepsilon_{\boldsymbol{k}})}{E_{\boldsymbol{p}}E_{\boldsymbol{k}}(E_{\boldsymbol{p}} + E_{\boldsymbol{k}} + \varepsilon_{\boldsymbol{k}-\boldsymbol{p}}/2)}\left[\frac{\phi_0^2}{E_{\boldsymbol{p}}^2} + \frac{\varepsilon_{\boldsymbol{p}}(E_{\boldsymbol{p}} - \varepsilon_{\boldsymbol{p}})}{E_{\boldsymbol{p}}(E_{\boldsymbol{k}} + \varepsilon_{\boldsymbol{k}-\boldsymbol{p}}/2 + E_{\boldsymbol{p}})}\right]. \tag{3.66}$$

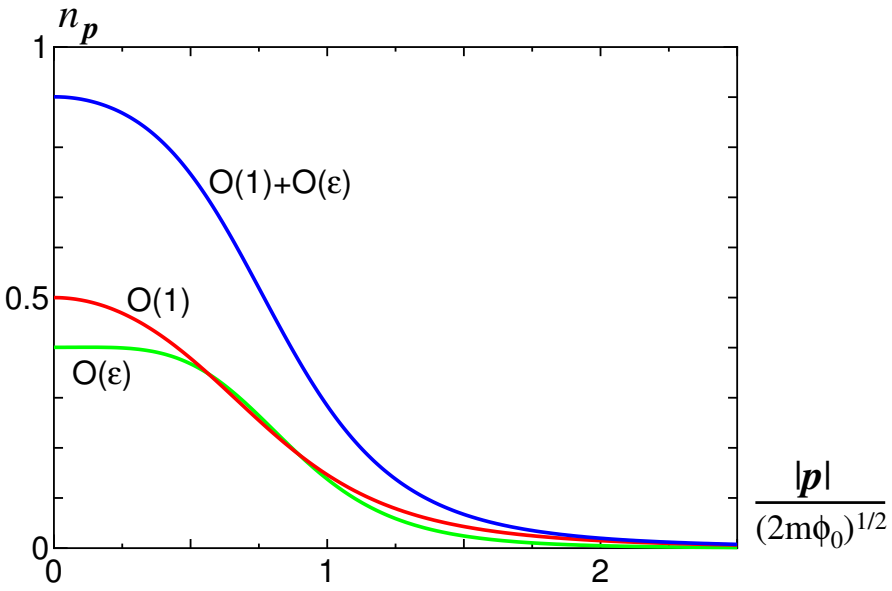

Figure 3.6: Momentum distribution function $n_{\boldsymbol{p}}$ of the fermion quasiparticles in the unitarity limit as a function of the momentum $|\boldsymbol{p}|/\sqrt{2m\phi_0}$ to the leading and next-to-leading orders in ϵ. The $O(1)$ part $n_{\boldsymbol{p}}^{(0)}$ (red curve), the $O(\epsilon)$ part $n_{\boldsymbol{p}}^{(1)}$ (green curve), and their sum $n_{\boldsymbol{p}} = n_{\boldsymbol{p}}^{(0)} + n_{\boldsymbol{p}}^{(1)}$ (blue curve) at $\epsilon \to 1$ are respectively shown.

The momentum distribution function of the fermion quasiparticles $n_{\boldsymbol{p}} = n_{\boldsymbol{p}}^{(0)} + n_{\boldsymbol{p}}^{(1)}$ to the leading and next-to-leading orders in ϵ is plotted as a function of the momentum $|\boldsymbol{p}|/\sqrt{2m\phi_0}$ in Fig. 3.6. Since the condensate ϕ_0 is related to the Fermi energy $\varepsilon_{\rm F} = k_{\rm F}^2/2m$ by Eq. (3.41),

$$\varepsilon_{\rm F} = \frac{\phi_0}{\epsilon^{2/d}}\left(1 - \frac{1-\ln 2}{4}\epsilon\right), \tag{3.67}$$

the Fermi momentum in the horizontal axis of Fig. 3.6 corresponds to

$$\frac{k_{\rm F}}{\sqrt{2m\phi_0}} = \epsilon^{-1/d}\left(1 - \frac{1-\ln 2}{8}\epsilon\right) \approx 0.962 \qquad (\epsilon \to 1). \tag{3.68}$$

We can find overall agreement of the momentum distribution function computed by the ϵ expansion up to the next-to-leading order in ϵ with that from the Monte Carlo simulation [116].

3.8 Condensate fraction

The fermion density in the condensation N_0 is related with the off-diagonal element of the fermion propagator $\mathcal{G}_{12}(p)$ through [116, 117, 118, 119]

$$N_0 = 2\int \frac{d\boldsymbol{p}}{(2\pi)^d}\left[\int \frac{dp_0}{2\pi i}\,\mathcal{G}_{12}(p_0, \boldsymbol{p})\right]^2. \tag{3.69}$$

Since $\mathcal{G}_{12}(p)$ up to the order ϵ is given from Eq. (3.60) as

$$\begin{aligned}\mathcal{G}_{12}(p) &= G_{12}(p) + G_{11}(p)\left[\Sigma_{11}(p)-\mu\right]G_{12}(p) + G_{12}(p)\left[\Sigma_{22}(p)+\mu\right]G_{22}(p)\\ &= -\frac{\phi_0}{p_0^2 - E_{\boldsymbol{p}}^2 + i\delta} - \frac{\phi_0\left(p_0+\varepsilon_{\boldsymbol{p}}\right)}{\left(p_0^2 - E_{\boldsymbol{p}}^2 + i\delta\right)^2}\left[\Sigma_{11}(p)-\mu\right] - \frac{\phi_0\left(p_0-\varepsilon_{\boldsymbol{p}}\right)}{\left(p_0^2 - E_{\boldsymbol{p}}^2 + i\delta\right)^2}\left[\Sigma_{22}(p)+\mu\right],\end{aligned} \tag{3.70}$$

the p_0 integration of each terms results in

$$-\int\frac{dp_0}{2\pi i}\,\frac{\phi_0}{p_0^2 - E_{\boldsymbol{p}}^2 + i\delta} = \frac{\phi_0}{2E_{\boldsymbol{p}}} \tag{3.71}$$

and

$$\begin{aligned}-\int\frac{dp_0}{2\pi i}\,\frac{\phi_0\left(p_0+\varepsilon_{\boldsymbol{p}}\right)}{\left(p_0^2 - E_{\boldsymbol{p}}^2 + i\delta\right)^2}\left[\Sigma_{11}(p)-\mu\right] &= -\int\frac{dp_0}{2\pi i}\,\frac{\phi_0\left(p_0-\varepsilon_{\boldsymbol{p}}\right)}{\left(p_0^2 - E_{\boldsymbol{p}}^2 + i\delta\right)^2}\left[\Sigma_{22}(p)+\mu\right]\\ &= -\phi_0\frac{\partial}{\partial p_0}\left[\frac{p_0+\varepsilon_{\boldsymbol{p}}}{\left(p_0-E_{\boldsymbol{p}}\right)^2}\left[\Sigma_{11}(p)-\mu\right]\right]\Bigg|_{p_0=-E_{\boldsymbol{p}}}\\ &= -\phi_0\frac{\varepsilon_{\boldsymbol{p}}}{4E_{\boldsymbol{p}}^3}\left[\Sigma_{11}(-E_{\boldsymbol{p}},\boldsymbol{p})-\mu\right] + \phi_0\frac{E_p-\varepsilon_{\boldsymbol{p}}}{4E_{\boldsymbol{p}}^2}\Sigma'_{11}(-E_{\boldsymbol{p}},\boldsymbol{p}).\end{aligned} \tag{3.72}$$

Here we used the relationship $\Sigma_{22}(p_0,\boldsymbol{p}) = -\Sigma_{11}(-p_0,\boldsymbol{p})$ and the fact that $\Sigma_{11}(p_0,\boldsymbol{p})$ in Eq. (3.47) is analytic at $\mathrm{Im}[p_0] > 0$.

Therefore, the fermion density in the condensation N_0 up to the order ϵ is given by

$$N_0 = \phi_0^2\int\frac{d\boldsymbol{p}}{(2\pi)^d}\left[\frac{1}{2E_{\boldsymbol{p}}^2} + \frac{\varepsilon_{\boldsymbol{p}}}{E_{\boldsymbol{p}}^4}\mu - \frac{\varepsilon_{\boldsymbol{p}}}{E_{\boldsymbol{p}}^4}\Sigma_{11}(-E_{\boldsymbol{p}},\boldsymbol{p}) + \frac{E_p-\varepsilon_{\boldsymbol{p}}}{E_{\boldsymbol{p}}^3}\Sigma'_{11}(-E_{\boldsymbol{p}},\boldsymbol{p})\right]. \tag{3.73}$$

The first term provides the leading contribution to N_0, while the other three terms are $O(\epsilon)$ corrections. Substituting the solution of the gap equation in the unitarity limit $\mu = \epsilon\phi_0/2 + O(\epsilon^2)$ and performing the integration over $\boldsymbol{p}$, we obtain N_0 as

$$N_0 = \left[\frac{\Gamma\left(1-\frac{\epsilon}{4}\right)\Gamma\left(\frac{\epsilon}{4}\right)}{4\Gamma\left(2-\frac{\epsilon}{2}\right)} + \frac{\pi}{8}\epsilon + 0.127741\,\epsilon + O(\epsilon^2)\right]\left(\frac{m\phi_0}{2\pi}\right)^{\frac{d}{2}}. \tag{3.74}$$

Note that because the $\boldsymbol{p}$ integration of the leading term is logarithmically divergent at $d = 4$, the leading contribution to N_0 becomes $O(1/\epsilon)$ at $d = 4-\epsilon$. The fermion density in the condensation should be compared to the total fermion density N to the same order in ϵ [102]:

$$N = \left[\frac{\Gamma\left(\frac{3}{2}-\frac{\epsilon}{4}\right)\Gamma\left(1+\frac{\epsilon}{4}\right)}{2\sqrt{\pi}\,\Gamma\left(2-\frac{\epsilon}{2}\right)} + \frac{1}{2}\epsilon + 0.258352\,\epsilon + O(\epsilon^2)\right]\left(\frac{m\phi_0}{2\pi}\right)^{\frac{d}{2}}. \tag{3.75}$$

Taking the ratio of N_0 to N, we find the condensate fraction N_0/N to be

$$\frac{N_0}{N} = 1 - 0.0966\,\epsilon - 0.2423\,\epsilon^2 + O(\epsilon^3). \tag{3.76}$$

The condensate fraction can take a value from zero (BCS limit) to one (BEC limit). The lowest term in the ϵ expansion is one as in the BEC limit and thus all fermion are in the condensation at four spatial dimensions. Below $d = 4$, the condensate fraction decreases and the naive extrapolation to $\epsilon = 1$ gives $N_0/N \approx 0.661$.

	$\xi = \mu/\varepsilon_{\rm F}$	Δ/μ	N_0/N
mean-field approximation	0.5906	1.1622	0.6994 [118]
ϵ expansion (NLO)	0.475	1.31	0.661
$1/N$ expansion (NLO) [104]	0.279	1.50	—
self-consistent approach [78]	0.360	—	—
Monte Carlo simulation	0.42 [86]	1.2 [86]	0.58 [116]

Table 3.2: Comparison of the results by the ϵ expansion with other analytic and numerical calculations in the unitarity limit.

3.9 Extrapolation to $\epsilon = 1$

Finally, we discuss the extrapolation of the series expansion to the physical case at three spatial dimensions. Although the formalism is based on the smallness of ϵ, we see that the corrections are reasonably small even at $\epsilon = 1$. If we naively use only the leading and next-to-leading order results for ξ in Eq.(3.43), Δ in Eq.(3.56), ε_0 in Eq.(3.57), and N_0/N in Eq. (3.76) in the unitarity limit, their extrapolations to $\epsilon = 1$ give for three spatial dimensions

$$\xi \approx 0.475, \qquad \frac{\Delta}{\mu} \approx 1.31, \qquad \frac{\varepsilon_0}{\mu} \approx 2, \qquad \frac{N_0}{N} \approx 0.661. \tag{3.77}$$

They are reasonably close to the results of recent Monte Carlo simulations, which yield $\xi \approx 0.42$, $\Delta/\mu \approx 1.2$, $\varepsilon_0/\mu \approx 1.9$ [86], and $N_0/N \approx 0.58$ [116]. They are also consistent with recent experimental measurements of ξ, where $\xi = 0.51 \pm 0.04$ [39] and $\xi = 0.46 \pm 0.05$ [43]. These agreements can be taken as a strong indication that the ϵ expansion is useful even at $\epsilon = 1$. In Table 3.2, we show results on ξ, $\Delta/\varepsilon_{\rm F}$, and N_0/N from other analytic and numerical calculations. The self-consistent approach [78] quoted in Table 3.2 and Table 9.1 is based on the Luttinger–Ward and DeDominicis–Martin formalism [120, 121] where the potential functional is self-consistently approximated by ladder diagrams [122, 123]. We can see some improvement of our results compared to naive mean-field approximations and other analytic approaches.

Our ϵ expansion predicts the behavior of the thermodynamic quantities near the unitarity limit. From Eqs. (3.44), (3.45), and (3.42), the extrapolations to the three spatial dimensions $\epsilon = 1$ lead to

$$\frac{P}{\varepsilon_{\rm F} N} \approx \frac{2}{d+2}\xi - \frac{1}{8}\frac{\varepsilon_{\rm b}}{\varepsilon_{\rm F}}, \tag{3.78}$$

$$\frac{E}{\varepsilon_{\rm F} N} \approx \frac{d}{d+2}\xi - \frac{1}{4}\frac{\varepsilon_{\rm b}}{\varepsilon_{\rm F}}\left(\frac{5}{2} - \ln\frac{\varepsilon_{\rm b}}{\varepsilon_{\rm F}}\right), \tag{3.79}$$

$$\frac{\mu}{\varepsilon_{\rm F}} \approx \xi - \frac{1}{4}\frac{\varepsilon_{\rm b}}{\varepsilon_{\rm F}}\left(3 - \ln\frac{\varepsilon_{\rm b}}{\varepsilon_{\rm F}}\right). \tag{3.80}$$

The pressure, energy density, and chemical potential at fixed density are decreasing function of the

binding energy ε_b with the slope shown above. In Chap. 7, we will make a discussion to improve the extrapolation of the series expansion by imposing the exact result at $d = 2$ as a boundary condition.

We can also try to determine the location of the splitting point. At this point,

$$\frac{\varepsilon_b}{\varepsilon_F} = \frac{2}{\epsilon^{2/d-1}}[1 + O(\epsilon)] \to 2 \qquad \text{at } d = 3 \tag{3.81}$$

and comparing with Eq. (2.14), one finds that at the splitting point $ak_F \approx 1$. Since this result is known only to leading order in ϵ, one must be cautious with the numerical value. However, certain qualitative features are probably correct: the splitting point is located on the BEC side of the unitarity limit ($a > 0$) and that the chemical potential $\mu/\varepsilon_F \approx -0.5$ is negative at this point.

Chapter 4

Phase structure of polarized Fermi gas

4.1 Background and proposed phase diagram

Here we apply the ϵ expansion developed in the previous Chapter to the unitary Fermi gas with unequal densities of two components (polarization). We put special emphasis on investigating the phase structure of the polarized Fermi gas in the unitary regime, which has a direct relation with the recent measurements in atomic traps [42, 43, 44, 45, 46]. Furthermore, it may be possible in future to realize the Feshbach resonances between two different species of fermionic atoms to study a Fermi gas with finite mass difference between different fermion species. Such asymmetric systems of fermions with density and mass imbalances will be also interesting as a prototype of high density quark matter in the core of neutron stars, where the density and mass asymmetries exist among different quark flavors [62, 63, 64, 65, 66]. Extension of the ϵ expansion to the polarized Fermi gas with unequal masses will be studied in the next Chapter and we concentrate on the equal mass case here.

Reliable facts on the phase structure of the polarized Fermi gas is known only in the weak-coupling BCS and BEC limits. If the polarization chemical potential $H = (\mu_\uparrow - \mu_\downarrow)/2$ is sufficiently small, the ground state is the unpolarized superfluid state both in the BCS and BEC limits and these two limits are considered to be smoothly connected as a function of $1/ak_{\rm F}$ (phase I in Fig. 4.1). When H is increased, we will have different situations in the two limits. In the BCS limit, the BCS superfluid state becomes unstable toward to the Fulde-Ferrell-Larkin-Ovchinikov (FFLO) states where Cooper pairs form with a nonzero momentum and the superfluid order parameter varies in space [124, 125] (phase IV). For the sufficiently large H, the Cooper paring is unfavorable and the system goes to a polarized normal Fermi gas (phase II). On the other hand, when H is increased in the BEC limit, unbound fermions are created on the top of the molecular BEC ground state. The system becomes a homogeneous mixture of the polarized fermions with the condensed molecules (phase III). For the sufficiently large H, all bound molecules disappear and the ground state is a fully polarized normal Fermi gas (phase II). Since the FFLO phase where the rotational symmetry is spontaneously broken does not appear in the BEC limit, such a phase should terminates somewhere between the BCS and BEC limits.

From these knowledge in the two limits and assuming there is a phase transition line between

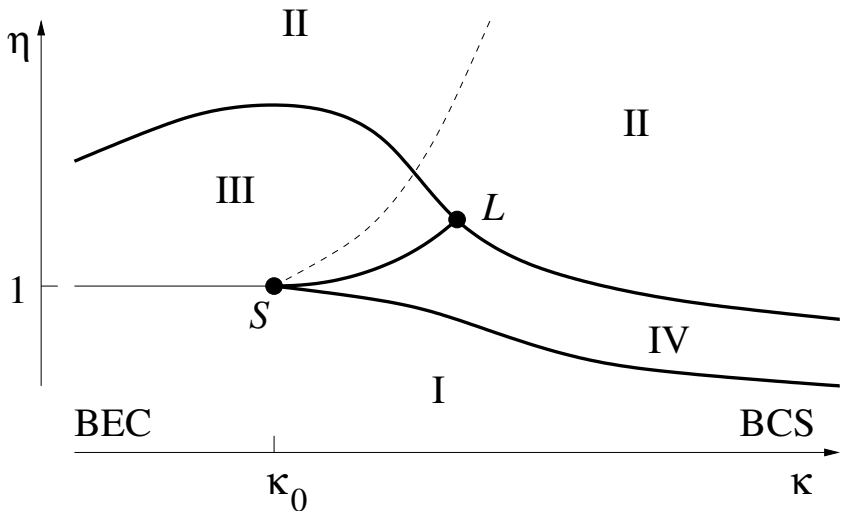

Figure 4.1: Proposed phase diagram in the plane of the diluteness parameter $\kappa = -1/ak_{\rm F}$ and the polarization chemical potential $\eta = H/\Delta_{H=0}$ by Son and Stephanov [112]. I is the unpolarized BEC/BCS phase, II is the normal phase, III is the gapless superfluid phase, and IV is a region of Fulde-Ferrell-Larkin-Ovchinikov phases [124, 125]. The dashed line divides phases II and III into regions with one (on the left) and two (on the right) Fermi surfaces. Region IV must be divided into phases with different patterns of breaking of the rotational symmetry (not shown).

the phases III and IV instead of I and II, Son and Stephanov proposed a global phase diagram of the polarized Fermi gas in the BCS-BEC crossover as shown in Fig. 4.1 [112]. The point S where the FFLO phase terminates is called the *splitting point* and the phase structure around it is studied based on the effective field theory [112]. The purpose of this Chapter is to study the phase structure of the polarized Fermi gas in the unitary regime including the splitting point from the microscopic point of view using the ϵ expansion.

4.2 Effective potential at finite superfluid velocity

In order to take into account the possibility of the FFLO state in the phase diagram, we generalize our formalism to allow a spatially varying condensate where $\langle\phi(x)\rangle = e^{2im\boldsymbol{v}_{\rm s}\cdot\boldsymbol{x}}\phi_0$ with $\boldsymbol{v}_{\rm s}$ being the superfluid velocity. The factor $e^{2im\boldsymbol{v}_{\rm s}\cdot\boldsymbol{x}}$ in front of ϕ_0 in the Lagrangian density can be absorbed by making the Galilean transformation on the fermion field as $\psi_\sigma(x) \to e^{im\boldsymbol{v}_{\rm s}\cdot\boldsymbol{x}}\psi_\sigma(x)$ and the boson field as $\varphi(x) \to e^{2im\boldsymbol{v}_{\rm s}\cdot\boldsymbol{x}}\varphi(x)$. Accordingly, the fermion propagator in Eq. (3.7) is modified as

$$G(p_0,\boldsymbol{p}) = \frac{1}{(p_0+H-\boldsymbol{p}\cdot\boldsymbol{v}_{\rm s})^2-(\varepsilon_{\boldsymbol{p}}+\varepsilon_{m\boldsymbol{v}_{\rm s}})^2-\phi_0^2+i\delta} \times\begin{pmatrix} p_0+H+\varepsilon_{\boldsymbol{p}-m\boldsymbol{v}_{\rm s}} & -\phi_0 \\ -\phi_0 & p_0+H-\varepsilon_{\boldsymbol{p}+m\boldsymbol{v}_{\rm s}}\end{pmatrix}, \tag{4.1}$$

while the boson propagator in Eq. (3.8) as

$$D(p_0, \boldsymbol{p}) = \left(p_0 - \frac{\varepsilon_{\boldsymbol{p}+2m\boldsymbol{v}_\mathrm{s}}}{2} + i\delta \right)^{-1} . \tag{4.2}$$

The value of the superfluid velocity $\boldsymbol{v}_\mathrm{s}$ is determined from minimizing the $\boldsymbol{v}_\mathrm{s}$ dependent part of the effective potential $V_H(\boldsymbol{v}_\mathrm{s})$. As far as the polarization H is sufficiently small compared to the energy gap Δ of the fermion quasiparticle, $V_H(\boldsymbol{v}_\mathrm{s})$ to the leading order in ϵ is given by the fermion one-loop diagram with the propagator in Eq.(4.1):

$$V_{H<\Delta}(\boldsymbol{v}_\mathrm{s}) = -\int \frac{d\boldsymbol{p}}{(2\pi)^d} \sqrt{\left(\varepsilon_{\boldsymbol{p}} + \varepsilon_{m\boldsymbol{v}_\mathrm{s}}\right)^2 + \phi_0^2}. \tag{4.3}$$

Since it will turn out that $\varepsilon_{m\boldsymbol{v}_\mathrm{s}}$ is $O(\epsilon^{11})$, we can expand the integrand in terms of $\varepsilon_{m\boldsymbol{v}_\mathrm{s}}/\phi_0$ to lead to

$$V_{H<\Delta}(\boldsymbol{v}_\mathrm{s}) = -\int \frac{d\boldsymbol{p}}{(2\pi)^d} \frac{\varepsilon_\mathrm{b}}{E_{\boldsymbol{p}}} \varepsilon_{m\boldsymbol{v}_\mathrm{s}} \simeq \frac{\varepsilon_{m\boldsymbol{v}_\mathrm{s}}}{\epsilon} \left(\frac{m\phi_0}{2\pi} \right)^2 . \tag{4.4}$$

Using the definition of the fermion number density N in Eq. (3.40), this part can be rewritten as $V_{H<\Delta}(\boldsymbol{v}_\mathrm{s}) = N\varepsilon_{m\boldsymbol{v}_\mathrm{s}}$, which represents the energy cost due to the presence of the superfluid flow.

If $H - \boldsymbol{p}\cdot\boldsymbol{v}_\mathrm{s}$ reaches the bottom of the fermion quasiparticle spectrum $\Delta + (\varepsilon_{\boldsymbol{p}} + \varepsilon_{m\boldsymbol{v}_\mathrm{s}} - \varepsilon_0)^2/2\phi_0$, $V_H(\boldsymbol{v}_\mathrm{s})$ receives an additional contribution from the filled fermion quasiparticles. Since $\varepsilon_{m\boldsymbol{v}_\mathrm{s}} \sim \epsilon^{11}$ is small, we can neglect it in the quasiparticle energy. Then the $\boldsymbol{v}_\mathrm{s}$ dependent part of the effective potential is given by

$$V_H(\boldsymbol{v}_\mathrm{s}) = N\varepsilon_{m\boldsymbol{v}_\mathrm{s}} - \int \frac{d\boldsymbol{p}}{(2\pi)^d} \left(H - \boldsymbol{p}\cdot\boldsymbol{v}_\mathrm{s} - \omega_\mathrm{F}(\boldsymbol{p}) \right)_> , \tag{4.5}$$

where we have introduced a notation $(x)_>^y = x^y\,\theta(x)$ and $\omega_\mathrm{F}(\boldsymbol{p})$ is the fermion quasiparticle spectrum $\omega_\mathrm{F}(\boldsymbol{p}) = \Delta + (\varepsilon_{\boldsymbol{p}} - \varepsilon_0)^2/2\phi_0$ derived in Eq. (3.53). The effective potential $V_H(\boldsymbol{v}_\mathrm{s})$ to the leading order in ϵ has the same form as that studied based on the effective field theory in [112].

4.3 Critical polarizations

Now we evaluate the effective potential $V_H(\boldsymbol{v}_\mathrm{s})$ at $d = 4$ as a function of $\boldsymbol{v}_\mathrm{s}$ and H. Changing the integration variables to $z = \varepsilon_{\boldsymbol{p}}/\phi_0$ and $w = \hat{\boldsymbol{p}}\cdot\hat{\boldsymbol{v}}_\mathrm{s}$, we have

$$\begin{aligned} V_H(\boldsymbol{v}_\mathrm{s}) = &\left(\frac{m\phi_0}{2\pi} \right)^2 \\ &\times \left[\frac{\varepsilon_{m\boldsymbol{v}_\mathrm{s}}}{\epsilon} - \frac{2}{\pi} \int_0^\infty dz \int_{-1}^1 dw\, z\sqrt{1-w^2} \left(H - \Delta - \frac{(z-z_0)^2}{2}\phi_0 - 2\sqrt{z\phi_0\varepsilon_{m\boldsymbol{v}_\mathrm{s}}}\, w \right)_> \right], \end{aligned} \tag{4.6}$$

where $z_0 = \varepsilon_0/\phi_0 \sim \epsilon$. We can approximate $\sqrt{z\phi_0\varepsilon_{m\boldsymbol{v}_\mathrm{s}}}$ by $\sqrt{z_0\phi_0\varepsilon_{m\boldsymbol{v}_\mathrm{s}}}$ because the difference will be $O(\epsilon^8)$ and negligible compared to itself $\sqrt{z_0\phi_0\varepsilon_{m\boldsymbol{v}_\mathrm{s}}} \sim \epsilon^6$. Then the integration over z leads to

$$V_H(\boldsymbol{v}_\mathrm{s}) = \left(\frac{m\phi_0}{2\pi} \right)^2 \phi_0 \left[\frac{\varepsilon_{m\boldsymbol{v}_\mathrm{s}}}{\epsilon\phi_0} - \frac{32}{3\pi} z_0 \left(\frac{\varepsilon_{m\boldsymbol{v}_\mathrm{s}}}{\phi_0} z_0 \right)^{3/4} \int_{-1}^1 dw\, \sqrt{1-w^2} \left(\frac{H-\Delta}{2\sqrt{\varepsilon_{m\boldsymbol{v}_\mathrm{s}}\phi_0 z_0}} - w \right)_>^{3/2} \right]. \tag{4.7}$$

By introducing the dimensionless variables x and h as

$$\frac{\varepsilon_{m\boldsymbol{v}_\mathrm{s}}}{\phi_0} = x^2\left(\frac{32}{3\pi}\epsilon\right)^4 z_0^7 \qquad \text{and} \qquad \frac{H-\Delta}{\phi_0} = 2h\left(\frac{32}{3\pi}\epsilon\right)^2 z_0^4, \tag{4.8}$$

we can rewrite the effective potential $V_H(\boldsymbol{v}_\mathrm{s}) = V_h(x)$ in the simple form as

$$V_h(x) = \phi_0\left(\frac{m\phi_0}{2\pi}\right)^2\left(\frac{32}{3\pi}\right)^4 \epsilon^3 z_0^7\left[x^2 - x^{3/2}\int_{-1}^{1} dw\ \sqrt{1-w^2}\left(\frac{h}{x}-w\right)_>^{3/2}\right]. \tag{4.9}$$

Now we see that if the superfluid velocity exists, $\varepsilon_{m\boldsymbol{v}_\mathrm{s}} \sim \epsilon^{11}$ and the $\boldsymbol{v}_\mathrm{s}$ dependent part of the effective potential is $O(\epsilon^{10})$.

Numerical studies on the effective potential $V_h(x)$ as a function of x show that there exists a region of h, $h_1 < h < h_2$, where $V_h(x)$ has its minimum at finite x. These two critical values are numerically given by

$$h_1 = -0.00366 \qquad \text{and} \qquad h_2 = 0.0275. \tag{4.10}$$

Correspondingly, we obtain the critical polarizations normalized by the energy gap as

$$\frac{H_1}{\Delta} = 1 - 0.0843\,\epsilon^2\left(\frac{\varepsilon_0}{\Delta}\right)^4, \tag{4.11}$$

and

$$\frac{H_2}{\Delta} = 1 + 0.634\,\epsilon^2\left(\frac{\varepsilon_0}{\Delta}\right)^4. \tag{4.12}$$

Here we have replaced ϕ_0 by Δ because they only differ by $O(\epsilon)$ [Eq. (3.54)]. The region for the phase with spatially varying condensate is $H_2 - H_1 \sim \epsilon^6$, where the superfluid velocity $\boldsymbol{v}_\mathrm{s}$ is finite at the ground state.

As the polarization increases further $H > H_2$, the superfluid velocity disappears. If $H < \omega_\mathrm{F}(\boldsymbol{0})$, fermion quasiparticles which have momentum $\omega_\mathrm{F}(\boldsymbol{p}) < H$ are filled and hence there exist two Fermi surfaces, while there is only one Fermi surface for $H > \omega_\mathrm{F}(\boldsymbol{0})$ [see Fig. 3.5]. Therefore, from the quasiparticle spectrum derived in Eq. (3.53), the polarization for the disappearance of the inner Fermi surface H_3 is given by

$$\frac{H_3}{\Delta} = \frac{\omega_\mathrm{F}(\boldsymbol{0})}{\Delta} = 1 + \frac{1}{2}\left(\frac{\varepsilon_0}{\Delta}\right)^2. \tag{4.13}$$

Here the location of minimum in the fermion quasiparticle spectrum ε_0 is related with the binding energy ε_b near the unitarity limit via $\varepsilon_0 = \epsilon\Delta - \varepsilon_\mathrm{b}/2$ [Eq. (3.58)]. The critical polarizations H_1/Δ and H_2/Δ as functions of $\varepsilon_\mathrm{b}/\epsilon\Delta$ are illustrated in Fig. 4.2.

4.4 Phase transition to normal Fermi gas

Next we turn to the phase transition to the normal Fermi gas which occurs at $H - \Delta \sim \epsilon$. Since the region for the phase with spatially varying condensate is $H_{1,2} - \Delta \sim \epsilon^6$, we can neglect the superfluid

velocity $\boldsymbol{v}_{\rm s}$ here. We can also neglect the possibility to have two Fermi surfaces where $H_3 - \Delta \sim \epsilon^2$. Then the contribution of the polarized quasiparticles to the effective potential is evaluated as

$$\begin{aligned} V_H(\mathbf{0}) &= -\int \frac{d\boldsymbol{p}}{(2\pi)^d} \left(H - \omega_{\rm F}(\boldsymbol{p})\right)_> \\ &\simeq -\frac{(H-\Delta)_>^2}{2\phi_0} \left(\frac{m\phi_0}{2\pi}\right)^{d/2}, \end{aligned} \tag{4.14}$$

where we have neglected the higher order corrections due to the shift of the location of minimum in the dispersion relation $\varepsilon_0 \sim \epsilon$. According to the modification of the effective potential in Eq. (3.36) to $V_{\rm eff}(\phi_0) + V_H$, the solution of the gap equation in Eq. (3.38) becomes $\phi_0 \to \phi_0 + \phi_H$, where

$$\phi_H = -(H-\Delta)_> + \frac{(H-\Delta)_>^2}{2\phi_0}. \tag{4.15}$$

Then the pressure of polarized Fermi gas in the superfluid state is given by $P = -V_{\rm eff}(\phi_0 + \phi_H) - V_H$, which results in

$$P = \frac{\phi_0}{6}\left[1 + \left(\frac{17}{12} - 3C - \frac{\gamma + \ln 2}{2}\right)\epsilon - \frac{3\varepsilon_{\rm b}}{4\phi_0}\right]\left(\frac{m\phi_0}{2\pi}\right)^{d/2} + O\left(\epsilon(H-\Delta)_>^2, (H-\Delta)_>^3\right). \tag{4.16}$$

The polarization dependent part of the pressure $P_H \sim \epsilon^3$ is small and negligible in the region considered here $H - \Delta \sim \epsilon$.

The pressure of the superfluid state should be compared to that of the normal state with the same chemical potentials. Since the phase transition to the normal state happens at $H \sim \phi_0 \gg \mu \sim \epsilon\phi_0$, only one-component of fermions exists in the normal state. Therefore, the interaction is completely suppressed in the normal Fermi gas and its pressure $P_{\rm n}$ is simply given by that of a free Fermi gas with a single component:

$$P_{\rm n} = \int \frac{d\boldsymbol{p}}{(2\pi)^d}(\mu_\uparrow - \varepsilon_{\boldsymbol{p}})_> = \frac{(H+\mu)^{\frac{d}{2}+1}}{\Gamma\left(\frac{d}{2}+2\right)}\left(\frac{m}{2\pi}\right)^{\frac{d}{2}}. \tag{4.17}$$

The phase transition of the superfluid state to the normal state occurs at $H = H_{\rm c}$ where the two pressures coincide $P = P_{\rm n}$. From Eqs. (4.16) and (4.17), the critical polarization $H_{\rm c}$ satisfies the following equation,

$$\begin{aligned} H_{\rm c} &= \left[1 + \frac{\varepsilon_{\rm b}}{4\phi_0} - C\epsilon - \frac{2+\ln 2}{6}\epsilon\right]\phi_0 \\ &= \left[1 + \frac{\varepsilon_{\rm b}}{4\Delta} - C\epsilon - \frac{2+\ln 2}{6}\epsilon + (8\ln 3 - 12\ln 2)\epsilon\right]\Delta, \end{aligned} \tag{4.18}$$

where we have substituted the relation between the condensate ϕ_0 and the energy gap Δ at zero polarization in Eq. (3.54). Defining a number $\sigma \sim O(1)$ by

$$\sigma = C + \frac{2+\ln 2}{6} - (8\ln 3 - 12\ln 2) \approx 0.12197. \tag{4.19}$$

the critical polarization normalized by the energy gap at zero polarization is written as

$$\frac{H_c}{\Delta} = 1 - \epsilon\sigma + \frac{\varepsilon_b}{4\Delta} + O(\epsilon^2). \tag{4.20}$$

If the binding energy is large enough $\varepsilon_b/\epsilon\Delta > 4\sigma = 0.488$, the superfluid state remains above $H = \Delta$. The superfluid state at $\Delta < H < H_c$ is referred to as a *gapless* superfluid state. The fermion number densities of two difference components are asymmetric there and the fermionic excitation does not have the energy gap.

In particular, at the unitarity limit where $\varepsilon_b/\Delta = 0$, the critical polarization is given by

$$\left.\frac{H_c}{\Delta}\right|_{UL} = 1 - \epsilon\sigma = 1 - 0.122\,\epsilon, \tag{4.21}$$

At the splitting point where $\varepsilon_b/\Delta = 2\epsilon$, it is

$$\left.\frac{H_c}{\Delta}\right|_{SP} = 1 - \epsilon\sigma + \frac{\epsilon}{2} = 1 + 0.378\,\epsilon. \tag{4.22}$$

The extrapolations to three spatial dimensions $\epsilon = 1$ give the critical polarizations at the two typical points as $H_c/\Delta\,|_{UL} = 0.878$ and $H_c/\Delta\,|_{SP} = 1.378$. At unitarity, hence, there is no gapless superfluid phase. On the other hand, near the splitting point the normal phase is not competitive compared to the gapless phases. The phase boundary between the superfluid and normal phases H_c/Δ as a function of $\varepsilon_b/\epsilon\Delta$ is illustrated in Fig. 4.2.

4.5 Phase structure near the unitarity limit

The schematic phase diagram of the polarized Fermi gas in the unitary regime is shown in Fig. 4.2 in the plane of H and ε_b/ϵ for the fixed energy gap Δ at zero polarization. The critical polarization H_c/Δ divides the phase diagram into two regions; the superfluid phase at $H < H_c$ (I and III) and the normal phase at $H > H_c$ (II). The Fermi gas in the normal phase is fully polarized near the unitarity limit because $H \gg \mu$. The phase transition of the superfluid state to the normal state is of the first order, because of the discontinuity in the fermion number density which is $O(\epsilon^{-1})$ in the superfluid phase while $O(1)$ in the normal phase.

The superfluid phase can be divided further into two regions; the gapped superfluid phase at $H < \Delta$ (I) and the gapless superfluid phase at $\Delta < H < H_c$ (III). At the BEC side of the splitting point (SP) where $\varepsilon_b/\epsilon\Delta > 2$, the phase transition from the gapped phase to the gapless phase is of the second order because a discontinuity appears in the second derivative of the pressure $\partial^2 P/\partial H^2 \sim \epsilon\,\theta(H - \Delta)$ [see Eq. (4.16)]. On the other hand, at the BCS side of the splitting point where

$$4\sigma < \frac{\varepsilon_b}{\epsilon\Delta} < 2, \tag{4.23}$$

there exists the superfluid phase with spatially varying condensate (IV) at $H_1 < H < H_2$ between the gapped and gapless phases. This phase appears only in the narrow region where $H_2 - H_1 \sim \epsilon^6$. The phase transitions at $H = H_1, H_2$ are of the first order.

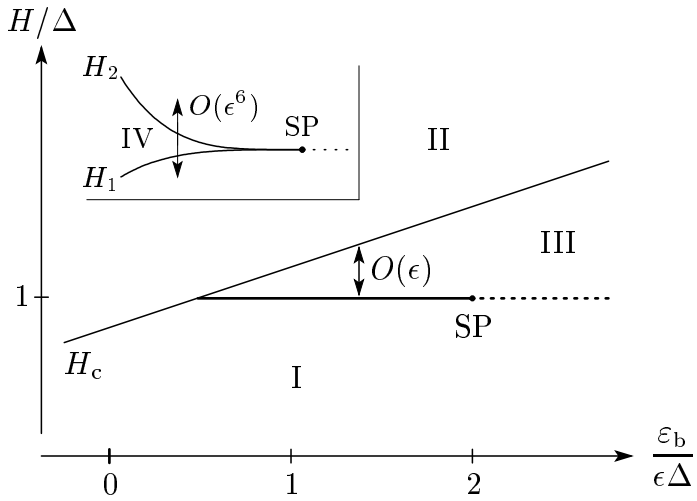

Figure 4.2: Schematic phase diagram of the polarized Fermi gas near the unitarity limit from the ϵ expansion. The phase diagram can be divided into four phases, I: the gapped superfluid phase, II: the polarized normal phase, III: the gapless superfluid phase, and IV: the phase with spatially varying condensate. The inset is the magnification of the region around the splitting point (SP). The phase IV appears in the narrow region represented by the thick line between the phases I and III.

In actual experiments using fermionic atoms, unitary Fermi gases are trapped in the optical potential $V(r)$ [42, 43, 44, 45, 46]. In such cases, the polarization H and the scattering length or ε_b are constant, while the effective chemical potential $\mu - V(r)$ decrease from the center to the peripheral of the trapping potential. For the purpose of comparison of our results with the experiments on the polarized Fermi gases, it is convenient to visualize the phase diagram in the plane of H and μ for the fixed ε_b.

In Fig. 4.3, $\epsilon H_c/\varepsilon_b$ and $\epsilon\Delta/\varepsilon_b$ are plotted as functions of μ/ε_b for the fixed binding energy $\varepsilon_b > 0$. The superfluid phase and the normal phase are separated by the line of the critical polarization $H = H_c$, while the gapped and gapless superfluid phases are separated by the line of the energy gap at zero polarization $H = \Delta$. The intersection of two lines, $H_c = \Delta$, is located at $(\mu/\varepsilon_b, \epsilon H/\varepsilon_b) = ((1 - 4\sigma)/8\sigma, 1/4\sigma) = (0.524, 2.05)$, while the splitting point in the phase diagram is at $(\mu/\varepsilon_b, \epsilon H/\varepsilon_b) = (-1/4, 1/2)$. The horizontal dashed line from right to left tracks the chemical potential μ in the trapped Fermi gas from the center to the peripheral. If the polarization is small enough compared to the binding energy $\epsilon H/\varepsilon_b < 2.05$, there exists the gapless superfluid phase (III) between the gapped superfluid phase (I) and the normal phase (II). When the polarization is above the splitting point $0.5 < \epsilon H/\varepsilon_b < 2.05$, the phase with spatially varying condensate (thick line between I and III) will appear between the gapped and gapless superfluid phases.

Assuming that the picture remains qualitatively valid in three dimensions, we thus found that the physics around the splitting point is the same as argued in Ref. [112]. However, due to the competition with the normal phase, the gapless phases disappear at some point, probably before the unitarity is

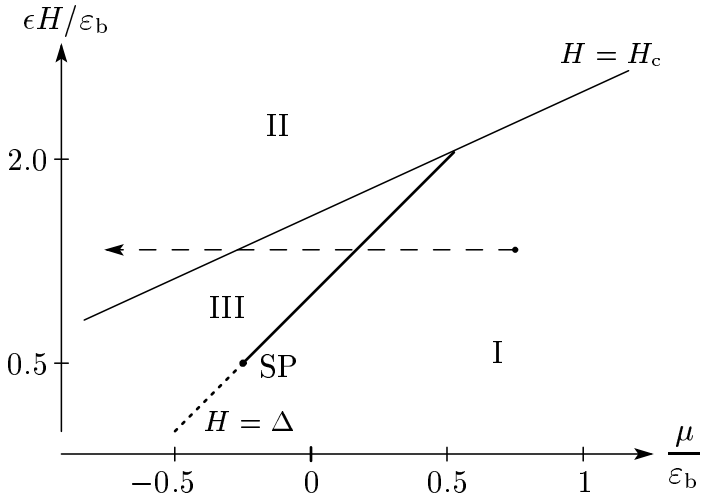

Figure 4.3: Schematic phase diagram of the polarized Fermi gas near the unitarity limit in the H-μ plane for the fixed binding energy $\varepsilon_b > 0$. The phases I, II, and III are same as in Fig. 4.2. The horizontal dashed line from right to left tracks the chemical potentials (μ, H) in trapped Fermi gases from the center to the peripheral.

reached. The point where this happens can be estimated from our calculations to be

$$(ak_F)^{-1} = \sqrt{2\sigma} = 0.494. \tag{4.24}$$

The gapless phase with spatially varying condensate exists in a finite range $0.494 < (ak_F)^{-1} < 1$. Thus the ϵ expansion does not support the hypothesis of Ref. [112] that the region of the gapless state with spatially varying condensate is connected with the FFLO region on the BCS side (see Fig. 4.1).

Chapter 5

Fermions with unequal masses

5.1 Two-body scattering in vacuum

Now we generalize our discussion on the unitary Fermi gas in the ϵ expansion to the fermions with unequal masses $m_\uparrow \neq m_\downarrow$, especially to study the phase structure of unitary Fermi gas with unequal densities and masses. As we mentioned in the previous Chapter, such asymmetric systems of fermions with density and mass imbalances will be interesting as a prototype of high density quark matter in the core of neutron stars, where the density and mass asymmetries exist among different quark flavors [62, 63, 64, 65, 66]. So far the phase structure of the two-component Fermi gas with density and mass imbalances in the BCS-BEC crossover has been studied within the mean-field approximation [126, 127, 128, 129], which is not a controllable approximation in the strong-coupling unitary regime.

First we reconsider the two-fermion scattering in vacuum studied in Chap. 2. As a result of the summation of the geometric series of bubble diagrams, the inverse T-matrix of the two-body scattering is given by

$$T(p_0, \boldsymbol{p})^{-1} = \frac{1}{c_0} + \int \frac{d\boldsymbol{k}}{(2\pi)^d} \frac{1}{p_0 - \frac{\left(\frac{\boldsymbol{p}}{2}+\boldsymbol{k}\right)^2}{2m_\uparrow} - \frac{\left(\frac{\boldsymbol{p}}{2}-\boldsymbol{k}\right)^2}{2m_\downarrow} + i\delta}. \tag{5.1}$$

The limit of infinite scattering length corresponds to $1/c_0 \to 0$ as before. Introducing the total mass $M = m_\uparrow + m_\downarrow$ and the reduced mass $m_\mathrm{r} = m_\uparrow m_\downarrow/(m_\uparrow + m_\downarrow)$, the inverse T-matrix at $d = 4 - \epsilon$ spatial dimensions to the leading order in ϵ can be written as

$$T(p_0, \boldsymbol{p})^{-1} = \frac{1}{c_0} - \frac{2}{\epsilon}\left(\frac{m_\mathrm{r}}{2\pi}\right)^2 \left(p_0 - \frac{\boldsymbol{p}^2}{2M} + i\delta\right) + \cdots. \tag{5.2}$$

This result suggests that the boson propagator is given by

$$D(p_0, \boldsymbol{p}) = \left(p_0 - \frac{\boldsymbol{p}^2}{2M} + i\delta\right)^{-1} \tag{5.3}$$

with the fermion-boson effective coupling

$$g^2 \simeq \frac{2\pi^2\epsilon}{m_\mathrm{r}^2}. \tag{5.4}$$

The binding energy $\varepsilon_{\rm b} > 0$ is obtained as the location of the pole of the T-matrix at zero external momentum: $T(-\varepsilon_{\rm b}, \mathbf{0})^{-1} = 0$. From Eq. (5.1), we see c_0 is related with $\varepsilon_{\rm b}$ via the following equation

$$\frac{1}{c_0} = \Gamma\left(1 - \frac{d}{2}\right)\left(\frac{m_{\rm r}}{2\pi}\right)^{\frac{d}{2}} \varepsilon_{\rm b}^{\frac{d}{2}-1}. \tag{5.5}$$

Near the four spatial dimensions, the relationships between $\varepsilon_{\rm b}$ and c_0 to the next-to-leading order in $\epsilon = 4 - d$ is given by

$$\frac{1}{c_0} \simeq -\frac{\varepsilon_{\rm b}}{2\epsilon}\left(\frac{m_{\rm r}}{\pi}\right)^2 \left[1 + \frac{\epsilon}{2}(1-\gamma)\right]\left(\frac{m_{\rm r}\varepsilon_{\rm b}}{2\pi}\right)^{-\frac{\epsilon}{2}}. \tag{5.6}$$

5.2 ϵ expansion with unequal masses

Now we consider the finite density system. The formalism of the ϵ expansion developed in the equal mass case in Chap. 3 holds just by replacing the boson propagator $D(p)$ by Eq. (5.3) and the fermion-boson effective coupling g by

$$g = \frac{(2\pi^2\epsilon)^{1/2}}{m_{\rm r}}\left(\frac{m_{\rm r}\phi_0}{\pi}\right)^{\epsilon/4}. \tag{5.7}$$

Then the Lagrangian density under consideration is given by

$$\mathcal{L}_0 = \Psi^\dagger\left(i\partial_t + H + \frac{\sigma_3 + \kappa}{4m_{\rm r}}\boldsymbol{\nabla}^2 + \sigma_+\phi_0 + \sigma_-\phi_0\right)\Psi + \varphi^*\left(i\partial_t + \frac{\boldsymbol{\nabla}^2}{2M}\right)\varphi - \frac{\phi_0^2}{c_0}, \tag{5.8}$$

$$\mathcal{L}_1 = g\Psi^\dagger\sigma_+\Psi\varphi + g\Psi^\dagger\sigma_-\Psi\varphi^* + \mu\Psi^\dagger\sigma_3\Psi + \left(2\mu - \frac{g^2}{c_0}\right)\varphi^*\varphi - \frac{g\phi_0}{c_0}\varphi - \frac{g\phi_0}{c_0}\varphi^*, \tag{5.9}$$

$$\mathcal{L}_2 = -\varphi^*\left(i\partial_t + \frac{\boldsymbol{\nabla}^2}{2M}\right)\varphi - 2\mu\varphi^*\varphi. \tag{5.10}$$

where $\mu_\sigma = \mu \pm H$ and $1/2m_\sigma = (1 \pm \kappa)/4m_{\rm r}$. We introduced the dimensionless parameter $-1 < \kappa < 1$ defined by

$$\kappa \equiv -\frac{m_\uparrow - m_\downarrow}{m_\uparrow + m_\downarrow}, \tag{5.11}$$

which measures the mass difference between two fermions.

The Lagrangian density $\mathcal{L}_0$ generates the fermion propagator given by

$$G(p_0, \boldsymbol{p}) = \frac{1}{(p_0 + H - \kappa\varepsilon_{\boldsymbol{p}})^2 - E_{\boldsymbol{p}}^2 + i\delta}\begin{pmatrix} p_0 + H - \kappa\varepsilon_{\boldsymbol{p}} + \varepsilon_{\boldsymbol{p}} & -\phi_0 \\ -\phi_0 & p_0 + H - \kappa\varepsilon_{\boldsymbol{p}} - \varepsilon_{\boldsymbol{p}} \end{pmatrix}, \tag{5.12}$$

where $\varepsilon_{\boldsymbol{p}} = \boldsymbol{p}^2/4m_{\rm r}$ and $E_{\boldsymbol{p}} = \sqrt{\varepsilon_{\boldsymbol{p}}^2 + \phi_0^2}$, and the boson propagator given by

$$D(p_0, \boldsymbol{p}) = \left(p_0 - \frac{\boldsymbol{p}^2}{2M} + i\delta\right)^{-1} = \left(p_0 - \frac{1-\kappa^2}{2}\varepsilon_{\boldsymbol{p}} + i\delta\right)^{-1}. \tag{5.13}$$

We can use the same Feynman rule and the same power counting rule of ϵ as the equal mass case developed in Sec. 3.2, as far as the mass difference is not so large. When the mass difference is

as large as $|\kappa| \simeq 1 - O(1/\epsilon)$, the power counting rule of ϵ breaks down because of the existence of another large parameter $m_{\rm heavy}/m_{\rm light} \sim 1/\epsilon$. Accordingly, the fermion-boson scattering leads to the three-body bound states (Efimov states) in vacuum when the mass ratio is given by $m_{\rm heavy}/m_{\rm light} = 4/\epsilon + O(1)$ [134, 135, 136]. In this Chapter, we will only consider the case where the mass difference is at most $\kappa \sim O(1)$ and free from the Efimov states. First we will determine the pressure and the fermion quasiparticle spectrum to the leading and next-to-leading orders in ϵ at the unpolarized ground state where $H = 0$. Then we investigate the phase structure of polarized Fermi gas with the small mass difference $\kappa \sim \epsilon$.

5.3 Effective potential and pressure

The computation of the effective potential with finite κ is straightforward according to the systematic expansion over ϵ. Since $\kappa\varepsilon_{\boldsymbol{p}} < E_{\boldsymbol{p}}$ for any momentum $\boldsymbol{p}$, κ does not appear at the one-loop level. Therefore, the effective potential from the tree and one-loop diagrams depends only on the reduced mass $m_{\rm r}$ as

$$\begin{aligned} &V_0(\phi_0) + V_1(\phi_0) \\ &\quad = \frac{\phi_0^2}{c_0} - \int \frac{d\boldsymbol{p}}{(2\pi)^d}\left(E_{\boldsymbol{p}} + \mu\frac{\varepsilon_{\boldsymbol{p}}}{E_{\boldsymbol{p}}}\right) \\ &\quad = \frac{\phi_0^2}{c_0} + \left[\frac{\phi_0}{3}\left\{1 + \frac{7 - 3(\gamma + \ln 2)}{6}\epsilon\right\} - \frac{\mu}{\epsilon}\left\{1 + \frac{1 - 2(\gamma - \ln 2)}{4}\epsilon\right\}\right]\left(\frac{m_{\rm r}\phi_0}{\pi}\right)^{d/2}. \end{aligned} \tag{5.14}$$

The effective potential at two-loop level is given by the same diagram in Fig. 3.3 as

$$\begin{aligned} V_2(\phi_0) &= g^2 \int \frac{dp\, dq}{(2\pi)^{2d+2}} G_{11}(p) G_{22}(q) D(p - q) \\ &= -\frac{g^2}{4}\int \frac{d\boldsymbol{p}\, d\boldsymbol{q}}{(2\pi)^{2d}} \frac{(E_{\boldsymbol{p}} - \varepsilon_{\boldsymbol{p}})(E_{\boldsymbol{q}} - \varepsilon_{\boldsymbol{q}})}{E_{\boldsymbol{p}} E_{\boldsymbol{q}}\left[E_{\boldsymbol{p}} + E_{\boldsymbol{q}} + \frac{1-\kappa^2}{2}\varepsilon_{\boldsymbol{p}-\boldsymbol{q}} - \kappa\varepsilon_{\boldsymbol{p}} + \kappa\varepsilon_{\boldsymbol{q}}\right]}. \end{aligned} \tag{5.15}$$

Changing the integration variables to $x = \varepsilon_{\boldsymbol{p}}/\phi_0$, $y = \varepsilon_{\boldsymbol{q}}/\phi_0$, and $\cos\theta = \hat{\boldsymbol{p}} \cdot \hat{\boldsymbol{q}}$, the integral can be expressed by

$$V_2(\phi_0) = -\epsilon\left(\frac{m_{\rm r}\phi_0}{\pi}\right)^2 \frac{\phi_0}{\pi}\int_0^\infty dx \int_0^\infty dy \int_0^\pi d\theta\, xy \sin^2\theta \frac{[f(x) - x][f(y) - y]}{f(x) f(y)\left[g_\kappa(x, y) - (1 - \kappa^2)\sqrt{xy}\cos\theta\right]} \tag{5.16}$$

with $f(x) = \sqrt{x^2 + 1}$ and $g_\kappa(x, y) = f(x) + f(y) + \frac{1-\kappa^2}{2}(x + y) - \kappa(x - y)$. The integration over θ can be performed analytically to lead to

$$V_2(\phi_0) = -C_\kappa \epsilon\left(\frac{m_{\rm r}\phi_0}{\pi}\right)^2 \phi_0 \tag{5.17}$$

where C_κ is a function of κ given by a two-dimensional integral

$$C_\kappa = \int_0^\infty dx \int_0^\infty dy \frac{[f(x) - x][f(y) - y]}{f(x) f(y)} \frac{g_\kappa(x, y) - \sqrt{g_\kappa(x, y)^2 - (1 - \kappa^2)^2 xy}}{(1 - \kappa^2)^2}. \tag{5.18}$$

C_κ is symmetric under $\kappa \to -\kappa$ and numerically we find C_κ is an increasing function of κ at $0 \le \kappa < 1$. In the equal mass limit $\kappa = 0$, we reproduce $C_0 \approx 0.14424$ in Eq. (3.35).

Consequently, we obtain the effective potential $V_{\rm eff} = V_0 + V_1 + V_2$ up to the next-to-leading order in ϵ,

$$V_{\rm eff}(\phi_0) = \frac{\phi_0^2}{c_0} + \left[\frac{\phi_0}{3}\left\{1 + \frac{7 - 3(\gamma + \ln 2)}{6}\epsilon - 3C_\kappa\epsilon\right\} - \frac{\mu}{\epsilon}\left\{1 + \frac{1 - 2(\gamma - \ln 2)}{4}\epsilon\right\}\right]\left(\frac{m_{\rm r}\phi_0}{\pi}\right)^{d/2}. \quad (5.19)$$

Comparing $V_{\rm eff}(\phi_0)$ with the effective potential in the equal mass case in Eq. (3.36), we see the solution of the gap equation ϕ_0 is simply given by replacing the fermion mass m by $2m_{\rm r}$ and the constant C by C_κ. Using the relation of c_0 with the binding energy of boson $\varepsilon_{\rm b}$ in Eq. (5.5), we obtain the condensate as

$$\phi_0 = \frac{2\mu}{\epsilon}\left[1 + (3C_\kappa - 1 + \ln 2)\,\epsilon\right] + \frac{\varepsilon_{\rm b}}{\epsilon}\left[1 + \left(3C_\kappa - \frac{1}{2} + \ln 2 - \frac{1}{2}\ln\frac{\varepsilon_{\rm b}}{\phi_0}\right)\epsilon\right]. \quad (5.20)$$

Then the pressure up to the next-to-leading order in ϵ is given by

$$P = -V_{\rm eff}(\phi_0) = \frac{\phi_0}{6}\left[1 + \left(\frac{17}{12} - 3C_\kappa - \frac{\gamma + \ln 2}{2}\right)\epsilon - \frac{3\varepsilon_{\rm b}}{4\phi_0}\right]\left(\frac{m_{\rm r}\phi_0}{\pi}\right)^{d/2}. \quad (5.21)$$

When the mass difference κ is as small as ϵ which is the case we will concentrate on later, we can neglect the κ dependence in C_κ to give $C \approx 0.14424$. In this case, the pressure of the superfluid state up to the order $O(\epsilon)$ depends only on $m_{\rm r}$ and not on κ at all.

5.4 Self-energy and dispersion relation

Let us turn to the computation of the fermion quasiparticle spectrum with finite κ. To the leading order in ϵ, the dispersion relation of fermion quasiparticles are given by

$$\omega_{\rm F}(\boldsymbol{p}) = E_{\boldsymbol{p}} \pm \kappa\varepsilon_{\boldsymbol{p}}. \quad (5.22)$$

The lighter fermion has the energy gap $\Delta = \phi_0$ at $\varepsilon_{\boldsymbol{p}} = 0$, while the heavier fermion has the energy gap $\Delta = \sqrt{1-\kappa^2}\,\phi_0$ at $\varepsilon_{\boldsymbol{p}} = |\kappa|\,\phi_0/\sqrt{1-\kappa^2}$. The next-to-leading order corrections to the dispersion relation come from the μ insertion to the fermion propagator and the one-loop self-energy diagrams, $-i\Sigma(p)$, depicted in Fig. 3.4. The one-loop diagrams in Fig. 3.4 give corrections to the diagonal elements of the fermion self-energy, which is evaluated as

$$\begin{aligned}\Sigma_{11}(p) &= ig^2\int\frac{dk}{(2\pi)^{d+1}}\,G_{22}(k)D(p-k)\\ &= -\frac{g^2}{2}\int\frac{d\boldsymbol{k}}{(2\pi)^d}\,\frac{E_{\boldsymbol{k}} - \varepsilon_{\boldsymbol{k}}}{E_{\boldsymbol{k}}\left[E_{\boldsymbol{k}} + \kappa\varepsilon_{\boldsymbol{k}} + \frac{1-\kappa^2}{2}\varepsilon_{\boldsymbol{k}-\boldsymbol{p}} - p_0\right]},\end{aligned} \quad (5.23)$$

and

$$\begin{aligned}\Sigma_{22}(p) &= ig^2\int\frac{dk}{(2\pi)^{d+1}}\,G_{11}(k)D(k-p)\\ &= \frac{g^2}{2}\int\frac{d\boldsymbol{k}}{(2\pi)^d}\,\frac{E_{\boldsymbol{k}} - \varepsilon_{\boldsymbol{k}}}{E_{\boldsymbol{k}}\left[E_{\boldsymbol{k}} - \kappa\varepsilon_{\boldsymbol{k}} + \frac{1-\kappa^2}{2}\varepsilon_{\boldsymbol{k}-\boldsymbol{p}} + p_0\right]}.\end{aligned} \quad (5.24)$$

From now on, we concentrate on the case where the mass difference is as small as $\kappa \sim \epsilon$, where we will see interesting physics in the phase diagram. In this case, we can neglect the κ dependence in Σ_{11} and Σ_{22} to the order $O(\epsilon)$ because Σ is already small by the factor $g^2 \sim \epsilon$. Therefore, the modification of the fermion quasiparticle spectrum due to the finite κ comes from Eq. (5.22). Following the calculations in Sec. 3.5, we find that the dispersion relation of the fermion quasiparticle around its minimum has the following form

$$\omega_{\mathrm{F}}(\boldsymbol{p}) \simeq \Delta + \frac{(\varepsilon_{\boldsymbol{p}} \pm \kappa\phi_0 - \varepsilon_0)^2}{2\phi_0} \simeq \sqrt{(\varepsilon_{\boldsymbol{p}} \pm \kappa\phi_0 - \varepsilon_0)^2 + \Delta^2}. \tag{5.25}$$

Here Δ is the energy gap of the fermion quasiparticle defined in Eq. (3.54) and ε_0 is given by Eq. (3.55). Note that the energy gap is not affected by κ up to the order $O(\epsilon)$. The minimum of the dispersion curve is located at a nonzero value of momentum $|\boldsymbol{p}|$ satisfying $\varepsilon_{\boldsymbol{p}} = \varepsilon_0 - |\kappa|\phi_0$ for the lighter fermion and $\varepsilon_{\boldsymbol{p}} = \varepsilon_0 + |\kappa|\phi_0$ for the heavier fermion when those are positive.

5.5 Critical polarizations and phase diagram

Since the result should be symmetric under $H \to -H$ and $\kappa \to -\kappa$, we can choose $H > 0$ without losing generality. Accordingly, $\kappa > 0$ (< 0) corresponds to the system where the majority is the lighter (heavier) fermions and an increase of κ means a decrease of major fermion's mass. When H is increased, the phase transition to the normal Fermi gas occurs at $H - \Delta \sim \epsilon$. The critical polarization H_{c} is given where the pressure of the superfluid state coincides with that of the normal state with the same chemical potentials. The pressure of the superfluid state is given by Eq. (5.21) because the contribution of the polarized quasiparticles to the pressure is $O(\epsilon^3)$ and negligible [see Eq. (4.16)]. On the other hand, since $H \sim \phi_0 \gg \mu \sim \epsilon\phi_0$, the pressure of the normal state is given by that of the fully polarized free Fermi gas

$$P_{\mathrm{n}} = \int \frac{d\boldsymbol{p}}{(2\pi)^d} \left(\mu_\uparrow - \frac{\boldsymbol{p}^2}{2m_\uparrow}\right)_> = \frac{(H+\mu)^{\frac{d}{2}+1}}{\Gamma\left(\frac{d}{2}+2\right)} \left(\frac{m_{\mathrm{r}}/\pi}{1+\kappa}\right)^{\frac{d}{2}}. \tag{5.26}$$

The condition $P = P_{\mathrm{n}}$ for the phase transition to the normal state gives the critical polarization $H = H_{\mathrm{c}}$ normalized by the energy gap at zero polarization Δ in Eq. (3.54) as

$$\frac{H_{\mathrm{c}}}{\Delta} = 1 - \epsilon\sigma + \frac{\varepsilon_{\mathrm{b}}}{4\Delta} + \frac{2}{3}\kappa + O(\epsilon^2). \tag{5.27}$$

The number $\sigma \approx 0.12197$ is defined in Eq. (4.19). When $H_{\mathrm{c}} > \Delta$, the gapless superfluid state appears at $\Delta < H < H_{\mathrm{c}}$. In particular, in the unitarity limit $\varepsilon_{\mathrm{b}} = 0$, the gapless superfluid state is possible when the majority is the lighter fermions and the mass difference is as large as $\kappa/\epsilon > 3\sigma/2 = 0.183$. The phase boundary between the superfluid and normal phases H_{c}/Δ in the unitarity limit as a function of κ/ϵ is illustrated in Fig. 5.1.

The minimum of the dispersion curve for the major fermions is located at a nonzero value of momentum $|\boldsymbol{p}|$ satisfying

$$\varepsilon_0 - \kappa\phi_0 = (\epsilon - \kappa)\,\Delta - \frac{\varepsilon_{\mathrm{b}}}{2} + O(\epsilon^2). \tag{5.28}$$

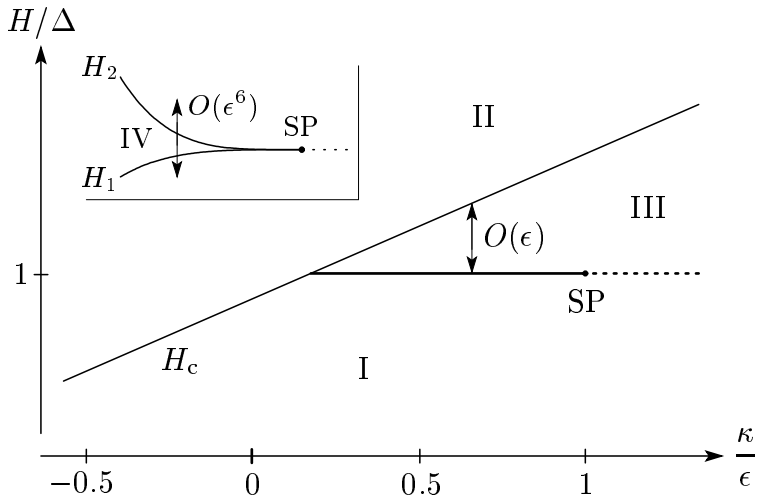

Figure 5.1: Schematic phase diagram of the polarized Fermi gas with unequal masses in the unitarity limit from the ϵ expansion. $\kappa > 0$ (< 0) corresponds to the system where the majority is the lighter (heavier) fermions and an increase of κ means a decrease of major fermion's mass. The phase diagram can be divided into four phases, I: the gapped superfluid phase, II: the polarized normal phase, III: the gapless superfluid phase, and IV: the phase with spatially varying condensate. The inset is the magnification of the region around the splitting point (SP). The phase IV appears in the narrow region represented by the thick line between the phases I and III.

Therefore, we find the splitting point where the minimum of the dispersion curve sits exactly at zero momentum exists at

$$\frac{\varepsilon_{\rm b}}{2\Delta} + \kappa = \epsilon. \tag{5.29}$$

The phase structure around the splitting point is determined by the same discussion given in Chap. 4 just by replacing ε_0 by $\varepsilon_0 - \kappa\phi_0$. There exists the phase with spatially varying condensate (or finite superfluid velocity) at $H_1 < H < H_2$, where

$$\frac{H_1}{\Delta} = 1 - 0.0843\,\epsilon^2 \left(\frac{\varepsilon_0}{\Delta} - \kappa\right)^4, \tag{5.30}$$

and

$$\frac{H_2}{\Delta} = 1 + 0.634\,\epsilon^2 \left(\frac{\varepsilon_0}{\Delta} - \kappa\right)^4. \tag{5.31}$$

Furthermore, the polarization for the disappearance of the inner Fermi surface H_3 is given by

$$\frac{H_3}{\Delta} = \frac{\omega_{\rm F}(\mathbf{0})}{\Delta} = 1 + \frac{1}{2}\left(\frac{\varepsilon_0}{\Delta} - \kappa\right)^2. \tag{5.32}$$

If $\Delta < H < H_3$, fermion quasiparticles which have momentum $\omega_{\rm F}(\boldsymbol{p}) < H$ are filled and hence there exist two Fermi surfaces, while there is only one Fermi surface for $H_3 < H$. Since $\varepsilon_0 - \kappa\phi_0 = (\epsilon - \kappa)\,\Delta$ in the unitarity limit $\varepsilon_{\rm b} = 0$, the splitting point is located at $\kappa = \epsilon$. The critical polarization for the

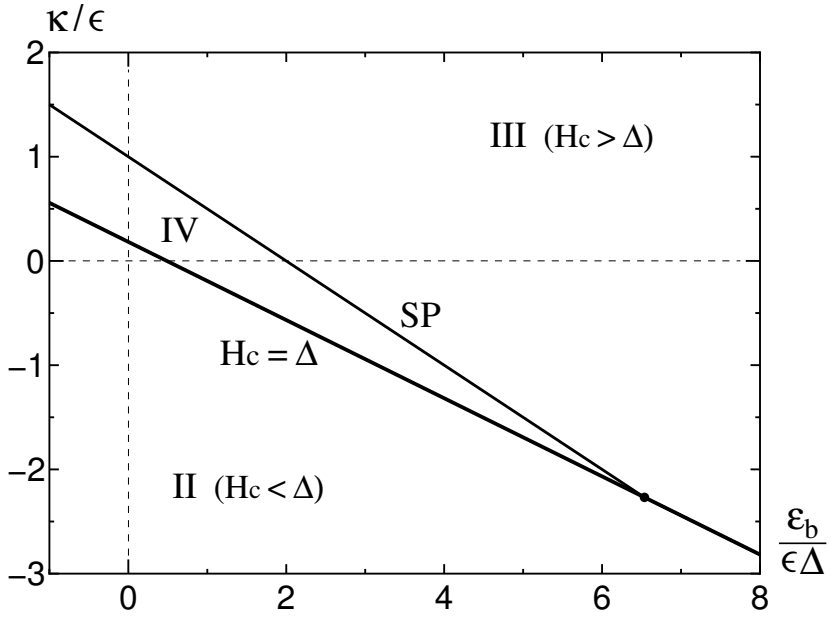

Figure 5.2: Phase diagram of the polarized Fermi gas in the plane of binding energy ε_b and mass difference κ from the ϵ expansion. Two solid lines show $H_c = \Delta$ in Eq. (5.34) and the location of the splitting point (SP) in Eq. (5.29). The intersection of these two lines is given by Eq. (5.35). The phases II, III, and IV represents the ground state slightly above $H = \Delta$. The phase diagrams in the equal mass limit $\kappa = 0$ and in the unitarity limit $\varepsilon_b = 0$ with H-axis are already illustrated in Fig. 4.2 and Fig. 5.1, respectively.

phase transition to the normal state at this point is $H_c/\Delta = 1 + 0.545\epsilon > 0$. Therefore, the phase with spatially varying condensate and the phase with two Fermi surfaces are stably exist in the unitarity limit with finite mass difference given by

$$\frac{3}{2}\sigma < \frac{\kappa}{\epsilon} < 1. \tag{5.33}$$

The critical polarizations H_1/Δ and H_2/Δ in the unitarity limit as functions of κ/ϵ are illustrated in Fig. 5.1.

Finally, we discuss the whole phase structure of the polarized Fermi gas with unequal masses near the unitarity limit. $H_c(\varepsilon_b, \kappa)$ in Eq. (5.27) is a function of the binding energy ε_b and the mass difference κ. Hence $H = H_c$ forms a single plane in the three-dimensional phase diagram in the space of ε_b/Δ, κ, and H/Δ, which separates the superfluid phase at $H < H_c$ from the polarized normal phase at $H > H_c$. The splitting point given by Eq. (5.29) with $H = \Delta$ forms a "line" in such a three-dimensional phase diagram. The superfluid phase with spatially varying condensate emerges from the SP line, which occupies a finite region in the phase diagram between the gapped superfluid phase at $H < H_1$ and the gapless superfluid phase at $H_2 < H < H_c$.

Fig. 5.2 shows a part of such a three-dimensional phase diagram in the space of ε_b/Δ, κ, and H/Δ, sliced slightly above $H = \Delta$. When $H_c < \Delta$ for a given set of ε_b and κ (lower half of the $H_c = \Delta$ line

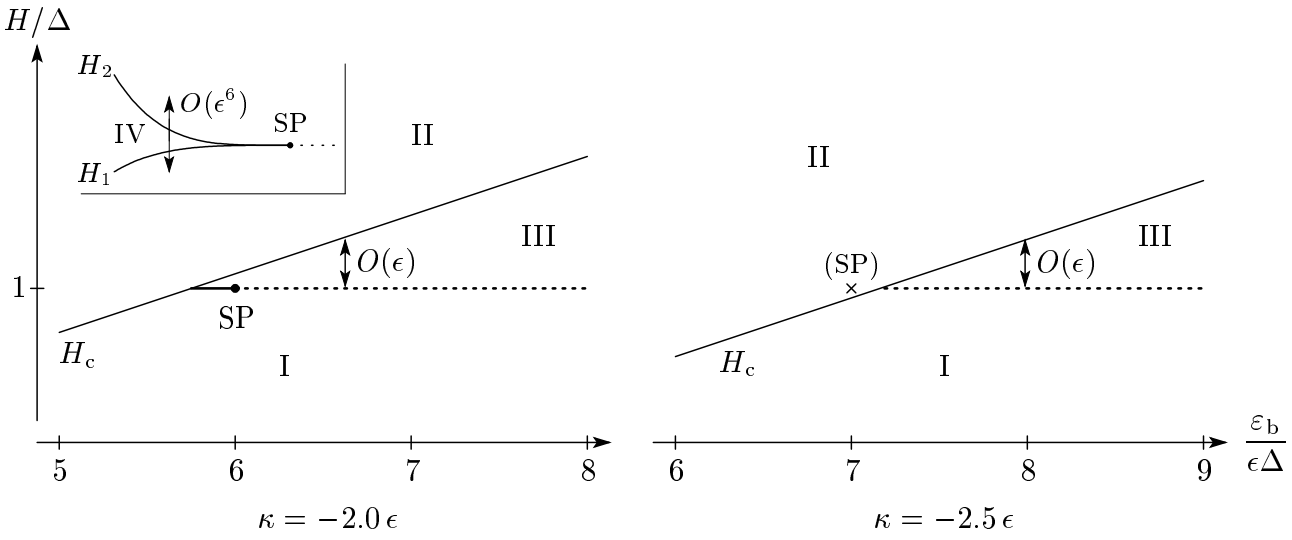

Figure 5.3: Schematic phase diagram of the polarized Fermi gas in the H-ε_b plane near the disappearance of the splitting point at $\kappa = -2.0\,\epsilon$ and $-2.5\,\epsilon$. The phases I, II, III, and VI are same as in Fig. 5.1. If $\kappa > -2.27\,\epsilon$ (left panel), the splitting point and the phase with spatially varying condensate stably exist, while those become unstable when $\kappa < -2.27\,\epsilon$ (right panel).

in Fig. 5.2), the superfluid state is unstable at $H = \Delta$ and there exists the phase transition from the gapped superfluid state to the polarized normal state (II). On the other hand, when $H_c > \Delta$ (upper half of the $H_c = \Delta$ line in Fig. 5.2), the superfluid is stable even at $H > \Delta$ and the gapless superfluid state (III) appears there. The boundary $H_c = \Delta$ dividing the phase diagram in the plane of ε_b and κ into these two regions is given from Eq. (5.27) by

$$\frac{\varepsilon_b}{4\Delta} + \frac{2}{3}\kappa = \epsilon\sigma \tag{5.34}$$

As the mass of major fermions is increased (or κ is decreased), the boundary shifts to the larger value of ε_b because the pressure of the normal state increases. Consequently, the polarized normal state occupies the wider domain near the unitarity limit.

The region where $H_c > \Delta$ can be further divided into two regions according to whether the minimum of the dispersion curve is located at a nonzero value of momentum $\varepsilon_0 - \kappa\phi_0 > 0$ or not. If $\varepsilon_0 - \kappa\phi_0 > 0$ (below the SP line in Fig. 5.2), there exist the superfluid state with spatially varying condensate (IV) between the normal state and the gapless superfluid state. The boundary $\varepsilon_0 = \kappa\phi_0$ represents the line of the splitting point given by Eq. (5.29). As the mass of major fermions is increased, the region for the superfluid phase with spatially varying condensate shrinks. Eventually, such a phase disappears at the following point where the two lines $H_c = \Delta$ and $\varepsilon_0 = \kappa\phi_0$ merges

$$\begin{aligned} \frac{\varepsilon_b}{\Delta} &= 4\,(2 - 3\sigma)\,\epsilon = 6.54\,\epsilon, \\ \kappa &= -3\,(1 - 2\sigma)\,\epsilon = -2.27\,\epsilon. \end{aligned} \tag{5.35}$$

Therefore, if the mass difference is as large as $\kappa < -2.27\,\epsilon$ with major heavier fermions, the splitting point becomes unstable towards the polarized normal state and the superfluid phase with spatially varying condensate never appears for any value of the binding energy ε_b. The schematic phase diagram in the plane of ε_b and H near the disappearance of the splitting point is illustrated in Fig. 5.3 by taking the typical values at $\kappa = -2.0\,\epsilon$ and $-2.5\,\epsilon$.

5.6 Summary on the phase structure of polarized Fermi gas

In Chapters 4 and 5, the phase structure of the polarized Fermi gas with equal and unequal fermion masses has been studied in the unitary regime based on the ϵ expansion around four spatial dimensions. Although our results are valid only near four spatial dimensions where $\epsilon \ll 1$, we can draw the following conclusions assuming that the picture remains qualitatively valid in three dimensions. At unitarity in the equal mass limit, there is a first-order phase transition from the unpolarized superfluid state to the fully polarized normal state. On the BEC side of the unitarity point, the gapless superfluid phase and the superfluid phase with spatially varying condensate stably exist between the gapped superfluid phase and the polarized normal phase in a certain range of the binding energy and the mass difference. In the equal mass limit (Fig. 4.2), our study gives a microscopic foundation to the phase structure around the splitting point, which has been proposed on the BEC side of the unitarity point using the effective field theory [112]. Moreover, we found the gapless phases terminate at some point before the unitarity is reached due to the competition with the polarized normal state. The naive extrapolation of our result (4.23) with the use of Eq. (2.14) estimates the range of the superfluid phase with spatially varying condensate to be $0.494 \lesssim (ak_F)^{-1} \lesssim 1$ at three dimensions $\epsilon \to 1$.

We also found the splitting point and the same phase structure around it in the unitarity limit but with finite mass difference between two fermion species when the majority is the lighter fermions ($\kappa > 0$ in Fig. 5.1). The range of the superfluid phase with spatially varying condensate can be estimated from Eq. (5.33) to be $1.37 \lesssim m_{\text{minority}}/m_{\text{majority}} \lesssim 3$ at $\epsilon \to 1$. Such splitting points form a smooth line on the $H = \Delta$ plane of the three-dimensional phase diagram in the space of ε_b/Δ, κ, and H/Δ. It gets away from the unitarity with increasing the mass of major fermions (or decreasing κ in Fig. 5.2). Eventually the splitting point becomes unstable due to the competition with the polarized normal state at the point in Eq. (5.35), which we estimate to be $(ak_F)^{-1} \approx 1.81$ and $m_{\text{majority}}/m_{\text{minority}} \approx 5.54$. Accordingly, the region for the superfluid phase with spatially varying condensate shrinks and eventually disappears. The superfluid state with finite superfluid velocity is never realized for any value of the binding energy ε_b for a sufficiently large mass difference where the majority is the heavier fermions $m_{\text{majority}}/m_{\text{minority}} \gtrsim 5.54$. While our quantitative results are not reliable at three dimensions, it is interesting to point out that our estimates on the mass ratios are well below the critical value at $d = 3$, $m_{\text{heavy}}/m_{\text{light}} = 13.6$, where the instability occurs due to the Efimov effect [134, 135, 136]. Further study will be worthwhile to confirm these possibilities.

Chapter 6

Expansion around two spatial dimensions

6.1 Lagrangian and Feynman rules

In this Chapter, we formulate the systematic expansion for the unitary Fermi gas around two spatial dimensions in a similar way as we have done for the $\epsilon = 4 - d$ expansion. Here we start with the Lagrangian density given in Eq. (3.2) limited to the unpolarized Fermi gas in the unitarity limit where $H = 0$ and $1/c_0 = 0$:

$$\mathcal{L} = \Psi^\dagger \left(i\partial_t + \frac{\sigma_3 \boldsymbol{\nabla}^2}{2m} + \mu\sigma_3 \right) \Psi + \Psi^\dagger \sigma_+ \Psi \phi + \Psi^\dagger \sigma_- \Psi \phi^* . \tag{6.1}$$

Then we expand the field ϕ around its vacuum expectation value ϕ_0 as

$$\phi = \phi_0 + \bar{g}\varphi, \qquad \bar{g} = \left(\frac{2\pi\bar{\epsilon}}{m} \right)^{1/2} \left(\frac{m\mu}{2\pi} \right)^{-\bar{\epsilon}/4}, \tag{6.2}$$

where the effective coupling $\bar{g} \sim \bar{\epsilon}^{1/2}$ in Eq. (2.10) was introduced. The extra factor $(m\mu/2\pi)^{-\bar{\epsilon}/4}$ was chosen so that the product of fields $\varphi^*\varphi$ has the same dimension as the Lagrangian density [1].

Then we rewrite the Lagrangian density as a sum of three parts, $\mathcal{L} = \bar{\mathcal{L}}_0 + \bar{\mathcal{L}}_1 + \bar{\mathcal{L}}_2$, where

$$\bar{\mathcal{L}}_0 = \Psi^\dagger \left(i\partial_t + \frac{\sigma_3 \boldsymbol{\nabla}^2}{2m} + \mu\sigma_3 + \sigma_+\phi_0 + \sigma_-\phi_0 \right) \Psi \,, \tag{6.3}$$

$$\bar{\mathcal{L}}_1 = -\varphi^*\varphi + \bar{g}\Psi^\dagger \sigma_+ \Psi\varphi + \bar{g}\Psi^\dagger \sigma_- \Psi\varphi^*, \tag{6.4}$$

$$\bar{\mathcal{L}}_2 = \varphi^*\varphi \,. \tag{6.5}$$

The part $\bar{\mathcal{L}}_0$ represents the gapped fermion quasiparticle, whose propagator is given by

$$\bar{G}(p_0, \boldsymbol{p}) = \frac{1}{p_0^2 - \bar{E}_{\boldsymbol{p}}^2 + i\delta} \begin{pmatrix} p_0 + \varepsilon_{\boldsymbol{p}} - \mu & -\phi_0 \\ -\phi_0 & p_0 - \varepsilon_{\boldsymbol{p}} + \mu \end{pmatrix}, \tag{6.6}$$

[1] The choice of the extra factor is arbitrary, if it has the correct dimension, and does not affect the final results because the difference can be absorbed into the redefinition of the fluctuation field φ. The particular choice of $\bar{g}$ in Eq. (6.2) will simplify the form of loop integrals in the intermediate steps.

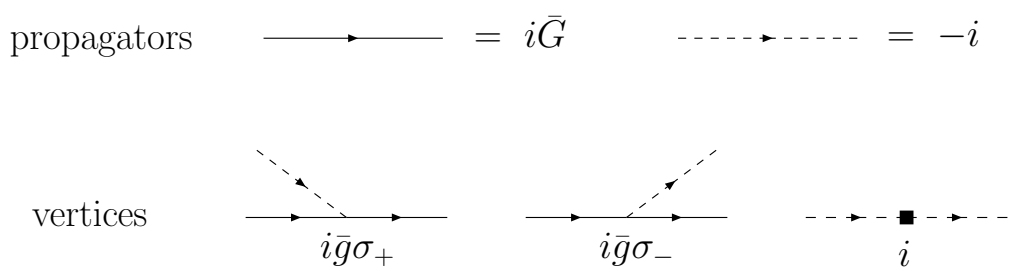

Figure 6.1: Feynman rules for the expansion around two spatial dimensions from the Lagrangian density in Eq. (6.3). The first line gives propagators, while the second line gives vertices.

with $\bar{E}_{\boldsymbol{p}} = \sqrt{(\varepsilon_{\boldsymbol{p}} - \mu)^2 + \phi_0^2}$ being the usual gapped quasiparticle spectrum in the BCS theory.

The second part $\bar{\mathcal{L}}_1$ represents the interaction between fermions induced by the auxiliary field φ. The first term in $\bar{\mathcal{L}}_1$ gives the propagator of the auxiliary field φ

$$\bar{D}(p_0, \boldsymbol{p}) = -1, \tag{6.7}$$

and the last two terms give vertices coupling two fermions and φ. If we did not have the part $\bar{\mathcal{L}}_2$, we could integrate out the auxiliary fields φ and φ^* to lead to

$$\bar{\mathcal{L}}_1 \to \bar{g}^2 \Psi^\dagger \sigma_+ \Psi \, \Psi^\dagger \sigma_- \Psi = \bar{g}^2 \psi_\uparrow^\dagger \psi_\downarrow^\dagger \psi_\downarrow \psi_\uparrow, \tag{6.8}$$

which gives the contact interaction of fermions with the small coupling $\bar{g}^2 \sim \bar{\epsilon}$ as depicted in Fig. 2.1. The vertex in the third part $\bar{\mathcal{L}}_2$ plays a role of a counter term so as to avoid double counting of a certain type of diagram which is already taken into $\bar{\mathcal{L}}_1$ as we will see below. The Feynman rules corresponding to these Lagrangian densities are summarized in Fig. 6.1.

6.2 Power counting rule of $\bar{\epsilon}$

We can construct the similar power counting rule of $\bar{\epsilon}$ as in the case of the expansion around four spatial dimensions. First, we make a prior assumption $\phi_0/\mu \sim e^{-1/\bar{\epsilon}}$, which will be checked later. Since $e^{-1/\bar{\epsilon}}$ is exponentially small compared to any powers of $\bar{\epsilon}$, we can neglect the contributions of ϕ_0 when we expand physical observables in powers of $\bar{\epsilon}$. Then, since each pair of fermion and φ vertices brings a factor of $\bar{\epsilon}$, the naive power of $\bar{\epsilon}$ for a given diagram is $N_{\bar{g}}/2$, where $N_{\bar{g}}$ is the number of couplings $\bar{g}$ from $\bar{\mathcal{L}}_1$.

However, this naive counting does not take into account the fact that there might be inverse powers of $\bar{\epsilon}$ that come from integrals which have logarithmic divergences at $d = 2$. Each loop integral in the ultraviolet region behaves as

$$\int dp_0 d\boldsymbol{p} \sim \int d\boldsymbol{p}\, \varepsilon_{\boldsymbol{p}} \sim p^4, \tag{6.9}$$

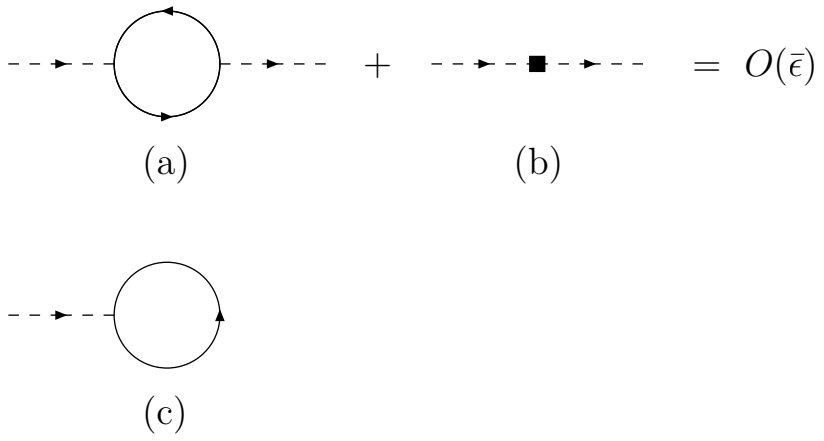

Figure 6.2: Two apparent exceptions of naive power counting rule of $\bar{\epsilon}$, (a, c). The boson self-energy diagram (a) is combined with the vertex from $\bar{\mathcal{L}}_2$ (b) to restore the naive $\bar{\epsilon}$ counting. The condition of disappearance of the tadpole diagram (c) gives the gap equation to determine the value of condensate ϕ_0.

while each fermion propagator behaves, at worst, as $\bar{G}(p) \sim p^{-2}$. Therefore, a given diagram may diverges as $\sim p^{\mathcal{D}}$ with $\mathcal{D}$ being the superficial degree of divergence given by

$$\mathcal{D} = 4L - 2P_{\mathrm{F}}. \tag{6.10}$$

Here L is the number of loop integrals and P_{F} is the number of fermion propagators. Using the similar relations to Eq. (3.13),

$$\begin{aligned} L &= P_{\mathrm{F}} + P_{\mathrm{B}} - N_{\bar{g}} + 1, \\ N_g &= P_{\mathrm{F}} + \frac{E_{\mathrm{F}}}{2} = 2P_{\mathrm{B}} + E_{\mathrm{B}}, \end{aligned} \tag{6.11}$$

the superficial degree of divergence is written in terms of the number of external fermion (auxiliary field) lines, $E_{\mathrm{F(B)}}$, as

$$\mathcal{D} = 4 - E_{\mathrm{F}} - 2E_{\mathrm{B}}. \tag{6.12}$$

Therefore, the inverse power of $\bar{\epsilon}$ is possible only in diagrams which satisfies $E_{\mathrm{F}} + 2E_{\mathrm{B}} \leq 4$. Moreover from the analytic properties of $G(p)$ in the ultraviolet region discussed in Eq. (3.16), one can show that there are only two skeleton diagrams which have the $1/\bar{\epsilon}$ singularity near two dimensions. They are one-loop diagrams of the boson self-energy [Figs. 6.2(a)], and the φ tadpole diagram [Fig. 6.2(c)].

The boson self-energy diagram in Fig. 6.2(a) is evaluated as

$$\begin{aligned} -i\bar{\Pi}_{\mathrm{a}}(p) &= -\bar{g}^2 \int \frac{dk}{(2\pi)^{d+1}} G_{11}\Big(k + \frac{p}{2}\Big) G_{22}\Big(k - \frac{p}{2}\Big) \\ &= i\bar{g}^2 \int \frac{d\boldsymbol{k}}{(2\pi)^d} \frac{\theta(\varepsilon_{\boldsymbol{k}+\frac{\boldsymbol{p}}{2}} - \mu) - \theta(\mu - \varepsilon_{\boldsymbol{k}-\frac{\boldsymbol{p}}{2}})}{2\varepsilon_{\boldsymbol{k}} - (p_0 - \frac{1}{2}\varepsilon_{\boldsymbol{p}} + 2\mu + i\delta)}, \end{aligned} \tag{6.13}$$

where we have neglected the contribution of ϕ_0. The integral over $\boldsymbol{k}$ is logarithmic divergent at $d = 2$ and has a pole at $\bar{\epsilon} = 0$. Thus it is $O(1)$ instead of $O(\bar{\epsilon})$ according to the naive counting. The residue at the pole can be computed as

$$\begin{aligned}\bar{\Pi}_{\mathrm{a}}(p) &= -\bar{g}^2 \int \frac{d\boldsymbol{k}}{(2\pi)^d} \frac{1}{2\varepsilon_{\boldsymbol{k}} - (p_0 - \frac{1}{2}\varepsilon_{\boldsymbol{p}} + 2\mu + i\delta)} + \cdots \\ &= 1 + O(\bar{\epsilon}),\end{aligned} \tag{6.14}$$

which is cancelled out exactly by adding the vertex $\bar{\Pi}_0 = -1$ in $\bar{\mathcal{L}}_2$. Therefore the diagram of the type in Fig. 6.2(a) should be combined with the vertex from $\bar{\mathcal{L}}_2$ in Fig. 6.2(b) to restore the naive $\bar{\epsilon}$ power counting result, $O(\bar{\epsilon})$.

Similarly, the tadpole diagram in Fig. 6.2(c) also contains the $1/\bar{\epsilon}$ singularity. The requirement that this tadpole diagram should vanish by itself gives the gap equation to the leading order to determine the condensate ϕ_0 as wee will see in the succeeding section.

6.3 Gap equation

The condensate ϕ_0 as a function of the chemical potential μ is determined by the gap equation which is obtained by the condition of the disappearance of all tadpole diagrams. The leading contribution to the gap equation is the one-loop diagram drawn in Fig. 6.2(c), which is given by

$$\bar{\Xi}_1 = \bar{g} \int \frac{dk}{(2\pi)^{d+1}} G_{21}(k) = i\bar{g} \int \frac{d\boldsymbol{k}}{(2\pi)^d} \frac{\phi_0}{2\bar{E}_{\boldsymbol{p}}}. \tag{6.15}$$

By changing the integration variable to $z = \varepsilon_{\boldsymbol{p}}/\mu$, we obtain

$$\bar{\Xi}_1 = \frac{i\bar{g}\phi_0}{2\mu} \frac{\left(\frac{m\mu}{2\pi}\right)^{\frac{d}{2}}}{\Gamma\left(\frac{d}{2}\right)} \int_0^\infty dz \, \frac{z^{\bar{\epsilon}/2}}{\sqrt{(z-1)^2 + (\phi_0/\mu)^2}}. \tag{6.16}$$

The integration over z in the dimensional regularization can be performed to lead to

$$\bar{\Xi}_1 = \frac{i\bar{g}\phi_0}{\mu} \frac{\left(\frac{m\mu}{2\pi}\right)^{\frac{d}{2}}}{\Gamma\left(\frac{d}{2}\right)} \left[\ln \frac{2\mu}{\phi_0} - \frac{1}{\bar{\epsilon}} + O(\bar{\epsilon}^2) \right]. \tag{6.17}$$

The first term $\ln 2\mu/\phi_0$ originates from the singularity around the Fermi surface as is well known as the Cooper instability, while the second term $1/\bar{\epsilon}$ is from the logarithmic singularity of the $\boldsymbol{k}$ integration at $d = 2$ in $\bar{\Xi}_1$. Solving the gap equation $\bar{\Xi}_1 = 0$, we obtain the condensate as $\phi_0 = 2\mu\, e^{-1/\bar{\epsilon}}$. Note that this result is equivalent to that obtained by the mean field BCS theory.

It is known that the pre–exponential factor in the mean field result $\phi_0 = 2\mu\, e^{-1/\bar{\epsilon}}$ is modified due to the effects of medium [130, 131]. In the language of the tadpole diagrams, the corresponding modification to the gap equation comes from the three-loop diagram $\bar{\Xi}_3$ depicted in Fig. 6.3. The diagram, which seems proportional to $g^4 \sim \bar{\epsilon}^2$, gives the $O(1)$ correction to the gap equation.

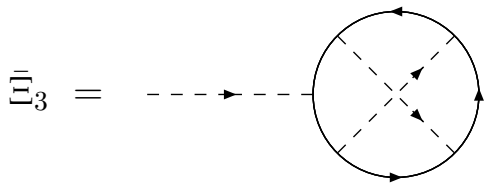

Figure 6.3: The tadpole diagram which gives the medium-effect correction to the gap equation.

Using the Feynman rules, the tadpole diagram in Fig. 6.3 is given by

$$\begin{aligned}\bar{\Xi}_3 &= -\bar{g}^5 \int \frac{dk\,dp\,dq}{(2\pi)^{3d+3}} \mathrm{Tr}\left[\bar{G}\sigma_+\bar{G}\sigma_-\bar{G}\sigma_+\bar{G}\sigma_+\bar{G}\sigma_-\right] \\ &= -\bar{g}^5 \int \frac{dk\,dp\,dq}{(2\pi)^{3d+3}} \bar{G}_{11}(p)\,\bar{G}_{22}(p)\,\bar{G}_{11}(p-k)\,\bar{G}_{21}(q)\,\bar{G}_{22}(q+k).\end{aligned} \tag{6.18}$$

Since the second term in the product,

$$\bar{G}_{11}(p)\,\bar{G}_{22}(p) = \frac{1}{p_0^2 - \bar{E}_{\boldsymbol{p}}^2} + \frac{\phi_0^2}{(p_0^2 - \bar{E}_{\boldsymbol{p}}^2)^2}, \tag{6.19}$$

gives only the $O(\bar{\epsilon}^2)$ correction to the gap equation, we can neglect it for the current purpose. Then we perform the integration over p_0 and q_0 to result in

$$\begin{aligned}\bar{\Xi}_3 = -\bar{g}^5 \int \frac{dk\,d\boldsymbol{p}\,d\boldsymbol{q}}{(2\pi)^{3d+1}} \frac{\phi_0}{4\bar{E}_{\boldsymbol{p}}\bar{E}_{\boldsymbol{q}}} &\left[\frac{\bar{E}_{\boldsymbol{p}} - k_0 + \varepsilon_{\boldsymbol{p}-\boldsymbol{k}} - \mu}{(\bar{E}_{\boldsymbol{p}} - k_0)^2 - \bar{E}_{\boldsymbol{p}-\boldsymbol{k}}^2} + \frac{\bar{E}_{\boldsymbol{p}} + \varepsilon_{\boldsymbol{p}} - \mu}{(k_0 + \bar{E}_{\boldsymbol{p}})^2 - \bar{E}_{\boldsymbol{p}+\boldsymbol{k}}^2}\right] \\ &\times \left[\frac{k_0 + \bar{E}_{\boldsymbol{q}} - \varepsilon_{\boldsymbol{q}+\boldsymbol{k}} + \mu}{(k_0 + \bar{E}_{\boldsymbol{q}})^2 - \bar{E}_{\boldsymbol{q}+\boldsymbol{k}}^2} + \frac{\bar{E}_{\boldsymbol{q}} - \varepsilon_{\boldsymbol{q}} + \mu}{(k_0 - \bar{E}_{\boldsymbol{q}})^2 - \bar{E}_{\boldsymbol{q}-\boldsymbol{k}}^2}\right].\end{aligned} \tag{6.20}$$

Because of the factor $1/\bar{E}_{\boldsymbol{p}}\bar{E}_{\boldsymbol{q}}$ in the integrand, the integrations over $\boldsymbol{p}$ and $\boldsymbol{q}$ are dominated around the Fermi surface where $\varepsilon_{\boldsymbol{p}(\boldsymbol{q})} \sim \mu$ and hence $\bar{E}_{\boldsymbol{p}(\boldsymbol{q})} \sim \phi_0$. Keeping only the dominant part in the integrand, we can write the integral as

$$\bar{\Xi}_3 \simeq \bar{g}^5 \int \frac{dk\,d\boldsymbol{p}\,d\boldsymbol{q}}{(2\pi)^{3d+1}} \frac{\phi_0}{4\bar{E}_{\boldsymbol{p}}\bar{E}_{\boldsymbol{q}}} \frac{1}{(k_0 + \varepsilon_{\boldsymbol{p}-\boldsymbol{k}} - \mu)(k_0 + \varepsilon_{\boldsymbol{q}+\boldsymbol{k}} - \mu)}\bigg|_{\varepsilon_{\boldsymbol{p}(\boldsymbol{q})}=\mu}. \tag{6.21}$$

Now the integration over k_0 can be performed easily to lead to

$$\bar{\Xi}_3 = -i\frac{\bar{g}^5}{2}\phi_0 \int \frac{d\boldsymbol{p}\,d\boldsymbol{q}}{(2\pi)^{2d}} \frac{1}{\bar{E}_{\boldsymbol{p}}\bar{E}_{\boldsymbol{q}}} \int \frac{d\boldsymbol{k}}{(2\pi)^d} \frac{\theta(\varepsilon_{\boldsymbol{q}+\boldsymbol{k}} - \mu)\,\theta(\mu - \varepsilon_{\boldsymbol{p}-\boldsymbol{k}})}{\varepsilon_{\boldsymbol{q}+\boldsymbol{k}} - \varepsilon_{\boldsymbol{p}-\boldsymbol{k}}}\bigg|_{\varepsilon_{\boldsymbol{p}(\boldsymbol{q})}=\mu}. \tag{6.22}$$

If we evaluated the $\boldsymbol{k}$ integration at $d = 3$, we would obtain the static Lindhard function representing the medium-induced interaction [21].

Here we shall evaluate $\bar{\Xi}_3$ at $d = 2$. Changing the integration variables to $\varepsilon_{\boldsymbol{p}}$, $\varepsilon_{\boldsymbol{q}}$, $\varepsilon_{\boldsymbol{k}}$, $\cos\chi_p = \hat{\boldsymbol{k}}\cdot\hat{\boldsymbol{p}}$, $\cos\chi_q = \hat{\boldsymbol{k}}\cdot\hat{\boldsymbol{q}}$, and performing the integrations over $\varepsilon_{\boldsymbol{p}}$ and $\varepsilon_{\boldsymbol{q}}$, we obtain

$$\bar{\Xi}_3 \simeq -i\frac{\bar{g}^5}{2}\phi_0 \left(\frac{m}{2\pi}\right)^3 \left(2\ln\frac{\mu}{\phi_0}\right)^2 \int \frac{d\varepsilon_{\boldsymbol{k}}\,d\chi_p\,d\chi_q}{\pi^2} \frac{\theta(\varepsilon_{\boldsymbol{q}+\boldsymbol{k}} - \mu)\,\theta(\mu - \varepsilon_{\boldsymbol{p}-\boldsymbol{k}})}{\varepsilon_{\boldsymbol{q}+\boldsymbol{k}} - \varepsilon_{\boldsymbol{p}-\boldsymbol{k}}}\bigg|_{\varepsilon_{\boldsymbol{p}(\boldsymbol{q})}=\mu}. \tag{6.23}$$

The range of the integrations over χ_p and χ_q are from 0 to π. Since $\phi_0/\mu \propto e^{-1/\bar{\epsilon}}$, we have $(2\ln\mu/\phi_0)^2 \sim (2/\bar{\epsilon})^2$ which cancels $\bar{\epsilon}^2$ coming from the four vertex couplings $\bar{g}^4$. Finally the integrations can be performed as follows:

$$\begin{aligned}
&\int \frac{d\varepsilon_{\boldsymbol{k}}\, d\chi_p\, d\chi_q}{\pi^2}\, \frac{\theta(\varepsilon_{\boldsymbol{q}+\boldsymbol{k}}-\mu)\,\theta(\mu-\varepsilon_{\boldsymbol{p}-\boldsymbol{k}})}{\varepsilon_{\boldsymbol{q}+\boldsymbol{k}}-\varepsilon_{\boldsymbol{p}-\boldsymbol{k}}} \\
&\quad = \int_0^{4\mu\cos^2\chi_p} d\varepsilon_{\boldsymbol{k}} \int_0^{\pi/2} \frac{d\chi_p}{\pi} \int_0^{\pi/2} \frac{d\chi_q}{\pi} \frac{1}{2\sqrt{\mu\varepsilon_{\boldsymbol{k}}}\left(\cos\chi_p+\cos\chi_q\right)} \\
&\qquad + \int_{4\mu\cos^2\chi_q}^{4\mu\cos^2\chi_p} d\varepsilon_{\boldsymbol{k}} \int_0^{\pi/2} \frac{d\chi_p}{\pi} \int_{\pi/2}^{\pi-\chi_p} \frac{d\chi_q}{\pi} \frac{1}{2\sqrt{\mu\varepsilon_{\boldsymbol{k}}}\left(\cos\chi_p+\cos\chi_q\right)} \\
&\quad = \frac{1}{2},
\end{aligned} \tag{6.24}$$

which gives $\bar{\Xi}_3$ as

$$\bar{\Xi}_3 \simeq -i\bar{g}\phi_0 \frac{m}{2\pi}. \tag{6.25}$$

Consequently, the gap equation $\bar{\Xi}_1 + \bar{\Xi}_3 = 0$, which receives the $O(1)$ correction due to $\bar{\Xi}_3$, is modified as

$$\ln\frac{2\mu}{\phi_0} - \frac{1}{\bar{\epsilon}} - 1 + O(\bar{\epsilon}) = 0. \tag{6.26}$$

The solution of the gap equation becomes

$$\phi_0 = 2\mu\, \exp\left[-\frac{1}{\bar{\epsilon}} - 1 + O(\bar{\epsilon})\right] = \frac{2\mu}{e}\,[1+O(\bar{\epsilon})]\, e^{-1/\bar{\epsilon}}, \tag{6.27}$$

where the value of condensate is reduced by the factor $e \approx 2.71828$. The reduction of the pre–exponential factor due to the medium effects is known as the Gor'kov correction at $d = 3$ theories [130, 131].

6.4 Thermodynamic quantities

The value of the effective potential $V_{\rm eff}$ at its minimum determines the pressure $P = -\bar{V}_{\rm eff}(\phi_0)$ at a given chemical potential μ. Since the energy gain due to the superfluidity $\phi_0^2 \sim e^{-2/\bar{\epsilon}}$ is exponentially small compared to any power series of $\bar{\epsilon}$, we can simply neglect the contributions of ϕ_0 to the pressure. To the next-to-leading order, the effective potential receives contribution from two vacuum diagrams drawn in Fig. 6.4: fermion loops without and with an exchange of the auxiliary field. The one-loop diagram at $\phi_0 = 0$ is $O(1)$ and given by

$$\bar{V}_1(0) = -2\int \frac{d\boldsymbol{p}}{(2\pi)^d}(\mu-\varepsilon_{\boldsymbol{p}})_> = -\frac{2\mu\left(\frac{m\mu}{2\pi}\right)^{\frac{d}{2}}}{\Gamma\left(\frac{d}{2}+2\right)} \equiv -P_{\rm free}, \tag{6.28}$$

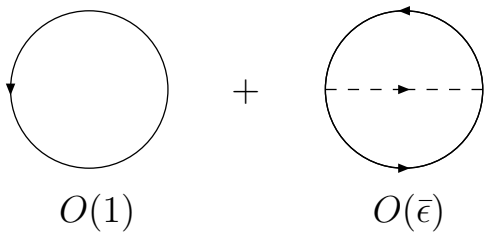

Figure 6.4: Vacuum diagrams contributing to the pressure up to next-to-leading order in $\bar{\epsilon}$.

which represents the contributions of free fermions to the pressure. The two-loop diagram at $\phi_0 = 0$ is $O(\bar{\epsilon})$, which represents the density-density correlation as

$$\begin{aligned}\bar{V}_2(0) &= -\bar{g}^2 \int \frac{dp\, dq}{(2\pi)^{2d+2}} \bar{G}_{11}(p)\bar{G}_{22}(q) \\ &= -\bar{g}^2 \left[\int \frac{d\boldsymbol{p}}{(2\pi)^d}\theta(\mu - \varepsilon_{\boldsymbol{p}})\right]^2 = -\epsilon \frac{\mu\left(\frac{m\mu}{2\pi}\right)^{\frac{d}{2}}}{\Gamma\left(\frac{d}{2}+1\right)^2}.\end{aligned} \tag{6.29}$$

Thus we obtain the pressure up to the next-to-leading order in $\bar{\epsilon}$ as

$$P = (1 + \bar{\epsilon})\, P_{\text{free}}. \tag{6.30}$$

Accordingly, the fermion number density is given by $N = \partial P/\partial\mu = (1 + \bar{\epsilon})\, N_{\text{free}}$. The Fermi energy is obtained from the thermodynamics of free gas in d spatial dimensions as

$$\varepsilon_{\text{F}} = \frac{2\pi}{m}\left[\frac{1}{2}\,\Gamma\left(\frac{d}{2}+1\right)N\right]^{2/d} = (1 + \bar{\epsilon})\,\mu, \tag{6.31}$$

which yields the universal parameter of the unitary Fermi gas from the $\bar{\epsilon}$ expansion as

$$\xi = \frac{\mu}{\varepsilon_{\text{F}}} = 1 - \bar{\epsilon} + O(\bar{\epsilon}^2). \tag{6.32}$$

6.5 Quasiparticle spectrum

To the leading order in $\bar{\epsilon}$, the dispersion relation of the fermion quasiparticle is given by $\omega_{\text{F}}(\boldsymbol{p}) = \bar{E}_{\boldsymbol{p}} = \sqrt{(\varepsilon_{\boldsymbol{p}} - \mu)^2 + \phi_0^2}$, which has the same form as that in the mean field BCS theory. There exist the next-to-leading order corrections to the fermion quasiparticle spectrum from the one-loop self-energy diagrams, $-i\bar{\Sigma}(p)$, depicted in Fig. 6.5. These corrections are only to the diagonal elements of the self-energy and each element is evaluated as

$$\begin{aligned}\bar{\Sigma}_{11}(p) &= -i\bar{g}^2 \int \frac{dk}{(2\pi)^{d+1}}\, \bar{G}_{22}(k) \\ &= -\bar{g}^2 \int \frac{d\boldsymbol{k}}{(2\pi)^d}\, \theta(\mu - \varepsilon_{\boldsymbol{k}}) = -\bar{\epsilon}\mu\end{aligned} \tag{6.33}$$

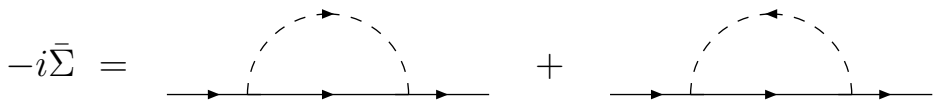

Figure 6.5: One-loop diagrams contributing to the fermion self-energy in order $O(\bar{\epsilon})$.

and

$$\begin{aligned}\bar{\Sigma}_{22}(p) &= -i\bar{g}^2 \int \frac{dk}{(2\pi)^{d+1}}\, \bar{G}_{11}(k) \\ &= \bar{g}^2 \int \frac{d\boldsymbol{k}}{(2\pi)^d}\, \theta(\mu - \varepsilon_{\boldsymbol{k}}) = \bar{\epsilon}\mu.\end{aligned} \tag{6.34}$$

To this order, the self-energy is momentum independent, which effectively shifts the chemical potential due to the interaction with the other component of fermions.

By solving the equation $\det[\bar{G}^{-1}(\omega, \boldsymbol{p}) - \bar{\Sigma}] = 0$ in terms of ω, the dispersion relation of the fermion quasiparticle up to the next-to-leading order is given by

$$\omega_{\rm F}(\boldsymbol{p}) = \sqrt{(\varepsilon_{\boldsymbol{p}} - \mu - \bar{\epsilon}\mu)^2 + \phi_0^2}. \tag{6.35}$$

The minimum of the dispersion curve is located at a nonzero value of momentum, $|\boldsymbol{p}| = (2m\varepsilon_0)^{1/2}$, where

$$\varepsilon_0 = (1 + \bar{\epsilon})\,\mu. \tag{6.36}$$

The location of the minimum coincides with the Fermi energy in Eq. (6.31), $\varepsilon_0 = \varepsilon_{\rm F}$, in agreement with the Luttinger theorem [132]. The energy gap Δ of the fermion quasiparticle is given by the condensate,

$$\Delta = \phi_0 = \frac{2\mu}{e}\, e^{-1/\bar{\epsilon}}. \tag{6.37}$$

6.6 Extrapolation to $\bar{\epsilon}$=1

Now we discuss the extrapolation of the expansion over $\bar{\epsilon} = d - 2$ to the physical case at three spatial dimensions. In contradiction to the case of $\epsilon = 4 - d$ expansion, the coefficients of $O(\bar{\epsilon})$ corrections are not small. If we naively extrapolate the leading and next-to-leading order results for ξ in Eq. (6.32), Δ in Eq. (6.37), and ε_0 in Eq. (6.36) to $\bar{\epsilon} = 1$, we would have

$$\xi \approx 0, \qquad \frac{\Delta}{\mu} \approx 0.271, \qquad \frac{\varepsilon_0}{\mu} \approx 2, \tag{6.38}$$

which are not as good as the extrapolations in the expansions over ϵ in Eq. (3.77). Thus, instead of naively extrapolating the $\bar{\epsilon}$ expansions to $d = 3$, we use them as boundary conditions to improve the series summation of the ϵ expansions in Chap. 7.

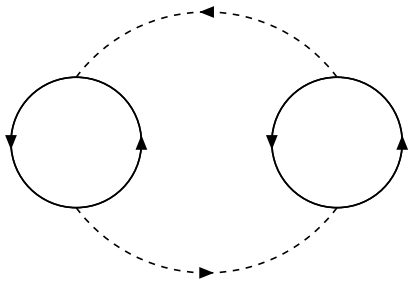

Figure 6.6: Vacuum diagram contributing to the pressure to the order $\bar{\epsilon}^2$. The counter vertex $-i\bar{\Pi}_0 = i$ for each bubble diagram is understood implicitly. The other $O(\bar{\epsilon}^2)$ diagrams identically vanish.

6.7 NNLO correction for ξ

The order $\bar{\epsilon}^2$ contribution to the effective potential or the pressure is solely given by the three-loop diagram depicted in Fig. 6.6, which is written as

$$\bar{V}_3(0) = \frac{i}{2}\int\frac{dk}{(2\pi)^{d+1}}\left[1+\bar{g}^2\int\frac{d\boldsymbol{p}}{(2\pi)^d}\frac{\theta(\varepsilon_{\boldsymbol{p}+\frac{\boldsymbol{k}}{2}}-\mu)-\theta(\mu-\varepsilon_{\boldsymbol{p}-\frac{\boldsymbol{k}}{2}})}{2\varepsilon_{\boldsymbol{p}}-(k_0-\frac{1}{2}\varepsilon_{\boldsymbol{k}}+2\mu+i\delta)}\right]^2. \tag{6.39}$$

where p_0 integrations in each bubble diagram are already performed. Note that +1 in the bracket comes from the counter vertex $-\bar{\Pi}_0 = 1$. We can see that the other $O(\bar{\epsilon}^2)$ diagrams identically vanish. The integration over k_0 in $\bar{V}_3$ leads to

$$\bar{V}_3(0) = -\bar{g}^2\int\frac{d\boldsymbol{k}d\boldsymbol{p}}{(2\pi)^{2d}}\,\theta(\mu-\varepsilon_{\boldsymbol{p}+\frac{\boldsymbol{k}}{2}})\theta(\mu-\varepsilon_{\boldsymbol{p}-\frac{\boldsymbol{k}}{2}})\left[1+\bar{g}^2\int\frac{d\boldsymbol{q}}{(2\pi)^d}\frac{\theta(\varepsilon_{\boldsymbol{q}+\frac{\boldsymbol{k}}{2}}-\mu)\theta(\varepsilon_{\boldsymbol{q}-\frac{\boldsymbol{k}}{2}}-\mu)}{2\varepsilon_{\boldsymbol{q}}-2\varepsilon_{\boldsymbol{p}}}\right]. \tag{6.40}$$

Due to the θ-functions, the range of integral over $\varepsilon_{\boldsymbol{k}}$ is limited to $0 \le \varepsilon_{\boldsymbol{k}} \le 4\mu$ and the range of integral over $\varepsilon_{\boldsymbol{p}}$ is limited to $0 \le \varepsilon_{\boldsymbol{p}} \le \Lambda_p$, where

$$\sqrt{\Lambda_p} = \frac{-|\cos\chi_p|\sqrt{\varepsilon_{\boldsymbol{k}}}+\sqrt{4\mu-\varepsilon_{\boldsymbol{k}}\sin^2\chi_p}}{2} \tag{6.41}$$

with $\cos\chi_p = \hat{\boldsymbol{k}}\cdot\hat{\boldsymbol{p}}$. Similarly, the range of integral over $\varepsilon_{\boldsymbol{q}}$ is limited to $\Lambda_q \le \varepsilon_{\boldsymbol{q}}$ where

$$\sqrt{\Lambda_q} = \frac{|\cos\chi_q|\sqrt{\varepsilon_{\boldsymbol{k}}}+\sqrt{4\mu-\varepsilon_{\boldsymbol{k}}\sin^2\chi_q}}{2} \tag{6.42}$$

with $\cos\chi_q = \hat{\boldsymbol{k}}\cdot\hat{\boldsymbol{q}}$. Then the integration over $\varepsilon_{\boldsymbol{q}}$ is performed to result in

$$\bar{V}_3(0) = \bar{\epsilon}^2\frac{m}{4\pi}\int_0^{4\mu}d\varepsilon_{\boldsymbol{k}}\int_0^{\pi}\frac{d\chi_p}{\pi}\int_0^{\pi}\frac{d\chi_q}{\pi}\int_0^{\Lambda_p}d\varepsilon_{\boldsymbol{p}}\ln\left(\frac{\Lambda_q-\varepsilon_{\boldsymbol{p}}}{\mu}\right)+O(\bar{\epsilon}^3). \tag{6.43}$$

Finally, introducing the dimensionless variable $z = \varepsilon_{\boldsymbol{k}}/\mu$ and performing the integration over $\varepsilon_{\boldsymbol{p}}$, we obtain the following expression for V_3,

$$\bar{V}_3(0) = \bar{\epsilon}^2\frac{m\mu^2}{4\pi}\int_0^4 dz\int_0^{\pi}\frac{d\chi_p}{\pi}\int_0^{\pi}\frac{d\chi_q}{\pi}\left[\tilde{\Lambda}_q\ln\tilde{\Lambda}_q-(\tilde{\Lambda}_q-\tilde{\Lambda}_p)\ln(\tilde{\Lambda}_q-\tilde{\Lambda}_p)-\tilde{\Lambda}_p\right], \tag{6.44}$$

where $\tilde{\Lambda}_{p(q)} = \Lambda_{p(q)}/\mu$. The numerical integrations over z, χ_p, and χ_q give

$$\bar{V}_3(0) = \bar{\epsilon}^2 \frac{m\mu^2}{2\pi} \times 0.0568528. \tag{6.45}$$

Therefore, combining this result with Eqs. (6.28) and (6.29), we obtain the pressure up to the next-to-next-to-leading order (NNLO) in $\bar{\epsilon}$ as

$$P = P_{\text{free}} \left[1 + \bar{\epsilon} + \left(\frac{\gamma}{2} - \frac{1}{4} \right) \bar{\epsilon}^2 - 0.0568528\, \bar{\epsilon}^2 \right]. \tag{6.46}$$

Then ξ up to the order $\bar{\epsilon}^2$ is found to be given by

$$\xi = \frac{\mu}{\varepsilon_{\text{F}}} = \left[1 + \bar{\epsilon} + \left(\frac{\gamma}{2} - \frac{1}{4} \right) \bar{\epsilon}^2 - 0.0568528\, \bar{\epsilon}^2 \right]^{-\frac{2}{2+\bar{\epsilon}}} = 1 - \bar{\epsilon} + 1.51824\, \bar{\epsilon}^2 + O(\bar{\epsilon}^3). \tag{6.47}$$

Although the $O(\bar{\epsilon}^2)$ correction to the pressure is small, $(2\gamma - 1)/4 - 0.0569 = -0.0182$, the NNLO correction to ξ turns out to be large because of the large $O(\bar{\epsilon})$ correction in the pressure.

Chapter 7

Matching of expansions around $d = 4$ and $d = 2$

As we have mentioned previously, we shall match two expansions around $d = 4$ and $d = 2$, which are studied in Chapters 3 and 6 respectively, in order to extract results at $d = 3$. We use the results around two spatial dimensions as boundary conditions which should be satisfied by the series summations of the expansions over $\epsilon = 4 - d$. Because we do not yet have a precise knowledge on the large order behavior of the expansion around four spatial dimensions, we assume its Borel summability and employ Padé approximants.

Let us demonstrate the matching of two expansions by taking ξ as an example. In Ref. [96], the linear interpolation between exact values at $d = 2$ ($\xi = 1$) and $d = 4$ ($\xi = 0$) was discussed to yield $\xi = 0.5$ at $d = 3$. Now we have series expansions around these two exact limits. The expansion of ξ in terms of $\epsilon = 4 - d$ is obtained in Eq. (3.43). Assuming the Borel summability of the ϵ expansion, we write ξ as a function of ϵ in the form of the Borel transformation,

$$\xi(\epsilon) = \frac{\epsilon^{3/2}}{2} \exp\left(\frac{\epsilon \ln \epsilon}{8 - 2\epsilon}\right) \int_0^\infty dt\, e^{-t} B_\xi(\epsilon t), \tag{7.1}$$

where we factorized out the non-trivial dependence on ϵ explicitly. $B_\xi(t)$ is the Borel transform of the power series in $\xi(\epsilon)$, whose Taylor coefficients at origin is given from the ϵ expansion of ξ as

$$B_\xi(t) = 1 - \left(3C - \frac{5}{4}(1 - \ln 2)\right) t + \cdots . \tag{7.2}$$

In order to perform the integration over t in Eq. (7.1), the analytic continuation of the Borel transform $B_\xi(t)$ to the real positive axis of t is necessary. Here we employ the Padé approximant, where $B_\xi(t)$ is replaced by the following rational functions

$$B_\xi(t) = \frac{1 + p_1 t + \cdots + p_M t^M}{1 + q_1 t + \cdots + q_N t^N} . \tag{7.3}$$

From Eq. (7.2), we require that the Padé approximants satisfy $p_1 - q_1 = -3C + \frac{5}{4}(1 - \ln 2)$. Furthermore, we incorporate the results around two spatial dimensions in Eq. (6.32) by imposing

$$\xi(2 - \bar{\epsilon}) = 1 - \bar{\epsilon} + \cdots \tag{7.4}$$

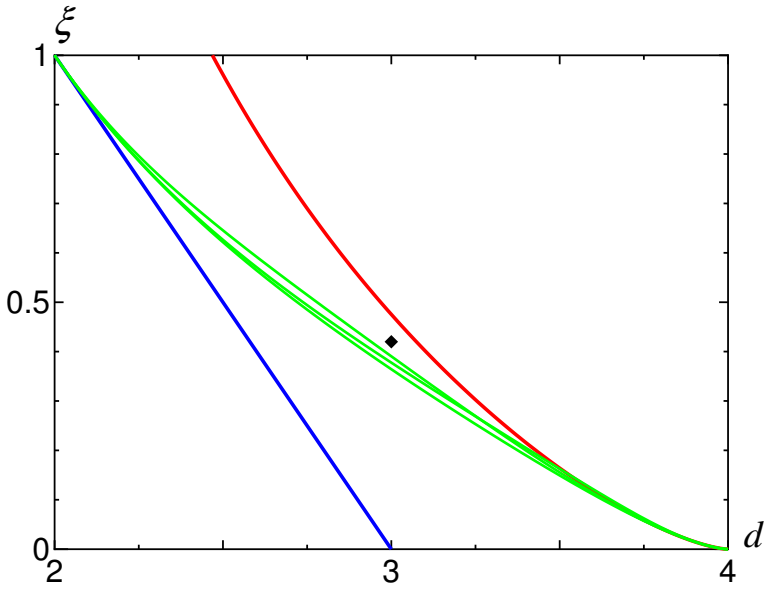

Figure 7.1: The universal parameter ξ as a function of the spatial dimensions d. The upper solid curve is from the expansion around $d = 4$ in Eq. (3.43), while the lower solid line is from the expansion around $d = 2$ in Eq. (6.32). The middle three curves show the different Borel–Padé approximants connecting the two expansions. The diamond indicates the result $\xi \approx 0.42$ from the Monte Carlo simulation [86].

on the Padé approximants as a boundary condition. Since we have three known coefficients from the two expansions, the Padé approximants $[M/N]$ satisfying $M + N = 3$ are possible. Since we could not find a solution satisfying the boundary condition $\xi(2 - \bar{\epsilon}) = 1 - \bar{\epsilon}$ for $[M/N] = [2/1]$, we adopt other three Padé approximants with $[M/N] = [3/0]$, $[1/2]$, $[0/3]$, whose coefficients p_m and q_n are determined uniquely by the above conditions.

Fig. 7.1 shows the universal parameter ξ as a function of the spatial dimensions d. The middle three curves show ξ in the different Padé approximants connecting the two expansions around $d = 4$ and $d = 2$. These Borel–Padé approximants give $\xi = 0.391$, 0.364, and 0.378 at $d = 3$, which are small compared to the naive extrapolation of the ϵ expansion to $d = 3$ ($\xi \to 0.475$).

The Padé approximant above, however, almost certainly needs serious modification, since it is known that in the expansion of $\xi(\epsilon)$, there exist non-analytic terms at sufficiently higher orders [102],

$$\xi(\epsilon) = \frac{\epsilon^{3/2}}{2} \exp\left[\frac{\epsilon \ln \epsilon}{8 - 2\epsilon}\right]\left(1 - 0.0492\epsilon + \#\epsilon^2 + \#\epsilon^3 \ln \epsilon + \cdots\right). \tag{7.5}$$

An understanding of the structure of high-order terms in the perturbation theory around $d = 4$ is currently lacking.

Chapter 8

Thermodynamics below T_{c}

Now we investigate the thermodynamics of the Fermi gas at finite temperature near the unitarity limit. At zero temperature, we found that there exist two difference energy scales in the system; the scale of condensate ϕ_0 and that of chemical potential $\mu \sim \epsilon\phi_0 \ll \phi_0$. Accordingly, we can consider two temperature regions where the unitary Fermi gas exhibits different thermodynamics.

One is the low temperature region where $T \sim \epsilon\phi_0$. In this region, the energy gap of the fermion quasiparticle $\Delta \sim \phi_0$ is still large compared to the temperature. Therefore, thermal excitations of the fermion quasiparticle are exponentially suppressed by a factor $e^{-\Delta/T} \sim e^{-1/\epsilon}$. The thermodynamics in this region is dominated by the bosonic phonon excitations. The other temperature region is the high temperature region where $T \sim \phi_0$. (ϕ_0 represents the condensate at zero temperature.) In this region, the condensate decreases and eventually vanishes at the critical temperature T_{c}. Fermions and bosons are equally excited here. We defer our discussion on the high temperature region to Chap. 9 and concentrate on the thermodynamics at the low temperature region $T \ll T_{\mathrm{c}}$ in this Chapter.

8.1 Finite temperature formalism

The extension to finite temperature T follows from the prescription of the imaginary time formalism. The system under consideration is described by the following Lagrangian density with the imaginary time $0 \le \tau \le 1/T$:

$$\mathcal{L}_0 = \Psi^\dagger \left(\partial_\tau - \frac{\sigma_3 \boldsymbol{\nabla}^2}{2m} - \sigma_+ \phi_0 - \sigma_- \phi_0 \right) \Psi + \varphi^* \left(\partial_\tau - \frac{\boldsymbol{\nabla}^2}{4m} \right) \varphi + \frac{\phi_0^2}{c_0}\,, \tag{8.1}$$

$$\mathcal{L}_1 = -g\Psi^\dagger \sigma_+ \Psi \varphi - g\Psi^\dagger \sigma_- \Psi \varphi^* - \mu \Psi^\dagger \sigma_3 \Psi - \left(2\mu - \frac{g^2}{c_0} \right) \varphi^* \varphi + \frac{g\phi_0}{c_0} \varphi + \frac{g\phi_0}{c_0} \varphi^*\,, \tag{8.2}$$

$$\mathcal{L}_2 = -\varphi^* \left(\partial_\tau - \frac{\boldsymbol{\nabla}^2}{4m} \right) \varphi + 2\mu \varphi^* \varphi\,. \tag{8.3}$$

The propagators of fermion and boson are generated by $\mathcal{L}_0$. The fermion propagator is a 2×2 matrix,

$$G(i\omega_n, \boldsymbol{p}) = \frac{1}{(i\omega_n)^2 - E_{\boldsymbol{p}}^2} \begin{pmatrix} i\omega_n + \varepsilon_{\boldsymbol{p}} & -\phi_0 \\ -\phi_0 & i\omega_n - \varepsilon_{\boldsymbol{p}} \end{pmatrix}, \tag{8.4}$$

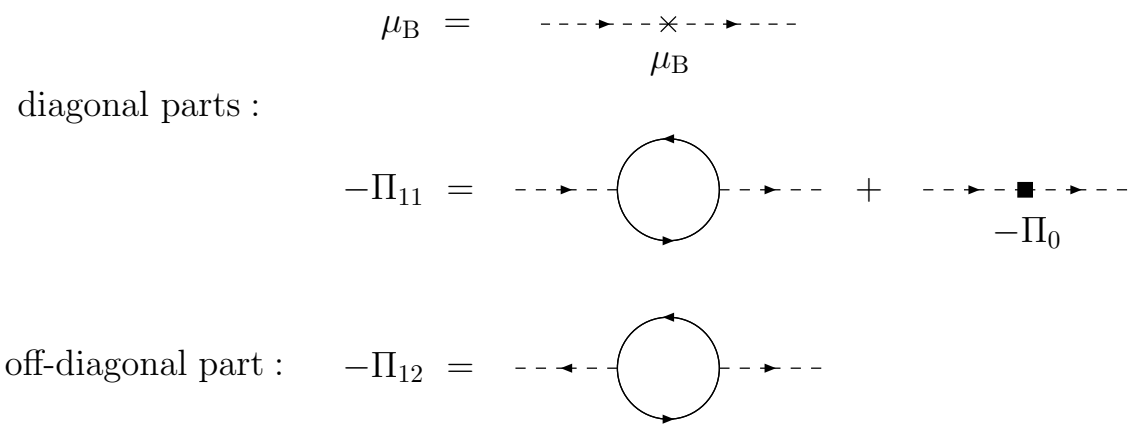

Figure 8.1: Boson's self-energies contributing to the order $O(\epsilon)$. Solid (dotted) lines represent the fermion (boson) propagator $-G$ ($-D$), while the cross in the first diagram represents the μ_B insertion to the boson propagator. The vertex Π_0 from $\mathcal{L}_2$ needs to be added to the second diagram. The last diagram gives the off-diagonal part of the self-energy.

where $\varepsilon_{\boldsymbol{p}} = \boldsymbol{p}^2/2m$, $E_{\boldsymbol{p}} = \sqrt{\varepsilon_{\boldsymbol{p}}^2 + \phi_0^2}$ and ϕ_0 is the condensate in the superfluid ground state as before. The boson propagator D is

$$D(i\nu_n, \boldsymbol{p}) = \left(i\nu_n - \frac{\varepsilon_{\boldsymbol{p}}}{2}\right)^{-1}. \tag{8.5}$$

$\omega_n = 2\pi T(n + \frac{1}{2})$ and $\nu_n = 2\pi T n$ are discrete Matsubara frequencies for fermion and boson with an integer $n = 0, \pm 1, \pm 2, \cdots$. The unitary Fermi gas around four spatial dimensions is described by the weakly-interacting system of fermionic and bosonic quasiparticles, whose coupling $g \sim \epsilon^{1/2}$ in $\mathcal{L}_1$ was introduced in Eq. (3.3) as

$$g = \frac{(8\pi^2\epsilon)^{1/2}}{m}\left(\frac{m\phi_0}{2\pi}\right)^{\epsilon/4}. \tag{8.6}$$

We define the counter vertex in $\mathcal{L}_2$ for the boson propagator by $\Pi_0(p_0, \boldsymbol{p}) = p_0 - \varepsilon_{\boldsymbol{p}}/2$ and the boson chemical potential by $\mu_B = 2\mu - g^2/c_0$. When c_0 is negative, $-g^2/c_0 \simeq \varepsilon_b$ gives the binding energy of boson to the leading order in ϵ. We consider the vicinity of the unitary point where $\varepsilon_b \sim \epsilon\phi_0$.

The power counting rule of ϵ developed at zero temperature in Sec. 3.2 holds in the low temperature region where the condensate is still large compared to the chemical potential $\mu/\phi_0 \sim \epsilon$, while it breaks down near the critical temperature because $\phi_0 \to 0$ at $T \to T_c$. In the high temperature region $T \sim T_c$, a minor modification of the power counting rule is necessary as we discuss in Chap. 9.

8.2 Phonon spectrum

The thermodynamics at the low temperature region $T \ll \phi_0$ is dominated by the phonon excitations. In order to determine the phonon spectrum, we first study the boson self-energy at zero temperature. To the order of $O(\epsilon)$, there are three types of contributions to the boson self-energy as depicted in

Fig. 8.1. In addition to the chemical potential insertion $\mu_{\rm B} = 2\mu + \varepsilon_{\rm b}$, the one-loop diagrams contribute to the diagonal part Π_{11} and off-diagonal part Π_{12} of the boson self-energy. The vertex Π_0 from $\mathcal{L}_2$ is necessary for Π_{11} according to the power counting rule described in Sec. 3.2. Then the diagonal part of the boson self-energy is given by

$$\Pi_{11}(p) = \Pi_0(p) + \Pi_{\rm a}(p), \tag{8.7}$$

where Π_0 is defined in Eq. (3.10) and $\Pi_{\rm a}$ is given by

$$\begin{aligned} -\Pi_{\rm a}(p) &= g^2 \int \frac{idk_0\,dk}{(2\pi)^{d+1}} G_{11}\Big(k+\frac{p}{2}\Big) G_{22}\Big(k-\frac{p}{2}\Big) \\ &= g^2 \int \frac{d\boldsymbol{k}}{(2\pi)^d} \frac{1}{4E_{\boldsymbol{k}-\frac{\boldsymbol{p}}{2}} E_{\boldsymbol{k}+\frac{\boldsymbol{p}}{2}}} \\ &\quad \times \left[\frac{(E_{\boldsymbol{k}-\frac{\boldsymbol{p}}{2}} + \varepsilon_{\boldsymbol{k}-\frac{\boldsymbol{p}}{2}})(E_{\boldsymbol{k}+\frac{\boldsymbol{p}}{2}} + \varepsilon_{\boldsymbol{k}+\frac{\boldsymbol{p}}{2}})}{E_{\boldsymbol{k}-\frac{\boldsymbol{p}}{2}} + E_{\boldsymbol{k}+\frac{\boldsymbol{p}}{2}} - p_0} + \frac{(E_{\boldsymbol{k}-\frac{\boldsymbol{p}}{2}} - \varepsilon_{\boldsymbol{k}-\frac{\boldsymbol{p}}{2}})(E_{\boldsymbol{k}+\frac{\boldsymbol{p}}{2}} - \varepsilon_{\boldsymbol{k}+\frac{\boldsymbol{p}}{2}})}{E_{\boldsymbol{k}-\frac{\boldsymbol{p}}{2}} + E_{\boldsymbol{k}+\frac{\boldsymbol{p}}{2}} + p_0} \right]. \end{aligned} \tag{8.8}$$

Since we are interested in physics at the scale of temperature $T \ll \phi_0$, it is sufficient to evaluate the self-energy when the external momentum is small $p \sim T \ll \phi_0$. Expanding $\Pi_{11}(p)$ in terms of p/ϕ_0 and performing the $\boldsymbol{k}$ integration with the use of the formula

$$\int_0^\infty dz\, \frac{z^{\alpha-1}}{(z+1)^\beta} = \frac{\Gamma(\alpha)\Gamma(\beta-\alpha)}{\Gamma(\beta)}, \tag{8.9}$$

we obtain

$$\Pi_{11}(p) \simeq -g^2 \int \frac{d\boldsymbol{k}}{(2\pi)^d} \frac{E_{\boldsymbol{k}}^2 + \varepsilon_{\boldsymbol{k}}^2}{4E_{\boldsymbol{k}}^3} = \frac{3}{2}\epsilon\phi_0 + O(\epsilon^2). \tag{8.10}$$

Similarly, the off-diagonal part of the boson-self energy is given by

$$\begin{aligned} -\Pi_{12}(p) &= g^2 \int \frac{idk_0\,dk}{(2\pi)^{d+1}} G_{12}\Big(k+\frac{p}{2}\Big) G_{12}\Big(k-\frac{p}{2}\Big) \\ &= -g^2 \int \frac{d\boldsymbol{k}}{(2\pi)^d} \frac{\phi_0^2}{4E_{\boldsymbol{k}-\frac{\boldsymbol{p}}{2}} E_{\boldsymbol{k}+\frac{\boldsymbol{p}}{2}}} \left[\frac{1}{E_{\boldsymbol{k}-\frac{\boldsymbol{p}}{2}} + E_{\boldsymbol{k}+\frac{\boldsymbol{p}}{2}} - p_0} + \frac{1}{E_{\boldsymbol{k}-\frac{\boldsymbol{p}}{2}} + E_{\boldsymbol{k}+\frac{\boldsymbol{p}}{2}} + p_0} \right]. \end{aligned} \tag{8.11}$$

Expanding $\Pi_{12}(p)$ in terms of p/ϕ_0 and performing the integration over $\boldsymbol{k}$, we obtain

$$\Pi_{12}(p) \simeq g^2 \int \frac{d\boldsymbol{k}}{(2\pi)^d} \frac{\phi^2}{4E_{\boldsymbol{k}}^3} = \frac{1}{2}\epsilon\phi_0 + O(\epsilon^2). \tag{8.12}$$

As a result of the resummation of these self-energies, the resumed boson propagator $\mathcal{D}$ is expressed by the following 2×2 matrix:

$$\mathcal{D}(p_0, \boldsymbol{p}) = \begin{pmatrix} D(p)^{-1} + \mu_{\rm B} - \Pi_{11} & -\Pi_{12} \\ -\Pi_{21} & D(-p)^{-1} + \mu_{\rm B} - \Pi_{22} \end{pmatrix}^{-1}, \tag{8.13}$$

where $\Pi_{22} = \Pi_{11}$ and $\Pi_{12} = \Pi_{21}$. The dispersion relation of the boson $\omega_{\rm ph}(\boldsymbol{p})$ can be obtained by solving the equation $\det[D^{-1}(\omega, \boldsymbol{p})] = 0$ in terms of ω as

$$\omega_{\rm ph}(\boldsymbol{p}) = \sqrt{\Big(\frac{\varepsilon_{\boldsymbol{p}}}{2} - \mu_{\rm B} + \epsilon\phi_0\Big)\Big(\frac{\varepsilon_{\boldsymbol{p}}}{2} - \mu_{\rm B} + 2\epsilon\phi_0\Big)}. \tag{8.14}$$

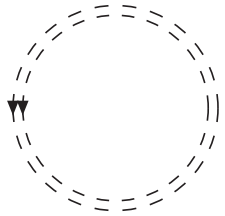

Figure 8.2: One-loop diagram of boson contributing the effective potential at finite temperature. The dotted double line represents the resumed boson propagator $\mathcal{D}$ in Eq. (8.13).

Note that this expression is valid as long as $\varepsilon_{\boldsymbol{p}} \ll \phi_0$ because of the expansions made to evaluate the boson self-energies. Substituting the leading order solution of the gap equation at zero temperature in Eq. (3.38), $\mu_B = \epsilon\phi_0$, the phonon spectrum is determined to be

$$\omega_{\rm ph}(\boldsymbol{p}) = \sqrt{\frac{\varepsilon_{\boldsymbol{p}}}{2}\left(\frac{\varepsilon_{\boldsymbol{p}}}{2} + \epsilon\phi_0\right)}. \tag{8.15}$$

For the small momentum $\varepsilon_{\boldsymbol{p}} \ll \epsilon\phi_0$, the dispersion relation becomes linear in the momentum as $\omega_{\rm ph} \simeq c_s|\boldsymbol{p}|$, remaining gapless in accordance with the Nambu–Goldstone theorem. The sound velocity of phonon c_s is given by

$$c_s = \sqrt{\frac{\epsilon\phi_0}{4m}} \sim \epsilon^{1/2}. \tag{8.16}$$

For the large momentum $\varepsilon_{\boldsymbol{p}} \gg \epsilon\phi_0$, the dispersion relation approaches that of the free boson as $\omega_{\rm ph} \simeq \varepsilon_{\boldsymbol{p}}/2$.

8.3 Effective potential and condensate

At finite temperature, the phonon excitations contribute to the effective potential, and consequently, the magnitude of the condensate decreases. The temperature dependent part of the effective potential $V_T(\phi_0)$ to the lowest order in ϵ is given by the one-loop diagram of the boson with the resumed propagator in Eq. (8.13) [Fig. 8.2]:

$$\begin{aligned} V_T(\phi_0) &= \frac{T}{2}\sum_n \int \frac{d\boldsymbol{p}}{(2\pi)^4}\,\mathrm{Tr}\ln\left[\mathcal{D}(i\nu_n,\boldsymbol{p})^{-1}\right] \\ &= \int \frac{d\boldsymbol{p}}{(2\pi)^4}\,T\ln\left[1 - e^{-\omega_{\rm ph}(\boldsymbol{p})/T}\right]. \end{aligned} \tag{8.17}$$

The n-th interaction vertex among phonons φ^n is of the order $\epsilon^{n/2}$ and appears in the effective potential only at higher orders. Then the contribution of $V_T(\phi_0)$ to the gap equation is

$$\frac{\partial V_T(\phi_0)}{\partial\phi_0} = \int \frac{d\boldsymbol{p}}{(2\pi)^4}\, f_B(\omega_{\rm ph})\,\frac{\partial\omega_{\rm ph}}{\partial\phi_0}, \tag{8.18}$$

where $f_{\rm B}(x) = 1/(e^{x/T} - 1)$ is the Bose distribution function and $\partial\omega_{\rm ph}/\partial\phi_0$ is given from Eq. (8.14) by

$$\frac{\partial\omega_{\rm ph}}{\partial\phi_0} = \epsilon\frac{3\varepsilon_{\boldsymbol{p}} + 2\epsilon\phi_0}{4\omega_{\rm ph}}. \tag{8.19}$$

There are two limiting cases where the integration over $\boldsymbol{p}$ in Eq. (8.18) can be analytically performed. Since the integral is dominated by the integration region where $\varepsilon_{\boldsymbol{p}} \sim T$, we can approximate the phonon spectrum by its linear branch $\omega_{\rm ph}(\boldsymbol{p}) \simeq c_{\rm s}|\boldsymbol{p}|$ when the temperature is very low $T \ll \epsilon\phi_0$. In this case, the integration over $\boldsymbol{p}$ in Eq. (8.18) leads to

$$\frac{\partial V_T(\phi_0)}{\partial\phi_0} \simeq \frac{8\zeta(3)T}{\phi_0}\left(\frac{mT}{2\pi}\right)^2. \tag{8.20}$$

On the other hand, when the temperature is located in the intermediate region $\epsilon\phi_0 \ll T \ll \phi_0$, the phonon spectrum can be approximated by its quadratic branch $\omega_{\rm ph} \simeq \varepsilon_{\boldsymbol{p}}/2$. In this case, the integration over $\boldsymbol{p}$ in Eq. (8.18) results in

$$\frac{\partial V_T(\phi_0)}{\partial\phi_0} \simeq \epsilon\frac{(mT)^2}{4}. \tag{8.21}$$

Now, from the gap equation $\partial(V_{\rm eff}(\phi) + V_T(\phi))/\partial\phi = 0$ with $\phi \equiv \phi_0 + \phi_T$, one finds the temperature dependent correction of the condensate ϕ_T satisfies

$$\frac{\partial V_{\rm eff}(\phi_0)^2}{\partial\phi_0^2}\phi_T + \frac{\partial V_T(\phi_0)}{\partial\phi_0} = 0, \tag{8.22}$$

where $V_{\rm eff}$ is the effective potential at zero temperature in Eq. (3.36). To the leading order in ϵ, ϕ_T at $T \ll \epsilon\phi_0$ is given by

$$\phi_T = -\frac{8\zeta(3)T^3}{\phi_0^2}, \tag{8.23}$$

while at $\epsilon\phi_0 \ll T \ll \phi_0$,

$$\phi_T = -\epsilon\frac{\pi^2T^2}{\phi_0}. \tag{8.24}$$

The condensate in total is $\phi = \phi_0 + \phi_T$, which decreases as the temperature increases. Note that since $\phi_T \ll \epsilon\phi_0$, the leading part of the condensate does not change in the temperature region considered here $T \ll \phi_0$. The effective potential is given by the sum of the zero temperature and finite temperature parts; $V_{\rm eff}(\phi_0 + \phi_T) + V_T(\phi_0 + \phi_T) \simeq V_{\rm eff}(\phi_0) + V_T(\phi_0)$.

8.4 Thermodynamic functions at low temperature

The temperature dependent part of the pressure $P_{\rm ph}$ at the low temperature region $T \ll \phi_0$ is given from the effective potential in Eq. (8.17) by

$$P_{\rm ph} = -V_T(\phi_0) = -\int\frac{d\boldsymbol{p}}{(2\pi)^4}\,T\ln\left[1 - e^{-\omega_{\rm ph}(\boldsymbol{p})/T}\right]. \tag{8.25}$$

The phonon contributions to the fermion number density, the entropy density, and the energy density are computed from the thermodynamic relations, $N_{\rm ph} = \partial P_{\rm ph}/\partial\mu$, $S_{\rm ph} = \partial P_{\rm ph}/\partial T$, and $E_{\rm ph} = \mu N_{\rm ph} + TS_{\rm ph} - P_{\rm ph}$, respectively. Here we show analytic expressions for these thermodynamic functions in the two cases where the analytic evaluation of the $\boldsymbol{p}$ integration in Eq. (8.25) is available.

When the temperature is very low $T \ll \epsilon\phi_0$, only the linear branch of the phonon spectrum $\omega_{\rm ph}(\boldsymbol{p}) \simeq c_{\rm s}|\boldsymbol{p}|$ is important to the thermodynamic functions. In this case, the integration over $\boldsymbol{p}$ can be performed analytically to lead to

$$P_{\rm ph} \simeq \frac{12\pi^2\zeta(5)}{(2\pi)^4}\frac{T^5}{c_{\rm s}^4} = \frac{12\zeta(5)}{\pi^2}\frac{m^2T^5}{(\epsilon\phi_0)^2}. \tag{8.26}$$

Accordingly, we obtain the phonon contributions to the fermion number density, the entropy density, and the energy density;

$$N_{\rm ph} = -\frac{48\zeta(5)}{\pi^2}\frac{m^2T^5}{(\epsilon\phi_0)^3}, \tag{8.27}$$

$$S_{\rm ph} = \frac{60\zeta(5)}{\pi^2}\frac{m^2T^4}{(\epsilon\phi_0)^2}, \tag{8.28}$$

$$E_{\rm ph} = \frac{24\zeta(5)}{\pi^2}\frac{m^2T^5}{(\epsilon\phi_0)^2}\left(1 + \frac{\varepsilon_{\rm b}}{\epsilon\phi_0}\right). \tag{8.29}$$

Since actual experiments or simulations are performed with the fixed fermion density, it is useful to show the thermodynamic functions at fixed N instead of fixed μ. From Eqs. (3.38), (3.40), and (8.27), we find the chemical potential for the fixed fermion density increases as a function of the temperature as

$$\mu = \mu_0 + 48\zeta(5)\frac{T^5}{\epsilon\phi_0^4}, \tag{8.30}$$

where μ_0 represents the chemical potential at zero temperature in Eq. (3.42). Normalizing μ by the Fermi energy in Eq. (3.41), we have

$$\frac{\mu}{\varepsilon_{\rm F}} = \frac{\mu_0}{\varepsilon_{\rm F}} + \frac{3\zeta(5)}{2\epsilon^3}\left(\frac{2T}{\varepsilon_{\rm F}}\right)^5. \tag{8.31}$$

The other thermodynamic functions for the fixed fermion number density are given by

$$\frac{P}{\varepsilon_{\rm F}N} = \frac{P_0}{\varepsilon_{\rm F}N} + \frac{3\zeta(5)}{\epsilon^3}\left(\frac{2T}{\varepsilon_{\rm F}}\right)^5, \tag{8.32}$$

$$\frac{E}{\varepsilon_{\rm F}N} = \frac{E_0}{\varepsilon_{\rm F}N} + \frac{6\zeta(5)}{\epsilon^3}\left(\frac{2T}{\varepsilon_{\rm F}}\right)^5, \tag{8.33}$$

$$\frac{S}{N} = \frac{15\zeta(5)}{\epsilon^3}\left(\frac{2T}{\varepsilon_{\rm F}}\right)^4, \tag{8.34}$$

where P_0 and E_0 represent the pressure and energy density at zero temperature in Eqs. (3.44) and (3.45), respectively. These expressions are valid in the low temperature region where $T \ll \epsilon\phi_0$.

On the other hand, when the temperature is located in the intermediate region $\epsilon\phi_0 \ll T \ll \phi_0$, we can expand the phonon spectrum $\omega_{\rm ph}(\boldsymbol{p})$ in terms of $\epsilon\phi_0/\varepsilon_{\boldsymbol{p}}$ up to its first order

$$\omega_{\rm ph}(\boldsymbol{p}) \simeq \frac{\varepsilon_{\boldsymbol{p}}}{2} + \frac{\epsilon\phi_0}{2}. \tag{8.35}$$

In this case, the integration over $\boldsymbol{p}$ can be performed analytically again to result in

$$P_{\rm ph} \simeq \frac{\zeta(3)}{\pi^2} m^2 T^3 - \frac{m^2 T^2}{12}\epsilon\phi_0. \tag{8.36}$$

Accordingly, we obtain the temperature dependent parts of the fermion number density, the entropy density, and the energy density;

$$N_{\rm ph} = -\frac{m^2 T^2}{6}, \tag{8.37}$$

$$S_{\rm ph} = \frac{3\zeta(3)}{\pi^2} m^2 T^2 - \frac{m^2 T}{6}\epsilon\phi_0, \tag{8.38}$$

$$E_{\rm ph} = \frac{2\zeta(3)}{\pi^2} m^2 T^3 - \frac{m^2 T^2}{6}\epsilon\phi_0\left(1 - \frac{\varepsilon_{\rm b}}{2\epsilon\phi_0}\right). \tag{8.39}$$

From Eqs. (3.38), (3.40), and (8.37), we find the chemical potential for the fixed fermion density increases as a function of the temperature as

$$\mu = \mu_0 + \epsilon^2 \frac{\pi^2}{6}\frac{T^2}{\phi_0}. \tag{8.40}$$

Normalizing μ by the Fermi energy in Eq. (3.41), we have

$$\frac{\mu}{\varepsilon_{\rm F}} = \frac{\mu_0}{\varepsilon_{\rm F}} + \epsilon^{3/2}\frac{\pi^2}{6}\left(\frac{T}{\varepsilon_{\rm F}}\right)^2. \tag{8.41}$$

The other thermodynamic functions for the fixed fermion number density are given by

$$\frac{P}{\varepsilon_{\rm F} N} = \frac{P_0}{\varepsilon_{\rm F} N} + 4\zeta(3)\left(\frac{T}{\varepsilon_{\rm F}}\right)^3 - \epsilon^{3/2}\frac{\pi^2}{6}\left(\frac{T}{\varepsilon_{\rm F}}\right)^2, \tag{8.42}$$

$$\frac{E}{\varepsilon_{\rm F} N} = \frac{E_0}{\varepsilon_{\rm F} N} + 8\zeta(3)\left(\frac{T}{\varepsilon_{\rm F}}\right)^3 - \epsilon^{3/2}\frac{\pi^2}{3}\left(\frac{T}{\varepsilon_{\rm F}}\right)^2, \tag{8.43}$$

$$\frac{S}{N} = 12\zeta(3)\left(\frac{T}{\varepsilon_{\rm F}}\right)^2 - \epsilon^{3/2}\frac{2\pi^2}{3}\frac{T}{\varepsilon_{\rm F}}. \tag{8.44}$$

These expressions are valid in the intermediate temperature region where $\epsilon\phi_0 \ll T \ll \phi_0$.

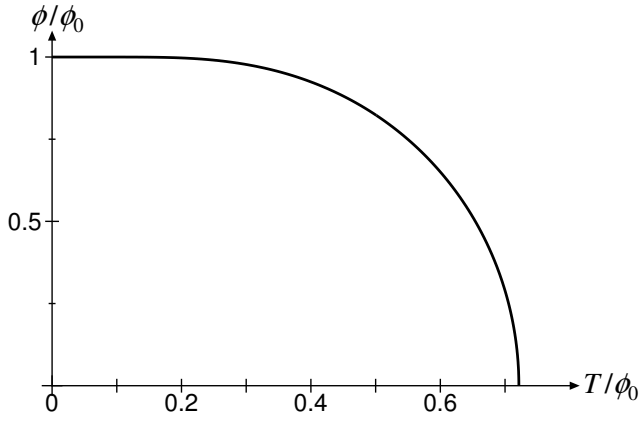

Figure 8.3: The behavior of the condensate ϕ as a function of the temperature T to the lowest order in ϵ. $\phi_0 = \mu_B/\epsilon$ is the value of the condensate at $T = 0$ and the critical temperature is located at $T_c/\phi_0 = 1/(2\ln 2) \approx 0.721348$.

8.5 Effective potential near T_c

At the end of this Chapter, we study the behavior of the condensate ϕ as a function of the temperature for a given μ. The effective potential to the leading order in ϵ is given by one-loop diagrams of fermion with and without one μ insertion, which is equivalent to the mean-field approximation. Since the critical dimension of the superfluid-normal phase transition is four, the mean-field approximation remains as a leading part at any temperature in the limit $d \to 4$. Then the leading contribution to the effective potential at finite temperature is given by

$$V_{\rm eff}(\phi) = -\frac{\varepsilon_b}{g^2}\phi^2 - \int \frac{d\boldsymbol{p}}{(2\pi)^d}\left[E_{\boldsymbol{p}} - \frac{\varepsilon_{\boldsymbol{p}}}{E_{\boldsymbol{p}}}\mu + 2T\ln\left(1 + e^{-E_{\boldsymbol{p}}/T}\right) + f_F(E_{\boldsymbol{p}})\frac{2\varepsilon_{\boldsymbol{p}}}{E_{\boldsymbol{p}}}\mu\right],$$

where $f_F(x) = 1/(e^{x/T} + 1)$ is the Fermi distribution function.

For the low temperature $T \ll \phi$, we can neglect the exponentially small factor $e^{-E_{\boldsymbol{p}}/T} \ll 1$ and the integration over $\boldsymbol{p}$ reproduces the leading order effective potential at zero temperature in Eq. (3.36). In the opposite limit where $\phi \ll T$, we can expand $V_{\rm eff}$ in terms of ϕ/T to lead to

$$V_{\rm eff}(\phi) = V_{\rm eff}(0) + \left[T\ln 2 - \frac{\mu_B}{2\epsilon}\right]\left(\frac{m\phi}{2\pi}\right)^2 + \frac{\phi^2}{16T}\left(\frac{m\phi}{2\pi}\right)^2 + \cdots, \tag{8.45}$$

where $\mu_B = 2\mu + \varepsilon_b$. From the coefficient of the quadratic term in ϕ, we can read the critical temperature T_c to the leading order in ϵ as

$$T_c = \frac{\mu_B}{\epsilon\, 2\ln 2} + O(\epsilon), \tag{8.46}$$

and the value of the condensate ϕ just below T_c as

$$\phi^2 = 8T\,(T_c - T)\ln 2 + O(\epsilon). \tag{8.47}$$

The critical exponent of the condensate $\phi \sim (T_c - T)^{1/2}$ will be shifted if we include higher order corrections to the effective potential. The condensate ϕ in the intermediate range of the temperature

is obtained by solving the gap equation $\partial V_{\rm eff}/\partial\phi = 0$;

$$\phi - \frac{\mu_{\rm B}}{\epsilon} + \int d\varepsilon_{\boldsymbol{p}} \frac{2\varepsilon_{\boldsymbol{p}}}{E_{\boldsymbol{p}}} f_{\rm F}(E_{\boldsymbol{p}}) = 0. \tag{8.48}$$

The numerical solution of the gap equation as a function of T is shown in Fig. 8.3.

Chapter 9

Thermodynamics above $T_{\rm c}$

9.1 Power counting rule of ϵ near $T_{\rm c}$

In the ϵ expansion at the zero or low temperature region, the chemical potential is small compared to the condensate $\mu \sim \epsilon\phi_0$ and we made expansions in terms of $\mu/\phi_0 \sim \epsilon$ as well as the small coupling $g \sim \epsilon^{1/2}$. Near the critical temperature, the ratio μ/ϕ is no longer small because ϕ vanishes at $T = T_{\rm c}$, but $\mu/T_{\rm c}$ is $O(\epsilon)$ as it is clear from $T_{\rm c} = \mu_{\rm B}/(\epsilon\, 2\ln 2)$. Therefore, we can still treat the chemical potential as a small perturbation near $T_{\rm c}$ and the same power counting rule of ϵ described in Sec. 3.2 holds even above $T_{\rm c}$ just by replacing ϕ_0 with T. Hereafter we consider $T \sim T_{\rm c}$ to be $O(1)$.

9.2 Boson's thermal mass

First we study the self-energy of boson at $T \geq T_{\rm c}$. The leading contribution to the self-energy is the chemical potential insertion $\mu_{\rm B}$ as well as the one-loop diagram Π_{11} shown in Fig. 8.1:

$$\begin{aligned}\Pi_{11}(i\nu, \boldsymbol{p}) - \Pi_0(i\nu, \boldsymbol{p}) &= g^2\, T \sum_n \int \frac{d\boldsymbol{k}}{(2\pi)^d} G_{11}(i\omega_n + i\nu, \boldsymbol{k} + \boldsymbol{p}) G_{22}(i\omega_n, \boldsymbol{k}) \\ &= -g^2 \int \frac{d\boldsymbol{k}}{(2\pi)^d} \frac{1 - f_{\rm F}(\varepsilon_{\boldsymbol{k}-\boldsymbol{p}/2}) - f_{\rm F}(\varepsilon_{\boldsymbol{k}+\boldsymbol{p}/2})}{2\varepsilon_{\boldsymbol{k}} - i\nu + \varepsilon_{\boldsymbol{p}}/2}.\end{aligned} \tag{9.1}$$

For the zero Matsubara frequency mode $\nu_n = 0$ at the small momentum $\varepsilon_{\boldsymbol{p}} \ll T$, we have

$$\Pi_{11}(0, \boldsymbol{0}) \simeq g^2 \int \frac{d\boldsymbol{k}}{(2\pi)^4} \frac{f_{\rm F}(\varepsilon_{\boldsymbol{k}})}{\varepsilon_{\boldsymbol{k}}} = \epsilon\, T\, 2\ln 2. \tag{9.2}$$

Therefore, the zero Matsubara frequency mode has the non-negative thermal mass $\Pi_T = \epsilon\, T\, 2\ln 2 - \mu_{\rm B} \sim \epsilon$ at $T \geq T_{\rm c}$. The condition of the vanishing thermal mass $\Pi_T = 0$ gives the critical temperature $T_{\rm c} = \mu_{\rm B}/(\epsilon\, 2\ln 2)$ equivalent to Eq. (8.46). As we will see below, at a sufficiently high order in the perturbation theory near $T_{\rm c}$ [ϵ^2 (ϵ) compared to the leading term in the pressure (fermion density)], the resummation of the boson self-energy is needed to avoid infrared singularities appearing in the zero Matsubara frequency mode.

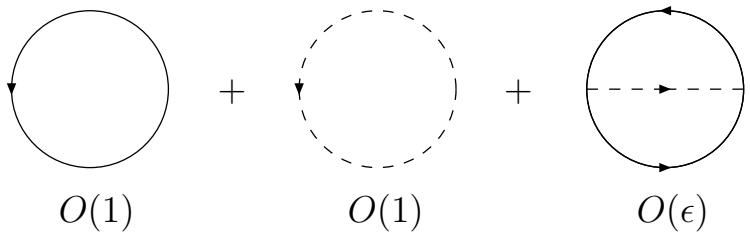

Figure 9.1: Three types of diagrams contributing to the pressure up to the next-to-leading order in ϵ. Each μ (μ_B) insertion to the fermion (boson) line reduces the power of ϵ by one.

9.3 Pressure

Now we calculate the thermodynamic functions at $T \geq T_c$ to the leading and next-to-leading orders in ϵ. There are three types of diagrams contributing to the pressure up to the next-to-leading order in ϵ as depicted in Fig. 9.1; one-loop diagrams with and without one μ (μ_B) insertion and two-loop diagram with a boson exchange. Note that at $T \geq T_c$, the boson's one-loop diagram contributes as $O(1)$ as well as the fermion's one-loop diagram. Then the pressure from the one-loop diagrams is given by

$$\begin{aligned} P_1 &= \int \frac{d\boldsymbol{p}}{(2\pi)^d}\left[2T\ln\left(1+e^{-\varepsilon_{\boldsymbol{p}}/T}\right) - T\ln\left(1-e^{-\varepsilon_{\boldsymbol{p}}/2T}\right) + 2\mu f_{\rm F}(\varepsilon_{\boldsymbol{p}}) + \mu_{\rm B} f_{\rm B}(\varepsilon_{\boldsymbol{p}}/2)\right] \\ &= T\left[\frac{11}{2}\zeta(3) - \frac{9\ln 2\,\zeta(3)+11\zeta'(3)}{4}\epsilon + \frac{\pi^2}{6}\frac{\mu}{T} + \frac{2\pi^2}{3}\frac{\mu_{\rm B}}{T}\right]\left(\frac{mT}{2\pi}\right)^{d/2}. \end{aligned} \tag{9.3}$$

The contribution from the two-loop diagram to the pressure, which is $O(\epsilon)$, is given by

$$\begin{aligned} P_2 &= g^2 T^2 \sum_{n,m}\int \frac{d\boldsymbol{p}\,d\boldsymbol{q}}{(2\pi)^{2d}} G_{11}(i\omega_n,\boldsymbol{p})G_{22}(i\omega_m,\boldsymbol{q})D(i\omega_n - i\omega_m,\boldsymbol{p}-\boldsymbol{q}) \\ &= -g^2\int \frac{d\boldsymbol{p}\,d\boldsymbol{q}}{(2\pi)^{2d}}\,\frac{f_{\rm F}(\varepsilon_{\boldsymbol{p}})f_{\rm F}(\varepsilon_{\boldsymbol{q}}) + \left[f_{\rm F}(\varepsilon_{\boldsymbol{p}}) + f_{\rm F}(\varepsilon_{\boldsymbol{q}})\right] f_{\rm B}(\varepsilon_{\boldsymbol{p}-\boldsymbol{q}}/2)}{\varepsilon_{\boldsymbol{p}} + \varepsilon_{\boldsymbol{q}} - \varepsilon_{\boldsymbol{p}-\boldsymbol{q}}/2}. \end{aligned} \tag{9.4}$$

The numerical integrations over $\boldsymbol{p}$ and $\boldsymbol{q}$ result in

$$P_2 = -C_P\epsilon\left(\frac{mT}{2\pi}\right)^{d/2} T, \tag{9.5}$$

where $C_P \approx 8.4144$. From Eqs. (9.3) and (9.5), we obtain the pressure up to the next-to-leading order in ϵ as

$$\begin{aligned} P &= P_1 + P_2 \\ &= T\left[\frac{11}{2}\zeta(3) - \frac{9\ln 2\,\zeta(3)+11\zeta'(3)}{4}\epsilon - \epsilon\, C_P + \frac{\pi^2}{6}\frac{\mu}{T} + \frac{2\pi^2}{3}\frac{\mu_{\rm B}}{T}\right]\left(\frac{mT}{2\pi}\right)^{d/2}. \end{aligned} \tag{9.6}$$

The entropy density S and the energy density E to the same order can be computed from the thermodynamic relations $S = \partial P/\partial T$ and $E = \mu N + TS - P$.

9.4 Fermion number density

The fermion number density to the next-to-leading order in ϵ can not be obtained simply by differentiating the pressure in Eq. (9.6) with respect to the chemical potential $N = \partial P/\partial\mu$. Since the pressure to the leading order in ϵ does not depend on μ and the μ derivative $\partial/\partial\mu \sim 1/\epsilon$ enhances the power of ϵ by one, we need to compute the one-loop diagrams with two μ ($\mu_{\rm B}$) insertions and two-loop diagrams with one μ ($\mu_{\rm B}$) insertion. Then the fermion density from the fermion's one-loop diagrams is given by

$$\begin{aligned} N_{\rm F} &= 2\int\frac{d\boldsymbol{p}}{(2\pi)^d}\left[f_{\rm F}(\varepsilon_{\boldsymbol{p}}) + \frac{\mu}{T}f_{\rm F}(\varepsilon_{\boldsymbol{p}})f_{\rm F}(-\varepsilon_{\boldsymbol{p}})\right] \\ &= \left[\frac{\pi^2}{6} - \frac{\pi^2\ln 2 + 6\zeta'(2)}{12}\epsilon + \frac{2\ln 2}{T}\mu\right]\left(\frac{mT}{2\pi}\right)^{d/2}. \end{aligned} \tag{9.7}$$

On the other hand, the boson's one-loop diagrams contribute to the fermion density as

$$N_{\rm B} = 2\int\frac{d\boldsymbol{p}}{(2\pi)^d}\left[f_{\rm B}(\varepsilon_{\boldsymbol{p}}/2) - \frac{\mu_{\rm B}}{T}f_{\rm B}(\varepsilon_{\boldsymbol{p}}/2)f_{\rm B}(-\varepsilon_{\boldsymbol{p}}/2)\right]. \tag{9.8}$$

Apparently, the last term has an infrared singularity because the Bose distribution function behaves as $f_{\rm B}(\varepsilon_{\boldsymbol{p}}/2) \simeq 2T/\varepsilon_{\boldsymbol{p}}$ at the small momentum $\varepsilon_{\boldsymbol{p}} \ll T$. In order to resolve this infrared singularity, the resummation of the boson self-energy $\Pi_{11} = \epsilon T\, 2\ln 2$ is needed at the small momentum region $\varepsilon_{\boldsymbol{p}} \sim \mu$. Within the accuracy we are working, we can rewrite $N_{\rm B}$ as

$$N_{\rm B} = 2\int\frac{d\boldsymbol{p}}{(2\pi)^d}\left[f_{\rm B}(\varepsilon_{\boldsymbol{p}}/2 + \Pi_T) - \epsilon\, 2\ln 2\, f_{\rm B}(\varepsilon_{\boldsymbol{p}}/2)f_{\rm B}(-\varepsilon_{\boldsymbol{p}}/2)\right], \tag{9.9}$$

where $\Pi_T = \epsilon T\, 2\ln 2 - \mu_{\rm B}$. Now the first term is infrared finite, where the boson's thermal mass $\Pi_T/T = (2\ln 2)\epsilon - \mu_B/T$ plays a role of an infrared cutoff. Integrating over $\boldsymbol{p}$ and expanding up to the next-to-leading order in ϵ, we have

$$\begin{aligned} &2\int\frac{d\boldsymbol{p}}{(2\pi)^d}f_{\rm B}(\varepsilon_{\boldsymbol{p}}/2 + \Pi_T) \\ &\qquad = \left[\frac{4\pi^2}{3} - \frac{2\pi^2\ln 2 + 12\zeta'(2)}{3}\epsilon - 8\left(1 - \ln\frac{\Pi_T}{T}\right)\frac{\Pi_T}{T} + O(\epsilon^2)\right]\left(\frac{mT}{2\pi}\right)^{d/2}. \end{aligned} \tag{9.10}$$

The logarithmic term $\sim \ln\Pi_T/T$ appears as a consequence of the resummation. The second term in Eq. (9.9), which is still infrared divergent, will cancel with the infrared singularity existing in the two-loop diagram.

The contribution from the two-loop diagrams to the fermion density is given by

$$\begin{aligned} N_2 = -g^2\int&\frac{d\boldsymbol{k}\,d\boldsymbol{p}}{(2\pi)^{2d}} \\ &\times\frac{f_{\rm F}(\varepsilon_{\boldsymbol{k}+\boldsymbol{p}/2})f_{\rm F}(-\varepsilon_{\boldsymbol{k}+\boldsymbol{p}/2})\left[f_{\rm F}(\varepsilon_{\boldsymbol{k}-\boldsymbol{p}/2}) + f_{\rm B}(\varepsilon_{\boldsymbol{p}}/2)\right] - 2f_{\rm F}(\varepsilon_{\boldsymbol{k}+\boldsymbol{p}/2})f_{\rm B}(\varepsilon_{\boldsymbol{p}}/2)f_{\rm B}(-\varepsilon_{\boldsymbol{p}}/2)}{\varepsilon_{\boldsymbol{k}}T}. \end{aligned} \tag{9.11}$$

The second term in the numerator contains the infrared singularity at small $\varepsilon_{\boldsymbol{p}}$. Extracting the divergent part, we can rewrite N_2 as

$$\begin{aligned} N_2 = &-g^2 \int \frac{d\boldsymbol{k}\, d\boldsymbol{p}}{(2\pi)^{2d}} \frac{f_{\rm F}(\varepsilon_{\boldsymbol{k}+\boldsymbol{p}/2}) f_{\rm F}(-\varepsilon_{\boldsymbol{k}+\boldsymbol{p}/2}) \left[f_{\rm F}(\varepsilon_{\boldsymbol{k}-\boldsymbol{p}/2}) + f_{\rm B}(\varepsilon_{\boldsymbol{p}}/2) \right]}{\varepsilon_{\boldsymbol{k}} T} \\ &+ g^2 \int \frac{d\boldsymbol{k}\, d\boldsymbol{p}}{(2\pi)^{2d}} \frac{2 \left[f_{\rm F}(\varepsilon_{\boldsymbol{k}+\boldsymbol{p}/2}) - f_{\rm F}(\varepsilon_{\boldsymbol{k}}) \right] f_{\rm B}(\varepsilon_{\boldsymbol{p}}/2) f_{\rm B}(-\varepsilon_{\boldsymbol{p}}/2)}{\varepsilon_{\boldsymbol{k}} T} \\ &+ 2g^2 \int \frac{d\boldsymbol{k}\, d\boldsymbol{p}}{(2\pi)^{2d}} \frac{f_{\rm F}(\varepsilon_{\boldsymbol{k}})}{\varepsilon_{\boldsymbol{k}} T} f_{\rm B}(\varepsilon_{\boldsymbol{p}}/2) f_{\rm B}(-\varepsilon_{\boldsymbol{p}}/2). \end{aligned} \tag{9.12}$$

One finds the $\boldsymbol{k}$ integration in the last term can be performed to lead to $\Pi_{11} = \epsilon T\, 2\ln 2$ in Eq. (9.2), which exactly cancels out the infrared divergent part in Eq. (9.9). The numerical integrations over $\boldsymbol{k}$ and $\boldsymbol{p}$ in the first two terms result in

$$N_2 = -C_N \epsilon \left(\frac{mT}{2\pi} \right)^{d/2} + \epsilon\, 4 \ln 2 \int \frac{d\boldsymbol{p}}{(2\pi)^d} f_{\rm B}(\varepsilon_{\boldsymbol{p}}/2) f_{\rm B}(-\varepsilon_{\boldsymbol{p}}/2), \tag{9.13}$$

where $C_N \approx 1.92181$. Gathering up all contributions, Eqs. (9.7), (9.9), and (9.13), the fermion number density to the leading and next-to-leading orders is given by

$$\begin{aligned} N &= N_{\rm F} + N_{\rm B} + N_2 \\ &= \left[\frac{3\pi^2}{2} - \frac{3\pi^2 \ln 2 + 18\zeta'(2)}{4} \epsilon - \epsilon C_N + \frac{2\ln 2}{T} \mu - 8 \left(1 - \ln \frac{\Pi_T}{T} \right) \frac{\Pi_T}{T} \right] \left(\frac{mT}{2\pi} \right)^{d/2}. \end{aligned} \tag{9.14}$$

We define the Fermi energy $\varepsilon_{\rm F}$ through the relationship in Eq. (3.41) as

$$\begin{aligned} \frac{\varepsilon_{\rm F}}{T} &= \frac{2\pi}{m} \left[\frac{1}{2} \Gamma \left(\frac{d}{2} + 1 \right) N \right]^{2/d} \\ &= \sqrt{\frac{3\pi^2}{2}} \left[1 + \left\{ \frac{2\gamma - 3 - 2\ln 2}{8} - \frac{3\zeta'(2)}{2\pi^2} - \frac{C_N}{3\pi^2} + \frac{1}{8} \ln \left(\frac{3\pi^2}{2} \right) \right\} \epsilon \right. \\ &\qquad \left. + \frac{2\ln 2}{3\pi^2} \frac{\mu}{T} - \frac{8}{3\pi^2} \left(1 - \ln \frac{\Pi_T}{T} \right) \frac{\Pi_T}{T} \right]. \end{aligned} \tag{9.15}$$

The logarithmic correction $(\Pi_T/T) \ln \Pi_T/T \sim \epsilon \ln \epsilon$ is a consequence of the resummation to avoid the infrared singularities, while it vanishes at the critical temperature $\Pi_{T_c} = \epsilon T_c\, 2\ln 2 - \mu_{\rm B} = 0$.

9.5 Critical temperature

The critical temperature in units of the Fermi energy directly follows from Eq. (9.15) with the use of the relationship $2\mu + \varepsilon_{\rm b} = \epsilon T_c\, 2\ln 2$:

$$\begin{aligned} \frac{T_c}{\varepsilon_{\rm F}} &= \sqrt{\frac{2}{3\pi^2}} \left[1 - \left\{ \frac{2\gamma - 3 - 2\ln 2}{8} - \frac{3\zeta'(2)}{2\pi^2} - \frac{C_N - 2(\ln 2)^2}{3\pi^2} + \frac{1}{8} \ln \left(\frac{3\pi^2}{2} \right) \right\} \epsilon \right] + \frac{\ln 2}{3\pi^2} \frac{\varepsilon_{\rm b}}{\varepsilon_{\rm F}} \\ &= 0.260 - 0.0112\, \epsilon + 0.0234\, \frac{\varepsilon_{\rm b}}{\varepsilon_{\rm F}} + O(\epsilon^2), \end{aligned} \tag{9.16}$$

where the numerical value $C_N \approx 1.92181$ is substituted. We find the critical temperature T_c is an increasing function of the binding energy ε_b near the unitarity limit. The next-to-leading order correction is reasonably small compared to the leading term even at $\epsilon = 1$. The naive extrapolation of the critical temperature to the physical case of $d = 3$ gives $T_c/\varepsilon_F \approx 0.249$ in the unitarity limit $\varepsilon_b = 0$. This value is surprisingly close to results from two Monte Carlo simulations, $T_c/\varepsilon_F = 0.23(2)$ [89] and $T_c/\varepsilon_F \approx 0.25$ [92], while other two simulations provide smaller values, $T_c/\varepsilon_F < 0.14$ [90] and $T_c/\varepsilon_F = 0.152(7)$ [91].

It is also interesting to compare the critical temperature in the unitarity limit with that in the BEC limit T_{BEC}. In the BEC limit, all fermion pairs are confined into tightly bound molecules and the system becomes a non-interacting Bose gas where the boson mass is $2m$ and the boson density is $N/2$. The critical temperature for the Bose-Einstein condensation of such an ideal Bose gas at $d > 2$ spatial dimensions becomes

$$\frac{T_{BEC}}{\varepsilon_F} = \frac{1}{2}\left[\zeta\left(\frac{d}{2}\right)\Gamma\left(1+\frac{d}{2}\right)\right]^{-2/d}. \tag{9.17}$$

To the leading and next-to-leading orders in $\epsilon = 4 - d$, the ratio of the critical temperatures in the unitarity limit T_c and in the BEC limit T_{BEC} at the same fermion density is given by

$$\frac{T_c}{T_{BEC}} = \sqrt{\frac{8}{9}}\left[1 + 0.0177\,\epsilon + O(\epsilon^2)\right] = 0.943 + 0.0167\,\epsilon + O(\epsilon^2). \tag{9.18}$$

The ratio is slightly below unity, indicating the lower critical temperature in the unitarity limit $T_c < T_{BEC}$. The leading order term of the above ratio, $T_c/T_{BEC} = \sqrt{8/9}$, has the following clear physical interpretation: The critical temperature for the Bose-Einstein condensation at $d = 4$ is proportional to a square root of the boson's density. In the BEC limit, all fermion pairs form the bound bosons, while only 8 of 9 fermion pairs form the bosons and 1 of 9 fermion pairs is dissociated in the unitarity limit [see the leading order terms in Eqs. (9.7) and (9.10)]. Thus, their ratio in the critical temperature should be $T_c/T_{BEC} = \sqrt{8/9} < 1$ at $d = 4$.

The more appropriate estimate of T_c at $d = 3$ will be obtained by matching the ϵ expansion with the exact result around $d = 2$. The critical temperature at unitarity in the expansion over $\bar{\epsilon} = d - 2$ is given by $T_c = (e^\gamma/\pi)\,\Delta$, where $\Delta/\varepsilon_F = (2/e)\,e^{-1/\bar{\epsilon}}$ is the energy gap of the fermion quasiparticle at zero temperature [94]:

$$\frac{T_c}{\varepsilon_F} = \frac{2e^{\gamma-1}}{\pi}\,e^{-1/\bar{\epsilon}}\left[1 + O(\bar{\epsilon})\right]. \tag{9.19}$$

We shall write the power series of $\bar{\epsilon}$ in the form of the Borel transformation,

$$\frac{T_c(\bar{\epsilon})}{\varepsilon_F} = \frac{2e^{\gamma-1}}{\pi}\,e^{-1/\bar{\epsilon}}\int_0^\infty dt\,e^{-t}B_{T_c}(\bar{\epsilon}t). \tag{9.20}$$

$B_{T_c}(t)$ is the Borel transform of the power series in $T_c(\bar{\epsilon})$, whose Taylor coefficients at origin is given by $B_{T_c}(t) = 1 + \cdots$. In order to perform the integration over t in Eq. (9.20), the analytic continuation of the Borel transform $B_{T_c}(t)$ to the real positive axis of t is necessary. Here we employ the Padé

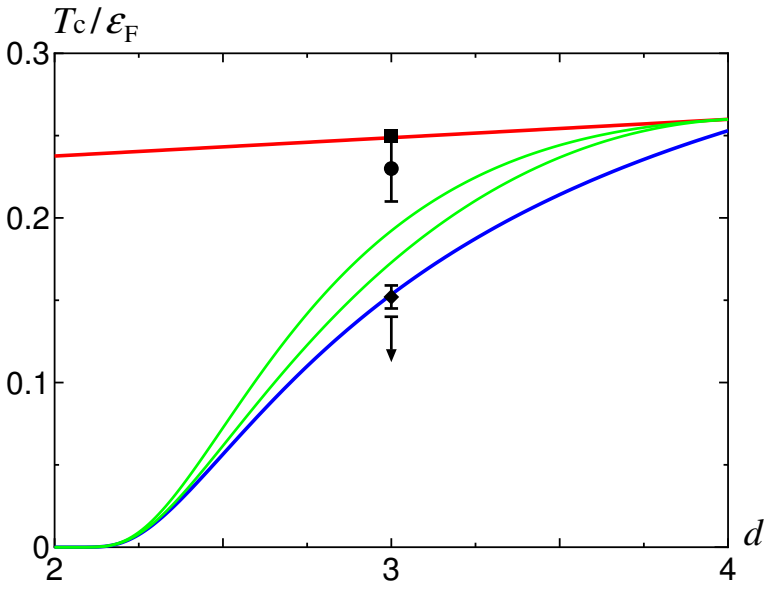

Figure 9.2: The critical temperature T_c at unitarity as a function of the spatial dimensions d. The upper solid line is from the expansion around $d = 4$ in Eq. (9.16), while the lower solid line is from the expansion around $d = 2$ in Eq. (9.19). The middle two curves show the different Borel–Padé approximants connecting the two expansions. The symbols at $d = 3$ indicate the results from the Monte Carlo simulations; $T_c/\varepsilon_F = 0.23(2)$ [89] (circle), $T_c/\varepsilon_F < 0.14$ [90] (down arrow), $T_c/\varepsilon_F = 0.152(7)$ [91] (diamond), and $T_c/\varepsilon_F \approx 0.25$ [92] (square).

approximant, where $B_{T_c}(t)$ is replaced by the following rational functions

$$B_{T_c}(t) = \frac{1 + p_1 t + \cdots + p_M t^M}{1 + q_1 t + \cdots + q_N t^N} . \tag{9.21}$$

Then we incorporate the results around four spatial dimensions in Eq. (9.16) by imposing

$$\frac{T_c(2-\epsilon)}{\varepsilon_F} = 0.260 - 0.0112\,\epsilon + \cdots \tag{9.22}$$

on the Padé approximants as a boundary condition. Since we have two known coefficients from the ϵ expansion, the Padé approximants $[M/N]$ satisfying $M + N = 2$ are possible. Since we could not find a solution satisfying the boundary condition in Eq. (9.22) for $[M/N] = [1/1]$, we adopt other two Padé approximants with $[M/N] = [2/0]$, $[0/2]$, whose coefficients p_m and q_n are determined uniquely by the above conditions.

Fig. 9.2 shows the critical temperature T_c in units of the Fermi energy ε_F as a function of the spatial dimensions d. The middle two curves show T_c/ε_F in the different Padé approximants connecting the two expansions around $d = 4$ and $d = 2$. These Borel–Padé approximants give $T_c/\varepsilon_F = 0.173$ and 0.192 at $d = 3$, which are located between the naive extrapolations to $d = 3$ from the $\epsilon = 4 - d$ expansion ($T_c/\varepsilon_F \to 0.249$) and the $\bar{\epsilon} = d - 2$ expansion ($T_c/\varepsilon_F \to 0.153$). It is also interesting to compare our results with those from the recent Monte Carlo simulations, where $T_c/\varepsilon_F = 0.23(2)$ [89],

$T_c/\varepsilon_F < 0.14$ [90], $T_c/\varepsilon_F = 0.152(7)$ [91], and $T_c/\varepsilon_F \approx 0.25$ [92]. Although these results from the Monte Carlo simulations seem not to be settled, the interpolation of the two expansions provides the moderate value $T_c/\varepsilon_F = 0.183 \pm 0.014$ not too far from the Monte Carlo simulations.

9.6 Thermodynamic functions at T_c

Finally we show the thermodynamic functions at T_c in the unitarity limit $\varepsilon_b = 0$ to the leading and next-to-leading orders in ϵ. The pressure P normalized by the fermion density $\varepsilon_F N$ follows from Eqs. (9.6), (9.14), and (9.15). Introducing the numerical values $C_P \approx 8.4144$ and $C_N \approx 1.92181$, we obtain the pressure up to the next-to-leading order in ϵ as

$$\left.\frac{P}{\varepsilon_F N}\right|_{T_c} = 0.116 + 0.0188\,\epsilon. \tag{9.23}$$

From the universal relationship in the unitarity limit $E = (d/2)P$, the energy density is given by

$$\left.\frac{E}{\varepsilon_F N}\right|_{T_c} = 0.232 - 0.0205\,\epsilon. \tag{9.24}$$

The chemical potential at the critical temperature $\mu = \epsilon\, T_c \ln 2$ is $O(\epsilon)$. Normalizing μ by the Fermi energy in Eq. (9.16), we have

$$\left.\frac{\mu}{\varepsilon_F}\right|_{T_c} = \epsilon \ln 2 \sqrt{\frac{2}{3\pi^2}} = 0.180\,\epsilon. \tag{9.25}$$

Then the entropy density $T_c S = (d/2 + 1)P - \mu N$ is given by

$$\left.\frac{S}{N}\right|_{T_c} = 1.340 - 0.642\,\epsilon. \tag{9.26}$$

The next-to-leading order corrections to the pressure and energy density are reasonably small compared to the leading order terms, while that is large for the entropy density.

We match the thermodynamic functions at T_c in the expansions over $\epsilon = 4 - d$ with those around $d = 2$ as we demonstrated for T_c/ε_F. The critical temperature around $d = 2$ is $T_c/\varepsilon_F \sim e^{-1/\bar{\epsilon}}$, which is exponentially small and negligible compared to any power series of $\bar{\epsilon}$. Therefore, the pressure, energy density, and chemical potential at T_c in the expansions over $\bar{\epsilon} = d - 2$ is simply given by those at zero temperature [94];

$$\left.\frac{P}{\varepsilon_F N}\right|_{T_c} = \frac{2}{d+2}\,\xi = \frac{1}{2} - \frac{5}{8}\bar{\epsilon}, \tag{9.27}$$

$$\left.\frac{E}{\varepsilon_F N}\right|_{T_c} = \frac{d}{d+2}\,\xi = \frac{1}{2} - \frac{3}{8}\bar{\epsilon}, \tag{9.28}$$

$$\left.\frac{\mu}{\varepsilon_F}\right|_{T_c} = \xi = 1 - \bar{\epsilon}. \tag{9.29}$$

	T_c/ε_F	$P/(\varepsilon_F N)$	$E/(\varepsilon_F N)$	μ/ε_F	S/N
ϵ expansion (NLO)	0.249	0.135	0.212	0.180	0.698
Borel–Padé approximant	0.183	0.172	0.270	0.294	0.642
self-consistent approach [78]	0.160	0.204	0.304	0.394	0.71
Monte Carlo simulation [89]	0.23(2)	0.27	0.41	0.45	0.99
Monte Carlo simulation [91]	0.152(7)	0.207(7)	0.31(1)	0.493(14)	0.16(2)

Table 9.1: Comparison of the results by the ϵ expansion with other analytic and numerical calculations in the unitarity limit.

A straightforward calculation shows that the entropy per particle at T_c to the leading order in $\bar{\epsilon}$ is given by

$$\left.\frac{S}{N}\right|_{T_c} = \frac{\pi^2}{3}\frac{T_c}{\varepsilon_F} = \frac{2\pi e^{\gamma-1}}{3}\, e^{-1/\bar{\epsilon}}. \tag{9.30}$$

Using the Borel–Padé approximants connecting the two expansions above, thermodynamic functions at $d = 3$ are found to be $P/(\varepsilon_F N)|_{T_c} = 0.172 \pm 0.022$, $E/(\varepsilon_F N)|_{T_c} = 0.270 \pm 0.004$, $\mu/\varepsilon_F|_{T_c} = 0.294 \pm 0.013$, and $S/N|_{T_c} = 0.642$. The errors here indicates only the uncertainty due to the choice of different Padé approximants. In Table 9.1, we summarize our results on the critical temperature T_c and the thermodynamic functions at T_c as well as results from other analytic and numerical calculations. In the recent Monte Carlo simulation, the thermodynamic functions at the critical temperature is $P/(\varepsilon_F N)|_{T_c} = 0.207(7)$, $E/(\varepsilon_F N)|_{T_c} = 0.31(1)$, $\mu/\varepsilon_F|_{T_c} = 0.493(14)$, and $S/N|_{T_c} = 0.16(2)$ [91]. We see that the interpolations of the two expansions indeed improve the series summations compared to the naive extrapolations from $d = 4$ or $d = 2$, while there still exist deviations between our results and the Monte Carlo simulation. We can understand these deviations partially due to the difference in the determined critical temperature. The large deviations existing in μ/ε_F and S/N may be because we know only the leading term for μ and the next-to-leading order correction for S is sizable.

Chapter 10

Summary and concluding remarks

We have developed the systematic expansion for the Fermi gas near the unitarity limit treating the dimensionality of space d as close to four. To the leading and next-to-leading orders in the expansion over $\epsilon = 4 - d$, the thermodynamic functions and the fermion quasiparticle spectrum were calculated as functions of the binding energy $\varepsilon_{\rm b}$ of the two-body state. Results for the physical case of three spatial dimensions were obtained by extrapolating the series expansions to $\epsilon = 1$. We found the universal parameter of the unitary Fermi gas to be

$$\xi \equiv \frac{\mu}{\varepsilon_{\rm F}} = \frac{1}{2}\epsilon^{3/2} + \frac{1}{16}\epsilon^{5/2}\ln\epsilon - 0.0246\,\epsilon^{5/2} + O(\epsilon^{7/2}) \approx 0.475. \tag{10.1}$$

The fermion quasiparticle spectrum in the unitarity limit was given by the form $\omega_{\rm F}(\boldsymbol{p}) \simeq \sqrt{(\varepsilon_{\boldsymbol{p}} - \varepsilon_0)^2 + \Delta^2}$ with the energy gap

$$\frac{\Delta}{\mu} = \frac{2}{\epsilon} - 0.691 + O(\epsilon) \approx 1.31 \tag{10.2}$$

and the location of the minimum of the dispersion curve

$$\frac{\varepsilon_0}{\mu} = 2 + O(\epsilon) \approx 2. \tag{10.3}$$

We also found the condensate fraction in the fermion density to be

$$\frac{N_0}{N} = 1 - 0.0966\,\epsilon - 0.2423\,\epsilon^2 + O(\epsilon^3) \approx 0.661. \tag{10.4}$$

Although we have only the first two terms in the ϵ expansion, these extrapolated values give reasonable results consistent with the Monte Carlo simulations or the experimental measurements. Furthermore, the corrections are not too large even when extrapolated to $\epsilon = 1$, which suggests that the picture of the unitary Fermi gas as a collection of weakly interacting fermionic and bosonic quasiparticles may be a useful starting point even in three spatial dimensions.

We have also formulated the systematic expansion for the unitary Fermi gas around two spatial dimensions. We used the results around $d = 2$ as boundary conditions which should be satisfied by the series summations of the expansion over $\epsilon = 4 - d$. The simple Borel–Padé approximants connecting the two expansions yielded $\xi = 0.378 \pm 0.013$ at $d = 3$, which is small compared to

the naive extrapolation of the ϵ expansion [Fig. 7.1]. In order for the accurate determination of ξ at $d = 3$, the precise knowledge on the large order behavior of the expansion around four spatial dimensions as well as the calculation of higher order corrections would be desirable. Once these information become available, a conformal mapping technique, if applicable, will further improve the series summations [133].

In Chapters 4 and 5, the phase structure of the polarized Fermi gas in the unitary regime with equal and unequal masses has been studied based on the ϵ expansion. The gapless superfluid phase and the superfluid phase with spatially varying condensate were found to exist between the gapped superfluid phase and the polarized normal phase in a certain range of the binding energy and the mass difference. In the equal mass limit, our study gives a microscopic foundation to the phase structure around the splitting point which has been proposed using the effective field theory [112]. Moreover, we found the gapless phase with spatially varying condensate around $d = 4$ exists only at $0.494 \lesssim (ak_{\rm F})^{-1} \lesssim 1$ and terminates near the unitarity limit. Our result suggests that the phase with spatially varying condensate existing in the unitary regime may be separated from the FFLO phase in the BCS regime [124, 125]. We also found the splitting point and the same phase structure around it in the unitarity limit but with finite mass difference when the majority is the lighter fermions. The range of the superfluid phase with spatially varying condensate can be estimated to be $1.37 \lesssim m_{\rm minority}/m_{\rm majority} \lesssim 3$. The splitting points form a smooth line in the three-dimensional phase diagram of $1/(ak_{\rm F})$, the mass difference κ, and polarization chemical potential H. It gets away from the unitarity with increasing the mass of major fermions. Eventually the splitting point becomes unstable due to the competition with the polarized normal state at the point given by $(ak_{\rm F})^{-1} \approx 1.81$ and $m_{\rm majority}/m_{\rm minority} \approx 5.54$. Further investigation will be worthwhile to confirm these possibility.

In Chapters 8 and 9, the thermodynamics of the Fermi gas near the unitarity limit at finite temperature has been investigated using the systematic expansion over $\epsilon = 4 - d$. We discussed that the thermodynamics in the low temperature region $T \ll T_{\rm c}$ is dominated by the bosonic phonon excitations. The analytic formulas for the thermodynamic functions at the fixed fermion density are derived in the two limiting cases; $T \ll \epsilon T_{\rm c}$ in Eqs. (8.31)–(8.34) and $\epsilon T_{\rm c} \ll T \ll T_{\rm c}$ in Eqs. (8.41)–(8.44). In the high temperature region $T \sim T_{\rm c}$, the fermionic quasiparticles are excited as well as the bosonic quasiparticles. We showed that the similar power counting rule of ϵ to that developed at zero temperature works even above $T_{\rm c}$. The critical temperature $T_{\rm c}$ and the thermodynamic functions around $T_{\rm c}$ were calculated to the leading and next-to-leading orders in ϵ. We found the critical temperature is an increasing function of the binding energy $\varepsilon_{\rm b}$ near the unitarity limit:

$$\frac{T_{\rm c}}{\varepsilon_{\rm F}} = 0.260 - 0.0112\,\epsilon + 0.0234\,\frac{\varepsilon_{\rm b}}{\varepsilon_{\rm F}} + O(\epsilon^2). \tag{10.5}$$

The next-to-leading order correction is reasonably small compared to the leading term even at $\epsilon = 1$. In the unitarity limit $\varepsilon_{\rm b} = 0$, the naive extrapolation of the critical temperature to the physical case of $d = 3$ gives $T_{\rm c}/\varepsilon_{\rm F} \approx 0.249$.

We also discussed the matching of the ϵ expansion with the expansion around $d = 2$. The critical temperature at unitarity in the expansion over $\bar{\epsilon} = d - 2$ is given by $T_{\rm c}/\varepsilon_{\rm F} = \left(2e^{\gamma-1}/\pi\right) e^{-1/\bar{\epsilon}}$, whose

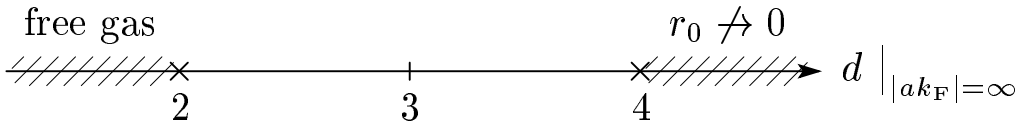

Figure 10.1: The Fermi gas at infinity scattering length $ak_\mathrm{F} \to \infty$ as a function of the spatial dimension d. At $d < 2$, such a system becomes a free Fermi gas, while the limit of zero-range interaction $r_0 k_\mathrm{F} \to 0$ can not be taken at $d > 4$. Therefore, the non-trivial universal limit exists only at $2 < d < 4$.

naive extrapolation to $\bar{\epsilon} = 1$ gives $T_\mathrm{c}/\varepsilon_\mathrm{F} \approx 0.153$. The Borel–Padé approximants connecting the two expansions yielded $T_\mathrm{c}/\varepsilon_\mathrm{F} = 0.183 \pm 0.014$ at $d = 3$, which is a moderate value located between the two naive extrapolations [Fig. 9.2]. These values are not too far from the results obtained by the recent Monte Carlo simulations where $T_\mathrm{c}/\varepsilon_\mathrm{F} = 0.15 \sim 0.25$ [89, 91, 92]. We also applied the Borel–Padé approximants to the thermodynamic functions at T_c, which yielded $P/(\varepsilon_\mathrm{F}N)|_{T_\mathrm{c}} \approx 0.172$, $E/(\varepsilon_\mathrm{F}N)|_{T_\mathrm{c}} \approx 0.270$, $\mu/\varepsilon_\mathrm{F}|_{T_\mathrm{c}} \approx 0.294$, and $S/N|_{T_\mathrm{c}} \approx 0.642$ at $d = 3$.

We conclude that the ϵ expansion is not only theoretically interesting but also provides us an useful analytical tool to investigate the properties of the unitary Fermi gas. Although our results are consistent with those from Monte Carlo simulation, there are several problems which should be clarified in future. For example, the Borel–Padé approximants employed here to match the two expansions around four and two spatial dimensions do not take into account the large order behavior of the expansions around $d = 4$ and $d = 2$. Most probably, the expansions over $\epsilon = 4 - d$ and $\bar{\epsilon} = d - 2$ are not convergent because $d = 4$ and $d = 2$ corresponds to the quantum phase transition points as depicted in Fig. 10.1. Thus the Borel transform $B(t)$ of such series expansions will have singularities somewhere in the complex t-plane. Furthermore, an understanding of the analytic structure of high-order terms in the perturbation theory around $d = 4$ is currently lacking. In order for the accurate determination of the universal quantities, e.g., ξ, $T_\mathrm{c}/\varepsilon_\mathrm{F}$, at $d = 3$, it will be important to appropriately take into account the knowledge on the large order behaviors of the expansions both around four and two spatial dimensions. The calculation of higher order corrections to our results is also important for this purpose. In Appendix, we show a type of diagrams which grows as a factorial of n at order ϵ^n and may be related with the large order behavior of the ϵ expansion. These problems should be further studied in future works. Also the application of the ϵ expansion to investigate other problems of the unitary Fermi gas, including its dynamical properties (dynamical response functions and kinetic coefficients) and the structure of superfluid vortices, will be extremely interesting.

Acknowledgments

I am grateful to all members of the theoretical nuclear physics group in the University of Tokyo for many useful discussions during I was a graduate student there. My supervisor Prof. Tetsuo Hatsuda drew my attention to the interesting field of quantum chromodynamics (QCD) at finite temperature and density, which is an intersection of condensed matter physics and high energy physics, when I was an undergraduate student. I would like to thank him for continuous and stimulating discussions on a large variety of subjects in physics. He also encouraged me to study abroad, without which I could not finish my thesis as its present form.

All works in this thesis were completed during I was visiting the Institute for Nuclear Theory in Seattle to collaborate with Prof. Dam Thanh Son. I am grateful to him for accepting me as a visiting scholar and for continuous and stimulating discussions on the physics of QCD and cold atomic gases. It was very fruitful to discuss and work with him together and I could learn many things as a researcher. I would really like to thank all people in the Institute and Robert Ingalls for their hospitality. Especially the discussions with Dr. Michael McNeil Forbes and Dr. Gautam Rupak were very helpful when I could not figure out how to organize the ϵ expansion correctly.

Finally I would like to express my sincere gratitude to my parents and family, who have kept me studying what I like to through moral and financial support. My father and grandfather raised my interest in physics, astronomy, and science during I was a child. Minako always gave me much encouragement and pleasure whenever I was in hard times and good times. I was supported by the predoctoral research fellowship of the Japan Society for the Promotion of Science for the last three years of my PhD course.

Appendix A

Large orders in the $\epsilon = 4 - d$ expansion

In this Appendix, we show that there exists a type of diagrams which grows as $n!$ by itself at order ϵ^n of the $\epsilon = 4 - d$ expansion. Such a factorial contribution originates from the large momentum region of the loop integrals which resembles the *ultraviolet renormalon* in relativistic field theories [137, 138, 139]. An example of the $n+1$-loop diagram contributing to the effective potential as $n!$ at $O(\epsilon^n)$ is depicted in Fig. A.1, which can be written as

$$V_n = \frac{i}{n} \int \frac{dk}{(2\pi)^{d+1}} \left[(\Pi_0(k) + \Pi_{\rm a}(k))\, D(k) \right]^n , \tag{A.1}$$

where $\Pi_0(k)$, $\Pi_{\rm a}(k)$, and $D(k)$ are respectively defined in Eqs. (3.10), (3.17), and (3.8). Introducing these definitions and integrating over k_0, we obtain the following expression for V_n,

$$\begin{aligned} V_n = \frac{i}{n} \int \frac{dk}{(2\pi)^{d+1}} \Bigg[& 1 + \frac{-g^2}{k_0 - \frac{\varepsilon_{\boldsymbol{k}}}{2} + i\delta} \int \frac{d\boldsymbol{p}}{(2\pi)^d} \frac{1}{4 E_{\boldsymbol{p}-\frac{\boldsymbol{k}}{2}} E_{\boldsymbol{p}+\frac{\boldsymbol{k}}{2}}} \\ & \times \left\{ \frac{(E_{\boldsymbol{p}-\frac{\boldsymbol{k}}{2}} + \varepsilon_{\boldsymbol{p}-\frac{\boldsymbol{k}}{2}})(E_{\boldsymbol{p}+\frac{\boldsymbol{k}}{2}} + \varepsilon_{\boldsymbol{p}+\frac{\boldsymbol{k}}{2}})}{E_{\boldsymbol{p}-\frac{\boldsymbol{k}}{2}} + E_{\boldsymbol{p}+\frac{\boldsymbol{k}}{2}} - k_0 - i\delta} + \frac{(E_{\boldsymbol{p}-\frac{\boldsymbol{k}}{2}} - \varepsilon_{\boldsymbol{p}-\frac{\boldsymbol{k}}{2}})(E_{\boldsymbol{p}+\frac{\boldsymbol{k}}{2}} - \varepsilon_{\boldsymbol{p}+\frac{\boldsymbol{k}}{2}})}{E_{\boldsymbol{p}-\frac{\boldsymbol{k}}{2}} + E_{\boldsymbol{p}+\frac{\boldsymbol{k}}{2}} + k_0 - i\delta} \right\} \Bigg]^n \\ = -\frac{g^2}{4} \int \frac{d\boldsymbol{k} d\boldsymbol{p}}{(2\pi)^{2d}} & \frac{(E_{\boldsymbol{p}-\frac{\boldsymbol{k}}{2}} - \varepsilon_{\boldsymbol{p}-\frac{\boldsymbol{k}}{2}})(E_{\boldsymbol{p}+\frac{\boldsymbol{k}}{2}} - \varepsilon_{\boldsymbol{p}+\frac{\boldsymbol{k}}{2}})}{E_{\boldsymbol{p}-\frac{\boldsymbol{k}}{2}} E_{\boldsymbol{p}+\frac{\boldsymbol{k}}{2}} \left(E_{\boldsymbol{p}-\frac{\boldsymbol{k}}{2}} + E_{\boldsymbol{p}+\frac{\boldsymbol{k}}{2}} + \frac{\varepsilon_{\boldsymbol{k}}}{2} \right)} \\ & \times \Bigg[1 + \frac{g^2}{E_{\boldsymbol{p}-\frac{\boldsymbol{k}}{2}} + E_{\boldsymbol{p}+\frac{\boldsymbol{k}}{2}} + \frac{\varepsilon_{\boldsymbol{k}}}{2}} \int \frac{d\boldsymbol{q}}{(2\pi)^d} \frac{1}{4 E_{\boldsymbol{q}-\frac{\boldsymbol{k}}{2}} E_{\boldsymbol{q}+\frac{\boldsymbol{k}}{2}}} \\ & \quad \times \left\{ \frac{(E_{\boldsymbol{q}-\frac{\boldsymbol{k}}{2}} + \varepsilon_{\boldsymbol{q}-\frac{\boldsymbol{k}}{2}})(E_{\boldsymbol{q}+\frac{\boldsymbol{k}}{2}} + \varepsilon_{\boldsymbol{q}+\frac{\boldsymbol{k}}{2}})}{E_{\boldsymbol{q}-\frac{\boldsymbol{k}}{2}} + E_{\boldsymbol{q}+\frac{\boldsymbol{k}}{2}} + E_{\boldsymbol{p}-\frac{\boldsymbol{k}}{2}} + E_{\boldsymbol{p}+\frac{\boldsymbol{k}}{2}}} + \frac{(E_{\boldsymbol{q}-\frac{\boldsymbol{k}}{2}} - \varepsilon_{\boldsymbol{q}-\frac{\boldsymbol{k}}{2}})(E_{\boldsymbol{q}+\frac{\boldsymbol{k}}{2}} - \varepsilon_{\boldsymbol{q}+\frac{\boldsymbol{k}}{2}})}{E_{\boldsymbol{q}-\frac{\boldsymbol{k}}{2}} + E_{\boldsymbol{q}+\frac{\boldsymbol{k}}{2}} - E_{\boldsymbol{p}-\frac{\boldsymbol{k}}{2}} - E_{\boldsymbol{p}+\frac{\boldsymbol{k}}{2}}} \right\} \Bigg]^{n-1} . \end{aligned} \tag{A.2}$$

Then we consider the $\boldsymbol{q}$ integration in the bracket. Since the $\boldsymbol{q}$ integration contains a logarithmic divergence at $d = 4$, we subtract and add its divergent piece as

$$\begin{aligned} & 1 + \frac{g^2}{E_{\boldsymbol{p}-\frac{\boldsymbol{k}}{2}} + E_{\boldsymbol{p}+\frac{\boldsymbol{k}}{2}} + \frac{\varepsilon_{\boldsymbol{k}}}{2}} \int \frac{d\boldsymbol{q}}{(2\pi)^d} \frac{1}{4 E_{\boldsymbol{q}-\frac{\boldsymbol{k}}{2}} E_{\boldsymbol{q}+\frac{\boldsymbol{k}}{2}}} \left\{ \cdots \right\} \\ & \quad = 1 + \frac{g^2}{E_{\boldsymbol{p}-\frac{\boldsymbol{k}}{2}} + E_{\boldsymbol{p}+\frac{\boldsymbol{k}}{2}} + \frac{\varepsilon_{\boldsymbol{k}}}{2}} \int \frac{d\boldsymbol{q}}{(2\pi)^d} \left[\frac{1}{4 E_{\boldsymbol{q}-\frac{\boldsymbol{k}}{2}} E_{\boldsymbol{q}+\frac{\boldsymbol{k}}{2}}} \left\{ \cdots \right\} - \frac{1}{2\varepsilon_{\boldsymbol{q}} + E_{\boldsymbol{p}-\frac{\boldsymbol{k}}{2}} + E_{\boldsymbol{p}+\frac{\boldsymbol{k}}{2}} + \frac{\varepsilon_{\boldsymbol{k}}}{2}} \right] \\ & \qquad + \frac{g^2}{E_{\boldsymbol{p}-\frac{\boldsymbol{k}}{2}} + E_{\boldsymbol{p}+\frac{\boldsymbol{k}}{2}} + \frac{\varepsilon_{\boldsymbol{k}}}{2}} \int \frac{d\boldsymbol{q}}{(2\pi)^d} \frac{1}{2\varepsilon_{\boldsymbol{q}} + E_{\boldsymbol{p}-\frac{\boldsymbol{k}}{2}} + E_{\boldsymbol{p}+\frac{\boldsymbol{k}}{2}} + \frac{\varepsilon_{\boldsymbol{k}}}{2}} . \end{aligned} \tag{A.3}$$

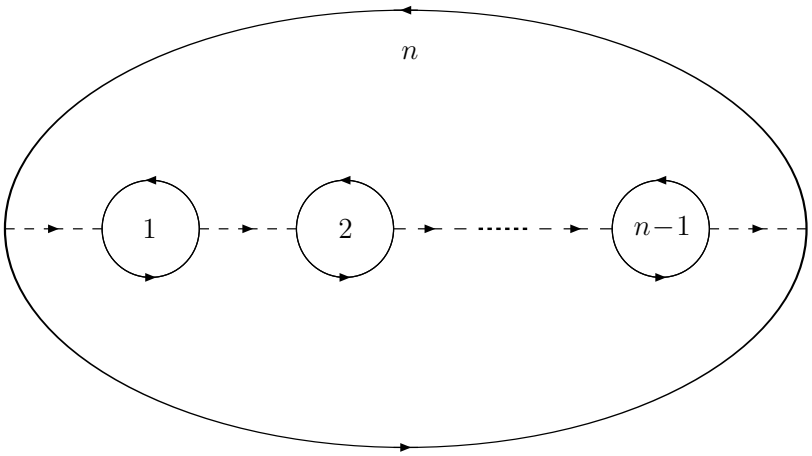

Figure A.1: A n-th order diagram at $d = 4$ which contributes to the effective potential as $n!$ by itself. The counter vertex $-i\Pi_0$ for each bubble diagram is understood implicitly.

The $\boldsymbol{q}$ integration in the second line becomes finite at $d = 4$ and does not produce singular logarithmic terms. So we concentrate on the $\boldsymbol{q}$ integration in the last line, which can be evaluated in the dimensional regularization as

$$\begin{aligned} &1 + \frac{g^2}{E_{\boldsymbol{p}-\frac{\boldsymbol{k}}{2}} + E_{\boldsymbol{p}+\frac{\boldsymbol{k}}{2}} + \frac{\varepsilon_{\boldsymbol{k}}}{2}} \int \frac{d\boldsymbol{q}}{(2\pi)^d} \frac{1}{2\varepsilon_{\boldsymbol{q}} + E_{\boldsymbol{p}-\frac{\boldsymbol{k}}{2}} + E_{\boldsymbol{p}+\frac{\boldsymbol{k}}{2}} + \frac{\varepsilon_{\boldsymbol{k}}}{2}} \\ &\quad = 1 + \frac{\epsilon}{2}\Gamma\left(1 - \frac{d}{2}\right)\left(\frac{E_{\boldsymbol{p}-\frac{\boldsymbol{k}}{2}} + E_{\boldsymbol{p}+\frac{\boldsymbol{k}}{2}} + \frac{\varepsilon_{\boldsymbol{k}}}{2}}{2\phi_0}\right)^{-\frac{\epsilon}{2}} \\ &\quad = \frac{\epsilon}{2}\ln\left(\frac{E_{\boldsymbol{p}-\frac{\boldsymbol{k}}{2}} + E_{\boldsymbol{p}+\frac{\boldsymbol{k}}{2}} + \frac{\varepsilon_{\boldsymbol{k}}}{2}}{2\phi_0}\right) + O(\epsilon^2). \end{aligned} \tag{A.4}$$

Then V_n in Eq. (A.2) to the order ϵ^n becomes

$$\begin{aligned} V_n &= -\frac{g^2}{4}\int \frac{d\boldsymbol{k}d\boldsymbol{p}}{(2\pi)^{2d}} \frac{(E_{\boldsymbol{p}-\frac{\boldsymbol{k}}{2}} - \varepsilon_{\boldsymbol{p}-\frac{\boldsymbol{k}}{2}})(E_{\boldsymbol{p}+\frac{\boldsymbol{k}}{2}} - \varepsilon_{\boldsymbol{p}+\frac{\boldsymbol{k}}{2}})}{E_{\boldsymbol{p}-\frac{\boldsymbol{k}}{2}}E_{\boldsymbol{p}+\frac{\boldsymbol{k}}{2}}\left(E_{\boldsymbol{p}-\frac{\boldsymbol{k}}{2}} + E_{\boldsymbol{p}+\frac{\boldsymbol{k}}{2}} + \frac{\varepsilon_{\boldsymbol{k}}}{2}\right)} \left[\frac{\epsilon}{2}\ln\left(\frac{E_{\boldsymbol{p}-\frac{\boldsymbol{k}}{2}} + E_{\boldsymbol{p}+\frac{\boldsymbol{k}}{2}} + \frac{\varepsilon_{\boldsymbol{k}}}{2}}{2\phi_0}\right) + \text{ regular terms}\right]^{n-1} \\ &= -\frac{g^2}{4}\int \frac{d\boldsymbol{p}d\boldsymbol{q}}{(2\pi)^{2d}} \frac{(E_{\boldsymbol{p}} - \varepsilon_{\boldsymbol{p}})(E_{\boldsymbol{q}} - \varepsilon_{\boldsymbol{q}})}{E_{\boldsymbol{p}}E_{\boldsymbol{q}}\left(E_{\boldsymbol{p}} + E_{\boldsymbol{q}} + \frac{\varepsilon_{\boldsymbol{p}-\boldsymbol{q}}}{2}\right)} \left[\frac{\epsilon}{2}\ln\left(\frac{E_{\boldsymbol{p}} + E_{\boldsymbol{q}} + \frac{\varepsilon_{\boldsymbol{p}-\boldsymbol{q}}}{2}}{2\phi_0}\right) + \text{ regular terms}\right]^{n-1}. \end{aligned} \tag{A.5}$$

By picking up the logarithmic terms, we find the $\boldsymbol{p}$ integration from its large momentum region $\varepsilon_{\boldsymbol{p}} \gg \varepsilon_{\boldsymbol{q}}$ and $\varepsilon_{\boldsymbol{p}} \gg \phi_0$ gives the following contribution to the effective potential,

$$\begin{aligned} V_n &\sim \epsilon \int \frac{d\boldsymbol{p}}{(2\pi)^d}\left(\frac{1}{\varepsilon_{\boldsymbol{p}}}\right)^3\left(\frac{\epsilon}{2}\ln\varepsilon_{\boldsymbol{p}}\right)^{n-1} \\ &\sim \left(\frac{\epsilon}{2}\right)^n \int d\varepsilon_{\boldsymbol{p}}\left(\frac{1}{\varepsilon_{\boldsymbol{p}}}\right)^2 (\ln\varepsilon_{\boldsymbol{p}})^{n-1} \\ &\sim \left(\frac{\epsilon}{2}\right)^n \Gamma(n), \end{aligned} \tag{A.6}$$

which grows as a factorial of n. Note that this $n!$ contribution comes from the single diagram depicted in Fig. A.1. At the moment, it is not clear whether such a $n!$ contribution survives at $O(\epsilon^n)$ of the effective potential and dominates the large order behavior of the ϵ expansion. Possibly there might be cancellations with other n-th order diagrams and/or with subleading contributions from lower-order diagrams.

Bibliography

[1] L. N. Cooper, *Bound Electron Pairs in a Degenerate Fermi Gas*, Phys. Rev. **104**, 1189 (1956).

[2] J. Bardeen, L. N. Cooper, and J. R. Schrieffer, *Microscopic Theory of Superconductivity*, Phys. Rev. **106**, 162 (1957); *Theory of Superconductivity*, Phys. Rev. **108**, 1175 (1957).

[3] H. Kamerlingh Onnes, *On the sudden change in the rate at which the resistance of mercury disappears*, Akad. van Wetenschappen **14(113)**, 818 (1911).

[4] D. D. Osheroff, R. C. Richardson, and D. M. Lee, *Evidence for a New Phase of Solid He^3*, Phys. Rev. Lett. **28**, 885 (1972).

[5] J. G. Bednorz and K. Müller, *Possible high-T_c superconductivity in the Ba-La-Cu-O system*, Z. Physik B **64**, 189 (1986).

[6] C. A. Regal, M. Greiner, and D. S. Jin, *Observation of Resonance Condensation of Fermionic Atom Pairs*, Phys. Rev. Lett. **92**, 040403 (2004) [arXiv:cond-mat/0401554].

[7] M. W. Zwierlein, C. A. Stan, C. H. Schunck, S. M. F. Raupach, A. J. Kerman, and W. Ketterle, *Condensation of Pairs of Fermionic Atoms near a Feshbach Resonance*, Phys. Rev. Lett. **92**, 120403 (2004) [arXiv:cond-mat/0403049].

[8] D. Bailin and A. Love, *Superfluidity And Superconductivity In Relativistic Fermion Systems*, Phys. Rep. **107**, 325 (1984).

[9] D. J. Dean and M. H.-Jensen, *Pairing in nuclear systems: from neutron stars to finite nuclei*, Rev. Mod. Phys. **75**, 607 (2003) [arXiv:nucl-th/0210033].

[10] K. Rajagopal and F. Wilczek, *The condensed matter physics of QCD*, in *At the frontier of particle physics: Handbook of QCD*, edited by B. I. Festschrift and M. Shifman (World Scientific, Singapore, 2001) [arXiv:hep-ph/0011333].

[11] M. G. Alford, *Color superconducting quark matter*, Ann. Rev. Nucl. Part. Sci. **51**, 131 (2001) [arXiv:hep-ph/0102047].

[12] J. I. Kapusta, *Neutrino Superfluidity*, Phys. Rev. Lett. **93**, 251801 (2004) [arXiv:hep-th/0407164].

[13] W. C. Stwalley, *Stability of Spin-Aligned Hydrogen at Low Temperatures and High Magnetic Fields: New Field-Dependent Scattering Resonances and Predissociations*, Phys. Rev. Lett. **37**, 1628 (1976).

[14] E. Tiesinga, B. J. Verhaar, and H. T. C. Stoof, *Threshold and resonance phenomena in ultracold ground-state collisions*, Phys. Rev. A **47**, 4114 (1993).

[15] K. M. O'Hara, S. L. Hemmer, S. R. Granade, M. E. Gehm, J. E. Thomas, V. Venturi, E. Tiesinga, and C. J. Williams, *Measurement of the zero crossing in a Feshbach resonance of fermionic ^{6}Li*, Phys. Rev. A **66**, 041401 (2002) [arXiv:cond-mat/0207717].

[16] C. A. Regal and D. S. Jin, *Measurement of Positive and Negative Scattering Lengths in a Fermi Gas of Atoms*, Phys. Rev. Lett. **90**, 230404 (2003) [arXiv:cond-mat/0302246].

[17] D. M. Eagles, *Possible pairing without superconductivity at low carrier concentration in bulk and thin-film superconducting semiconductors*, Phys. Rev. **186**, 456 (1969).

[18] A. J. Leggett, in *Modern Trends in the Theory of Condensed Matter* edited by A. Pekalski and R. Przystawa (Springer-Verlag, Berlin, 1980); J. Phys. (Paris), Colloq. **41**, C7-19 (1980).

[19] P. Nozières and S. Schmitt–Rink, *Bose condensation in an attractive fermion gas: from weak to strong coupling superconductivity*, J. Low Temp. Phys. **59**, 195 (1985).

[20] M. Randeria, *Crossover from BCS Theory to Bose-Einstein Condensation*, in *Bose–Einstein Condensation*, edited by A. Griffin *et al.* (Cambridge University Press, New York, 1995).

[21] See, e.g., A. L. Fetter and J. D. Walecka, *Quantum Theory of Many-Particle Systems* (McGraw Hill, New York, 1971);

A. A. Abrikosov, L. P. Gorkov, and I. E. Dzialoshinskii, *Methods of Quantum Field Theory in Statistical Physics* (Dover, New York, 1975).

[22] K. M. O'Hara, S. L. Hemmer, M. E. Gehm, S. R. Granade, and J. E. Thomas, *Observation of a Strongly Interacting Degenerate Fermi Gas of Atoms*, Science **298**, 2179 (2002) [arXiv:cond-mat/0212463].

[23] K. Dieckmann, C. A. Stan, S. Gupta, Z. Hadzibabic, C. H. Schunck, and W. Ketterle, *Decay of an Ultracold Fermionic Lithium Gas near a Feshbach Resonance*, Phys. Rev. Lett. **89**, 203201 (2002) [arXiv:cond-mat/0207046].

[24] T. Bourdel, J. Cubizolles, L. Khaykovich, K. M. F. Magalhães, S. J. J. M. F. Kokkelmans, G. V. Shlyapnikov, and C. Salomon, *Measurement of the Interaction Energy near a Feshbach Resonance in a ^{6}Li Fermi Gas*, Phys. Rev. Lett. **91**, 020402 (2003) [arXiv:cond-mat/0303079].

[25] C. A. Regal, C. Ticknor, J. L. Bohn, and D. S. Jin, *Creation of ultracold molecules from a Fermi gas of atoms*, Nature **424**, 47 (2003) [arXiv:cond-mat/0305028].

[26] K. E. Strecker, G. B. Partridge, and R. G. Hulet, *Conversion of an Atomic Fermi Gas to a Long-Lived Molecular Bose Gas*, Phys. Rev. Lett. **91**, 080406 (2003) [arXiv:cond-mat/0308318].

[27] J. Cubizolles, T. Bourdel, S. J. J. M. F. Kokkelmans, G. V. Shlyapnikov, and C. Salomon, *Production of Long-Lived Ultracold Li_2 Molecules from a Fermi Gas*, Phys. Rev. Lett. **91**, 240401 (2003) [arXiv:cond-mat/0308018].

[28] S. Jochim, M. Bartenstein, A. Altmeyer, G. Hendl, C. Chin, J. Hecker Denschlag, and R. Grimm, *Pure Gas of Optically Trapped Molecules Created from Fermionic Atoms*, Phys. Rev. Lett. **91**, 240402 (2003) [arXiv:cond-mat/0308095].

[29] M. Greiner, C. A. Regal, and D. S. Jin, *Emergence of a molecular Bose–Einstein condensate from a Fermi gas*, Nature **426**, 537 (2003) [arXiv:cond-mat/0311172].

[30] M. W. Zwierlein, C. A. Stan, C. H. Schunck, S. M. F. Raupach, S. Gupta, Z. Hadzibabic, and W. Ketterle *Observation of Bose–Einstein Condensation of Molecules*, Phys. Rev. Lett. **91**, 250401 (2003) [arXiv:cond-mat/0311617].

[31] S. Jochim, M. Bartenstein, A. Altmeyer, G. Hendl, S. Riedl, C. Chin, J. Hecker Denschlag, and R. Grimm, *Bose–Einstein Condensation of Molecules*, Science **302**, 2101 (2003).

[32] C. A. Regal, M. Greiner, and D. S. Jin, *Lifetime of Molecule-Atom Mixtures near a Feshbach Resonance in ^{40}K*, Phys. Rev. Lett. **92**, 083201 (2004) [arXiv:cond-mat/0308606].

[33] M. Bartenstein, A. Almeyer, S. Riedl, S. Jochim, C. Chin, J. Hecker Denschlag, and R. Grimm, *Crossover from a Molecular Bose-Einstein Condensate to a Degenerate Fermi Gas*, Phys. Rev. Lett. **92**, 120401 (2004) [arXiv:cond-mat/0401109].

[34] J. Kinast, S. L. Hemmer, M. E. Gehm, A. Turlapov, and J. E. Thomas, *Evidence for Superfluidity in a Resonantly Interacting Fermi Gas*, Phys. Rev. Lett. **92**, 150402 (2004) [arXiv:cond-mat/0403540].

[35] M. Bartenstein, A. Altmeyer, S. Riedl, S. Jochim, C. Chin, J. Hecker Denschlag, and R. Grimm, *Collective Excitations of a Degenerate Gas at the BEC-BCS Crossover*, Phys. Rev. Lett. **92**, 203201 (2004) [arXiv:cond-mat/0403716].

[36] T. Bourdel, L. Khayakovich, J. Cubizolles, J. Zhang, F. Chevy, M. Teichmann, L. Tarruell, S. J. J. M. F. Kokkelmans, and C. Salomon, *Experimental Study of the BEC-BCS Crossover Region in Lithium 6*, Phys. Rev. Lett. **93**, 050401 (2004) [arXiv:cond-mat/0403091].

[37] C. Chin, M. Bartenstein, A. Altmeyer, S. Riedl, S. Jochim, J. Hecker Denschlag, and R. Grimm, *Observation of the Pairing Gap in a Strongly Interacting Fermi Gas*, Science **305**, 1128 (2004) [arXiv:cond-mat/0405632].

[38] J. Kinast, A. Turlapov, and J. E. Thomas, *Breakdown of hydrodynamics in the radial breathing mode of a strongly interacting Fermi gas*, Phys. Rev. A **70**, 051401(R) (2004) [arXiv:cond-mat/0408634].

[39] J. Kinast, A. Turlapov, J. E. Thomas, Q. Chen, J. Stajic, and K. Levin, *Heat Capacity of a Strongly Interacting Fermi Gas*, Science **307**, 1296 (2005) [arXiv:cond-mat/0502087].

[40] G. B. Partridge, K. E. Strecker, R. I. Kamar, M. W. Jack, and R. G. Hulet, *Molecular probe of pairing in the BEC-BCS crossover*, Phys. Rev. Lett. **95**, 020404 (2005) [arXiv:cond-mat/0505353].

[41] M. W. Zwierlein, J. R. Abo-Shaeer, A. Schirotzek, C. H. Schunck and W. Ketterle, *Vortices and superfluidity in a strongly interacting Fermi gas*, Nature **435**, 1047 (2005) [arXiv:cond-mat/0505635].

[42] M. W. Zwierlein, A. Schirotzek, C. H. Schunck, and W. Ketterle, *Fermionic Superfluidity with Imbalanced Spin Populations*, Science **311**, 492 (2006) [arXiv:cond-mat/0511197].

[43] G. B. Partridge, W. Li, R. I. Kamar, Y. Liao, and R. G. Hulet, *Pairing and Phase Separation in a Polarized Fermi Gas*, Science **311**, 503 (2006) [arXiv:cond-mat/0511752].

[44] M. W. Zwierlein, C. H. Schunck, A. Schirotzek, and W. Ketterle, *Direct Observation of the Superfluid Phase Transition in Ultracold Fermi Gases*, Nature **442**, 54 (2006) [arXiv:cond-mat/0605258].

[45] Y. Shin, M. W. Zwierlein, C. H. Schunck, A. Schirotzek, and W. Ketterle, *Observation of Phase Separation in a Strongly-Interacting Imbalanced Fermi Gas*, Phys. Rev. Lett. **97**, 030401 (2006) [arXiv:cond-mat/0606432].

[46] G. B. Partridge, W. Li, Y. A. Liao, and R. G. Hulet M. Haque, and H. T. C. Stoof, *Deformation of a Trapped Fermi Gas with Unequal Spin Populations*, Phys. Rev. Lett. **97**, 190407 (2006) [arXiv:cond-mat/0608455].

[47] G. Bertsch, *Many-Body X Challenge*, in: Proc. X Conference on Recent Progress in Many-Body Theories, eds. R. F. Bishop *et al.* (World Scientific, Singapore, 2000).

[48] A. Gardestig and D. R. Phillips, *Using chiral perturbation theory to extract the neutron-neutron scattering length from* $\pi^- d \to nn\gamma$, Phys. Rev. C **73**, 014002 (2006) [arXiv:nucl-th/0501049].

[49] See, e.g., Q. Chen, J. Stajic, S. Tan, and K. Levin, *BCS-BEC Crossover: From High Temperature Superconductors to Ultracold Superfluids*, Phys. Rep. **412**, 1 (2005) [arXiv:cond-mat/0404274], and references therein.

[50] W. D. Phillips, *Laser cooling and trapping of neutral atoms*, Rev. Mod. Phys. **70**, 721 (1998).

[51] B. DeMarco and D. S. Jin, *Onset of Fermi degeneracy in a trapped atomic gas*, Science **285**, 1703 (1999).

[52] I. Arsene *et al.* [BRAHMS Collaboration], *Quark gluon plasma and color glass condensate at RHIC? The perspective from the BRAHMS experiment*, Nucl. Phys. **A757**, 1 (2005) [arXiv:nucl-ex/0410020].

[53] B. B. Back *et al.* [PHOBOS Collaboration], *The PHOBOS perspective on discoveries at RHIC*, Nucl. Phys. **A757**, 28 (2005) [arXiv:nucl-ex/0410022].

[54] J. Adams *et al.* [STAR Collaboration], *Experimental and theoretical challenges in the search for the quark gluon plasma: The STAR collaboration's critical assessment of the evidence from RHIC collisions*, Nucl. Phys. **A757**, 102 (2005) [arXiv:nucl-ex/0501009].

[55] K. Adcox *et al.* [PHENIX Collaboration], *Formation of dense partonic matter in relativistic nucleus nucleus collisions at RHIC: Experimental evaluation by the PHENIX collaboration*, Nucl. Phys. **A757**, 184 (2005) [arXiv:nucl-ex/0410003].

[56] Brookhaven National Laboratory, *RHIC Scientists Serve Up "Perfect" Liquid*, in Laboratory News (April 2005).
`http://www.bnl.gov/bnlweb/pubaf/pr/PR_display.asp?prID=05-38`

[57] See, e.g., K. Yagi, T. Hatsuda, and Y. Miake, *Quark-Gluon Plasma* (Cambridge University Press, Cambridge, 2005).

[58] M. H. Anderson, J. R. Ensher, M. R. Matthews, C. E. Wieman, and E. A. Cornell, *Observation of Bose–Einstein condensation in a dilute atomic vapor*, Science **269**, 198 (1995).

[59] K. B. Davis, M.–O. Mewes, M. R. Andrews, N. J. van Druten, D. S. Durfee, D. M. Kurn, and W. Ketterle, *Bose–Einstein condensation in a gas of sodium atoms*, Phys. Rev. Lett. **75**, 3969 (1995).

[60] C. A. Stan, M. W. Zwierlein, C. H. Schunck, S. M. F. Raupach, and W. Ketterle, *Observation of Feshbach Resonances between Two Different Atomic Species*, Phys. Rev. Lett. **93**, 143001 (2004) [arXiv:cond-mat/0406129].

[61] S. Inouye, J. Goldwin, M. L. Olsen, C. Ticknor, J. L. Bohn, and D. S. Jin, *Observation of Heteronuclear Feshbach Resonances in a Mixture of Bosons and Fermions*, Phys. Rev. Lett. **93**, 183201 (2004) [arXiv:cond-mat/0406208].

[62] M. G. Alford, J. Berges, and K. Rajagopal, *Gapless color superconductivity*, Phys. Rev. Lett. **84**, 598 (2000) [arXiv:hep-ph/9908235].

[63] I. Shovkovy and M. Huang, *Gapless two-flavor color superconductor*, Phys. Lett. B **564**, 205 (2003) [arXiv:hep-ph/0302142].

[64] M. Huang and I. Shovkovy, *Gapless color superconductivity at zero and at finite temperature*, Nucl. Phys. **A729**, 835 (2003) [arXiv:hep-ph/0307273].

[65] E. Gubankova, W. V. Liu, and F. Wilczek, *Breached pairing superfluidity: Possible realization in QCD*, Phys. Rev. Lett. **91**, 032001 (2003) [arXiv:hep-ph/0304016].

[66] M. Alford, C. Kouvaris, and K. Rajagopal, *Gapless color-flavor-locked quark matter*, Phys. Rev. Lett. **92**, 222001 (2004) [arXiv:hep-ph/0311286].

[67] C. A. R. Sá de Melo, M. Randeria, and J. R. Engelbrecht, *Crossover from BCS to Bose Superconductivity: Transition Temperature and Time-Dependent Ginzburg-Landau Theory*, Phys. Rev. Lett. **71**, 3202 (1993).

[68] J. R. Engelbrecht, M. Randeria and C. A. R. Sá de Melo, *BCS to Bose crossover: Broken-symmetry state*, Phys. Rev. B **55**, 15153 (1997).

[69] R. Haussmann, *Crossover from BCS superconductivity to Bose–Einstein condensation: A self-consistent theory*, Z. Phys. B **91**, 291 (1993); *Properties of a Fermi liquid at the superfluid transition in the crossover region between BCS superconductivity and Bose–Einstein condensation*, Phys. Rev. B **49**, 12975 (1994).

[70] M. Holland, S. J. J. M. F. Kokkelmans, M. L. Chiofalo, and R. Walser, *Resonance Superfluidity in a Quantum Degenerate Fermi Gas*, Phys. Rev. Lett. **87**, 120406 (2001) [arXiv:cond-mat/0103479].

[71] E. Timmermans, K. Furuyab, P. W. Milonnia, and A. K. Kermanc, *Prospect of creating a composite Fermi–Bose superfluid*, Phys. Lett. A **285**, 228 (2001) [arXiv:cond-mat/0103327].

[72] Y. Ohashi and A. Griffin, *BCS-BEC Crossover in a Gas of Fermi Atoms with a Feshbach Resonance*, Phys. Rev. Lett. **89**, 130402 (2002) [arXiv:cond-mat/0201262]; *Superfluid transition temperature in a trapped gas of Fermi atoms with a Feshbach resonance*, Phys. Rev. A **67**, 033603 (2003) [arXiv:cond-mat/0210185].

[73] J. N. Milstein, S. J. J. M. F. Kokkelmans, and M. J. Holland, *Resonance theory of the crossover from Bardeen-Cooper-Schrieffer superfluidity to Bose–Einstein condensation in a dilute Fermi gas*, Phys. Rev. A **66**, 043604 (2002) [arXiv:cond-mat/0204334].

[74] A. Perali, P. Pieri, L. Pisani, and G. C. Strinati, *BCS-BEC Crossover at Finite Temperature for Superfluid Trapped Fermi Atoms*, Phys. Rev. Lett. **92**, 220404 (2004) [arXiv:cond-mat/0311309].

[75] X.-J. Liu and H. Hu, *Self-consistent theory of atomic Fermi gases with a Feshbach resonance at the superfluid transition*, Phys. Rev. A **72**, 063613 (2005) [arXiv:cond-mat/0505572].

[76] Y. Nishida and H. Abuki, *BCS-BEC crossover in a relativistic superfluid and its significance to quark matter*, Phys. Rev. D **72**, 096004 (2005) [arXiv:hep-ph/0504083].

[77] H. Abuki, *BCS/BEC crossover in Quark Matter and Evolution of its Static and Dynamic properties*, arXiv:hep-ph/0605081.

[78] R. Haussmann, W. Rantner, S. Cerrito, and W. Zwerger, *Thermodynamics of the BCS-BEC crossover*, arXiv:cond-mat/0608282.

[79] T.-L. Ho and E. J. Mueller, *High Temperature Expansion Applied to Fermions near Feshbach Resonance*, Phys. Rev. Lett. **92**, 160404 (2004) [arXiv:cond-mat/0306187].

[80] C. J. Horowitz and A. Schwenk, *The Virial Equation of State of Low-Density Neutron Matter*, Phys. Lett. B **638**, 153 (2006) [arXiv:nucl-th/0507064].

[81] G. Rupak, *Universality in a 2-component Fermi System at Finite Temperature*, arXiv:nucl-th/0604053.

[82] J. Carlson, S.–Y. Chang, V. R. Pandharipande, and K. E. Schmidt, *Superfluid Fermi Gases with Large Scattering Length*, Phys. Rev. Lett. **91**, 050401 (2003) [arXiv:physics/0303094].

[83] S. Y. Chang, V. R. Pandharipande, J. Carlson, and K. E. Schmidt, *Quantum Monte Carlo studies of superfluid Fermi gases*, Phys. Rev. A **70**, 043602 (2004) [arXiv:physics/0404115].

[84] J. W. Chen and D. B. Kaplan, *A lattice theory for low energy fermions at finite chemical potential*, Phys. Rev. Lett. **92**, 257002 (2004) [arXiv:hep-lat/0308016].

[85] G. E. Astrakharchik, J. Boronat, J. Casulleras, and S. Giorgini, *Equation of State of a Fermi Gas in the BEC-BCS Crossover: A Quantum Monte Carlo Study*, Phys. Rev. Lett. **93**, 200404 (2004) [arXiv:cond-mat/0406113].

[86] J. Carlson and S. Reddy, *Asymmetric Two-component Fermion Systems in Strong Coupling*, Phys. Rev. Lett. **95**, 060401 (2005) [arXiv:cond-mat/0503256].

[87] D. Lee, *Ground state energy of spin-1/2 fermions in the unitary limit*, Phys. Rev. B **73**, 115112 (2006) [arXiv:cond-mat/0511332].

[88] M. Wingate, *Critical temperature for fermion pairing using lattice field theory*, arXiv:cond-mat/0502372.

[89] A. Bulgac, J. E. Drut, and P. Magierski, *Spin 1/2 Fermions in the Unitary Regime: A Superfluid of a New Type*, Phys. Rev. Lett. **96**, 090404 (2006) [arXiv:cond-mat/0505374].

[90] D. Lee and T. Schafer, *Cold dilute neutron matter on the lattice I: Lattice virial coefficients and large scattering lengths*, Phys. Rev. C **73**, 015201 (2006) [arXiv:nucl-th/0509017]; *Cold dilute neutron matter on the lattice II: Results in the unitary limit*, Phys. Rev. C **73**, 015202 (2006) [arXiv:nucl-th/0509018].

[91] E. Burovski, N. Prokofev, B. Svistunov, and M. Troyer, *Critical Temperature and Thermodynamics of Attractive Fermions at Unitarity*, Phys. Rev. Lett. **96**, 160402 (2006) [arXiv:cond-mat/0602224]; *The Fermi-Hubbard model at unitarity*, New J. Phys. **8**, 153 (2006) [arXiv:cond-mat/0605350].

[92] V. K. Akkineni, D. M. Ceperley, and N. Trivedi, *Pairing and Superfluid Properties of Dilute Fermion Gases at Unitarity*, arXiv:cond-mat/0608154.

[93] Y. Nishida and D. T. Son, *ϵ expansion for a Fermi gas at infinite scattering length*, Phys. Rev. Lett. **97**, 050403 (2006) [arXiv:cond-mat/0604500].

[94] Y. Nishida and D. T. Son, *Fermi gas near unitarity around four and two spatial dimensions*, arXiv:cond-mat/0607835.

[95] Y. Nishida, *Unitary Fermi gas at finite temperature in the ϵ expansion*, arXiv:cond-mat/0608321.

[96] Z. Nussinov and S. Nussinov, *The BCS-BEC Crossover In Arbitrary Dimensions*, arXiv:cond-mat/0410597; *Triviality of the BCS-BEC crossover in extended dimensions: Implications for the ground state energy*, Phys. Rev. A **74**, 053622 (2006).

[97] F. Sauli and P. Kopietz, *Low-density expansion for the two-dimensional electron gas*, arXiv:cond-mat/0608423.

[98] P. Nikolic and S. Sachdev, *Renormalization group fixed points, universal phase diagram, and 1/N expansion for quantum liquids with interactions near the unitarity limit*, arXiv:cond-mat/0609106.

[99] G. Rupak, *Dimer scattering in the ε expansion*, arXiv:nucl-th/0605074.

[100] K. G. Wilson and J. Kogut, *The renormalization group and the ϵ expansion*, Phys. Rep. **12**, 75 (1974).

[101] G. Rupak, T. Schaefer, and A. Kryjevski, *Polarized fermions in the unitarity limit*, arXiv:cond-mat/0607834.

[102] P. Arnold, J. E. Drut, and D. T. Son, *NNLO ϵ expansion for a Fermi gas at infinite scattering length*, arXiv:cond-mat/0608477.

[103] J. W. Chen and E. Nakano, *BEC-BCS Crossover in the ϵ Expansion*, arXiv:cond-mat/0610011.

[104] M. Y. Veillette, D. E. Sheehy, and L. Radzihovsky, *Large-N expansion for unitary superfluid Fermi gases*, arXiv:cond-mat/0610798.

[105] Y. Nishida and D. T. Son, *Phase structure of unitary Fermi gas with unequal densities and masses*, in preparation.

[106] M. Randeria, J.–M. Duan, and L.–Y. Shieh, *Bound states, Cooper pairing, and Bose condensation in two dimensions*, Phys. Rev. Lett. **62**, 981 (1989); *Superconductivity in a two-dimensional Fermi gas: Evolution from Cooper pairing to Bose condensation*, Phys. Rev. B **41**, 327 (1990).

[107] R. L. Stratonovich, *On a method of calculating quantum distribution functions*, Dokl. Akad. Nauk SSSR **115**, 1097 (1957); [Soviet Phys. Doklady **2**, 416 (1958)].

[108] J. Hubbard, *Calculation of Partition Functions*, Phys. Rev. Lett. **3**, 77 (1959).

[109] L. P. Gorkov, *On the energy spectrum of superconductors*, Sov. Phys. JETP **7**, 505 (1958).

[110] Y. Nambu, *Quasi-Particles and Gauge Invariance in the Theory of Superconductivity*, Phys. Rev. **117**, 648 (1960).

[111] See, e.g., M. E. Peskin and D. V. Schroeder, *An Introduction to Quantum Field Theory* (Addison-Wesley, Reading MA, 1995).

[112] D. T. Son and M. A. Stephanov, *Phase Diagram of Cold Polarized Fermi Gas*, Phys. Rev. A **74**, 013614 (2006) [arXiv:cond-mat/0507586].

[113] L. Viverit, S. Giorgini, L. P. Pitaevskii, and S. Stringari, *Momentum distribution of a trapped Fermi gas with large scattering length*, Phys. Rev. A **69**, 013607 (2004) [arXiv:cond-mat/0307538].

[114] S. Tan, *Energetics of the Fermi gas which has BEC-BCS crossover*, arXiv:cond-mat/0505200; *Large momentum part of fermions with large scattering length*, arXiv:cond-mat/0508320.

[115] C. A. Regal, M. Greiner, S. Giorgini, M. Holland, and D. S. Jin, *Momentum Distribution of a Fermi Gas of Atoms in the BCS-BEC Crossover*, Phys. Rev. Lett. **95**, 250404 (2005) [arXiv:cond-mat/0507316].

[116] G. E. Astrakharchik, J. Boronat, J. Casulleras, and S. Giorgini, *Momentum distribution and condensate fraction of a Fermi gas in the BCS-BEC crossover*, arXiv:cond-mat/0507483.

[117] G. Ortiz and J. Dukelsky, *BCS-to-BEC crossover from the exact BCS solution*, Phys. Rev. A **72**, 043611 (2005) [arXiv:cond-mat/0503664].

[118] L. Salasnich and N. Manini, *Condensate fraction of a Fermi gas in the BCS-BEC crossover*, Phys. Rev. A **72**, 023621 (2005) [arXiv:cond-mat/0506074].

[119] C. N. Yang, *Concept of Off-Diagonal Long-Range Order and the Quantum Phases of Liquid He and of Superconductors*, Rev. Mod. Phys. **34**, 694 (1962).

[120] J. M. Luttinger and J. C. Ward, *Ground-State Energy of a Many-Fermion System. II*, Phys. Rev. **118**, 1417 (1960).

[121] C. De Dominicis and P. C. Martin, *Stationary Entropy Principle and Renormalization in Normal and Superfluid Systems. I. Algebraic Formulation*, J. Math. Phys. **5**, 14 (1964); *Stationary Entropy Principle and Renormalization in Normal and Superfluid Systems. II. Diagrammatic Formulation*, J. Math. Phys. **5**, 31 (1964).

[122] G. Baym and L. P. Kadanoff, *Conservation Laws and Correlation Functions*, Phys. Rev. **124**, 287 (1961).

[123] G. Baym, *Self-Consistent Approximations in Many-Body Systems*, Phys. Rev. **127**, 1391 (1962).

[124] P. Fulde and R. A. Ferrell, *Superconductivity in a Strong Spin-Exchange Field*, Phys. Rev. **135**, A550 (1964).

[125] A. I. Larkin and Y. N. Ovchinnikov, *Superconductivity in a Strong Spin-Exchange Field*, Zh. Eksp. Teor. Fiz. **47**, 1136 (1964) [Sov. Phys. JETP **20**, 762 (1965)].

[126] M. Iskin and C. A. R. Sà de Melo, *Two-species fermion mixtures with population imbalance*, arXiv:cond-mat/0604184; *Asymmetric two-component Fermi gas with unequal masses*, arXiv:cond-mat/0606624.

[127] S.–T. Wu, C.–H. Pao, and S.–K. Yip, *Resonant pairing between Fermions with unequal masses*, arXiv:cond-mat/0604572.

[128] G.–D. Lin, W. Yi, and L.–M. Duan, *Superfluid shells for trapped fermions with mass and population imbalance*, Phys. Rev. A **74**, 031604(R) (2006) [arXiv:cond-mat/0607664].

[129] M. M. Parish, F. M. Marchetti, A. Lamacraft, and B. D. Simons, *Polarized Fermi condensates with unequal masses: Tuning the tricritical point*, arXiv:cond-mat/0608651.

[130] L. P. Gor'kov and T. K. Melik–Barkhudarov, *Contribution to the Theory of Superfluidity in an Imperfect Fermi Gas*, Sov. Phys. JETP **13**, 1018 (1961).

[131] H. Heiselberg, C. J. Pethick, H. Smith, and L. Viverit, *Influence of Induced Interactions on the Superfluid Transition in Dilute Fermi Gases*, Phys. Rev. Lett. **85**, 2418 (2000) [arXiv:cond-mat/0004360].

[132] J. M. Luttinger, *Fermi Surface and Some Simple Equilibrium Properties of a System of Interacting Fermions*, Phys. Rev. **119**, 1153 (1960).

[133] See, e.g., J. Z.–Justin, *Quantum Field Theory and Critical Phenomena* (Clarendon Press, Oxford, 2002).

[134] V. Efimov, *Energy levels arising from resonant two-body forces in a three-body system*, Phys. Lett. B **33**, 563 (1970); *Weakly-bound states of three resonantly-interacting particles*, Sov. J. Nucl. Phys. **12**, 589 (1971); *Energy levels of three resonantly interacting particles*, Nucl. Phys. **A210**, 157 (1973).

[135] E. Braaten and H.–W. Hammer, *Universality in few-body systems with large scattering length*, Phys. Rep. **428**, 259 (2006) [arXiv:cond-mat/0410417].

[136] E. Nielsen, D. V. Fedorov, A. S. Jensen, and E. Garrido, *The three-body problem with short-range interactions*, Phys. Rep. **347**, 373 (2001).

[137] D. J. Gross and A. Neveu, *Dynamical symmetry breaking in asymptotically free field theories*, Phys. Rev. D **10**, 3235 (1974).

[138] B. Lautrup, *On high order estimates in QED*, Phys. Lett. B **69**, 109 (1977).

[139] G. 't Hooft, in *The Whys of subnuclear physics*, Proc. Int. School, Erice, Italy, 1977, edited by A. Zichichi (Plenum, New York, 1978).